Nonlinear Optics in Planar Silica-on-Silicon Disk Resonators

Thesis by

Jiang Li

In Partial Fulfillment of the Requirements

for the Degree of

Doctor of Philosophy

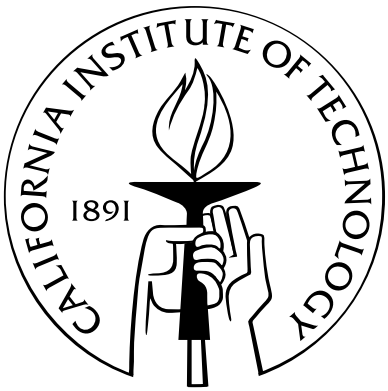

California Institute of Technology

Pasadena, California

2013

(Defended May 20, 2013)

To my parents

Acknowledgments

I would like to thank my advisor, Prof. Kerry Vahala. It has been a great honor and pleasure to work with Kerry for the past five years, and I appreciate his guidance and support very much. His passion and brilliance in fundamental science and applied technologies always inspire me. His vision and deep insight in science also help me to widen my horizons. I also enjoyed the research freedom he created and is grateful for his trust and help with carrying on and managing research projects. I also like his personal charm as a calm, gracious and warm person.

I also want to thank Dr. Scott Diddams, for his support and encouragement. I enjoyed the days when we worked side by side in the lab during his visit at Caltech and benefited a lot from our discussions. I am grateful to learn experimental skills from a laser guru like Dr. Diddams. I also enjoyed the visits to his lab at NIST and am always amazed by his creative and deep thinking in laser sciences, frequency combs and precision measurements.

Special thanks to Hansuek Lee. It has been a nice and long-term collaboration with Hansuek during my PHD study at Caltech. Thank Hansuek for the work in developing and fabricating the amazing and beautiful devices. I always enjoyed our stimulating discussions.

Thanks to Scott Papp, Pascal Del'Haye, Qiang Lin and Ivan Grudinin for so many fruitful and inspiring discussions. Thank the junior members of the Vahala group, Kiyoul Yang, Myoung-Gyun Suh, Xu Yi and Dongyoon Oh, for making such a dynamic and vibrant group. Also I have enjoyed the interactions and discussions with fellow graduate students and post-docs in the applied physics and physics department, Amir Safavi-Naeini, Jeff Hill, Simon Groeblacher, Alex Krause and Tim Blasius in Prof. Oskar Painter's group, Ari Weinstein and Chan U Lei in Prof. Keith Schwab's group, Hao Chu in Prof. David Hsieh's group, Haixing Miao in Prof. Yanbei Chen's group, Naresh Satyan in Prof. Amonn Yariv's group, Daniel Alton in Prof. Jeff Kimble's group, Liang Feng in Prof. Axel Sherer's group, Juhwan Yoo and Meisam Nazari in Prof. Azita Emami-Neyestanak's group.

Also thanks to Dr. Reginald Lee. I enjoyed every discussion with you and the visit to your laser company located close to Caltech campus. Your enthusiasm for low-noise lasers and entrepreneurship in photonic technologies inspired me. I also liked the coffee times we spent together at the red door cafe.

I would also like to thank my other friends in and outside Caltech. David Bo Chen and Brooks Zhongzheng Fu, Maolin Ci, Minghong Lin, Yingrui Chang, Daiqi Linghu, Sinan Zhao, Liling Gu, and Suyao Ji, thank you for the good times we spent together. To my friends who I have not mentioned by name, thank you for the companionship and the laughter you brought to my life.

Last but not least, I would like to thank my parents, and my sister. You are always there to support, encourage and listen to me. Thank you for all the love and support. My thesis is dedicated to you.

Abstract

Optical frequency combs (OFCs) provide direct phase-coherent link between optical and RF frequencies, and enable precision measurement of optical frequencies. In recent years, a new class of frequency combs (microcombs) have emerged based on parametric frequency conversions in dielectric microresonators. Micocombs have large line spacing from 10's to 100's GHz, allowing easy access to individual comb lines for arbitrary waveform synthesis. They also provide broadband parametric gain bandwidth, not limited by specific atomic or molecular transitions in conventional OFCs. The emerging applications of microcombs include low noise microwave generation, astronomical spectrograph calibration, direct comb spectroscopy, and high capacity telecommunications.

In this thesis, research is presented starting with the introduction of a new type of chemically etched, planar silica-on-silicon disk resonator. A record Q factor of 875 million is achieved for on-chip devices. A simple and accurate approach to characterize the FSR and dispersion of microcavities is demonstrated. Microresonator-based frequency combs (microcombs) are demonstrated with microwave repetition rate less than 80 GHz on a chip for the first time. Overall low threshold power (as low as 1 mW) of microcombs across a wide range of resonator FSRs from 2.6 to 220 GHz in surface-loss-limited disk resonators is demonstrated. The rich and complex dynamics of microcomb RF noise are studied. High-coherence, RF phase-locking of microcombs is demonstrated where injection locking of the subcomb offset frequencies are observed by pump-detuning-alignment. Moreover, temporal mode locking, featuring subpicosecond pulses from a parametric 22 GHz microcomb, is observed. We further demonstrated a shot-noise-limited white phase noise of microcomb for the first time. Finally, stabilization of the microcomb repetition rate is realized by phase lock loop control.

For another major nonlinear optical application of disk resonators, highly coherent, simulated Brillouin lasers (SBL) on silicon are also demonstrated, with record low Schawlow-Townes noise less than 0.1 Hz^2/Hz for any chip-based lasers and low technical noise comparable to commercial narrow-linewidth fiber lasers. The SBL devices are efficient, featuring more than 90 % quantum efficiency and threshold as low as 60 μW. Moreover, novel properties of the SBL are studied, including cascaded operation, threshold tuning, and mode-pulling phenomena. Furthermore, high performance microwave generation using on-chip cascaded Brillouin oscillation is demonstrated. It is also robust enough to enable incorporation as the optical voltage-controlled-oscillator in the first demonstration

of a photonic-based, microwave frequency synthesizer. Finally, applications of microresonators as frequency reference cavities and low-phase-noise optomechanical oscillators are presented.

Contents

List of Figures

List of Tables

Chapter 1

Ultrahigh-Q Planar Disk Resonators on a Silicon Chip

1.1 Introduction

Optical microcavities confine light to small mode volume due to resonant recirculation [1]. In whispering-gallery-mode (WGM) optical microcavities, light circulates around the boundary of a dielectric microcavity due to total internal reflection, in analogy to acoustic waves circulating around a round enclosure (e.g., the St Paul's Cathedral in London and the Echo Wall of Temple of Heaven in Beijing). Maintaining a large photon storage time, or equivalently high Q factors in optical cavities, are critical in many scientific and technological applications of microcavities, including cavity QED [2], cavity optomechanics [3], biosensing [4, 5], microresonator-based frequency combs [6], and narrow-linewidth laser sources [7, 8]. To achieve high Q factor in WGM cavities, it relies on the use of low-absorption dielectrics (to reduce material absorption loss) and the creation of very smooth dielectric surfaces (to reduce surface scattering loss). Although crystalline resonators currently have the highest Q factors on the order of 10^{10} and 10^{11} [9–11], for silicon-chip-based devices, microtoroid silica cavities provide the highest Q factors on the order of several hundred million [12]. Microtoroid resonators combine low material loss of silica with a reflow technique in which surface tension is used to smooth lithographic and etch-related blemishes. However, reflow smoothing makes it very challenging to fabricate larger-diameter ultrahigh-Q (UHQ) resonators or to leverage the full range of integration tools and devices available on silicon.

In this chapter, we report on a new silica-on-silicon planar disk resonator [7], using only conventional semiconductor processing methods on a silicon wafer, avoiding the reflow process necessary for microtoroid fabrication. A record Q factor of 875 million is achieved for on-chip devices. By eliminating the reflow process, ultrahigh-Q (UHQ) resonators with millimeter to centimeter dimensions are demonstrated on silicon, with important applications on microcombs, stimulated Brillouin lasers, and rotation sensing. Accurate resonator size control enables precise free-spectral range

(FSR) control of the device, and sub-MHz precision of resonator FSR for 10–50 GHz devices has been demonstrated.

1.2 Fabrication of Ultrahigh-Q Disk Resonators on a Chip

The procedure for fabricating the planar silica-on-silicn disk resonators is given in figure 1.1 [7]. It starts with thermal oxide growth with a thickness from 2 to 10 μm on silicon. The oxide layers were prepared using wet oxidation at first, and then a final dry oxidation step (24 hours) at 1000 °C was adapted to drive down the water content in the silica oxide. Photoresist was patterned using a GCA 6300 stepper on the silica layer. A post-exposure bake was then used to cure the surface roughness of the photoresist pattern, which acted as an etch mask during buffered hydrofluoric wet etching of silica. Careful examination of the wet etch revealed that the vertex formed by the lower oxide surface and upper surface contained an etch front distinct from that associated with the upper surface, which is called the "foot" region. This region has a roughness level that is higher than any other surface and is a significant contributor to Q degradation. By extending the etch time beyond what is necessary to reach the silicon substrate, this foot region can be eliminated. With elimination of the foot etch front, the isotropic and uniform etching characteristic of buffered hydrofluoric solution results in oxide disks and waveguides with very smooth wedge profiles, which enhance the Q factors. After a conventional cleaning process to remove photoresist and organics, silicon was isotropically etched by xenon difluoride to create an air-cladding whispering-gallery resonator. During this dry etch, the silicon undercut is set to reduce coupling of the optical mode to the silicon support pillar. This value is typically set to $\sim$ 100 mm for 1-mm-diameter structures and over 150 mm for 7.5-mm-diameter disks; however, smaller undercuts are possible while still preserving UHQ performance.

The microscopic photographs of the planar disk resonators are given in figure 1.2, with the size of 500 μm (left) and 2 mm (right). Figure 1.3 shows the scanning-electron-microscopy (SEM) images of the disk resonators. The resonator diameter in figure 1.3a is 2 mm. Figure 1.3b shows the side view of the resonator, illustrating clearly the wedge like silica resonator layer and the silicon pillar substrate. The wedge of the resonator can be varied from 12° to 27°. This can be controlled by adjustment of the photoresist adhesion to the silica during spin-coating using commercially available adhesion promoters. Figure 1.3c is an angled zoom-in view of disk resonator and the silicon pillar. Atomic-level smoothness of the silica surfaces is clearly shown. Using atomic-force-microscope, the roughness of the upper, wedge, and lower surfaces of the silica resonator is measured. The r.m.s. roughness values on 10° wedge-angle devices were 0.15 nm (upper), 0.46 nm (wedge), and 0.70 nm (lower); for the 27° wedge-angle devices these values were 0.15 nm (upper), 0.75 nm (wedge), and 0.70 nm (lower).

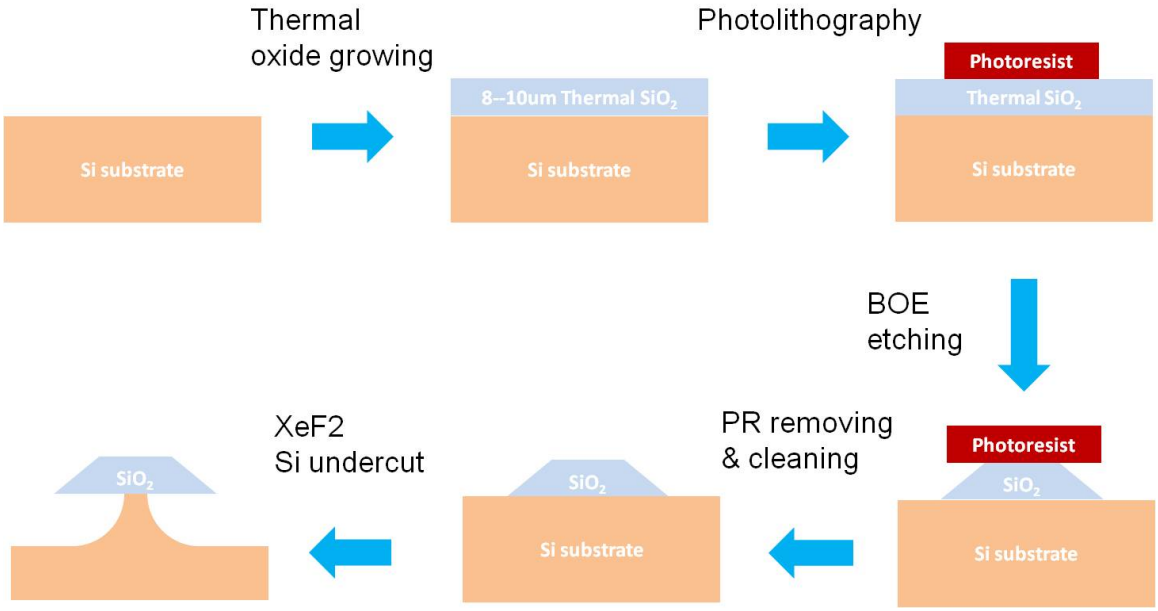

Figure 1.1: **Fabrication procedure of disk resonators.** It starts with thermal oxide growth with a thickness from 2-10 μm on silicon, followed by lithography and oxide etching with buffered hydrofluoric acid. After a conventional cleaning process to remove photoresist and organics, silicon was isotropically etched by xenon difluoride to create an air-cladding whispering-gallery silica resonator.

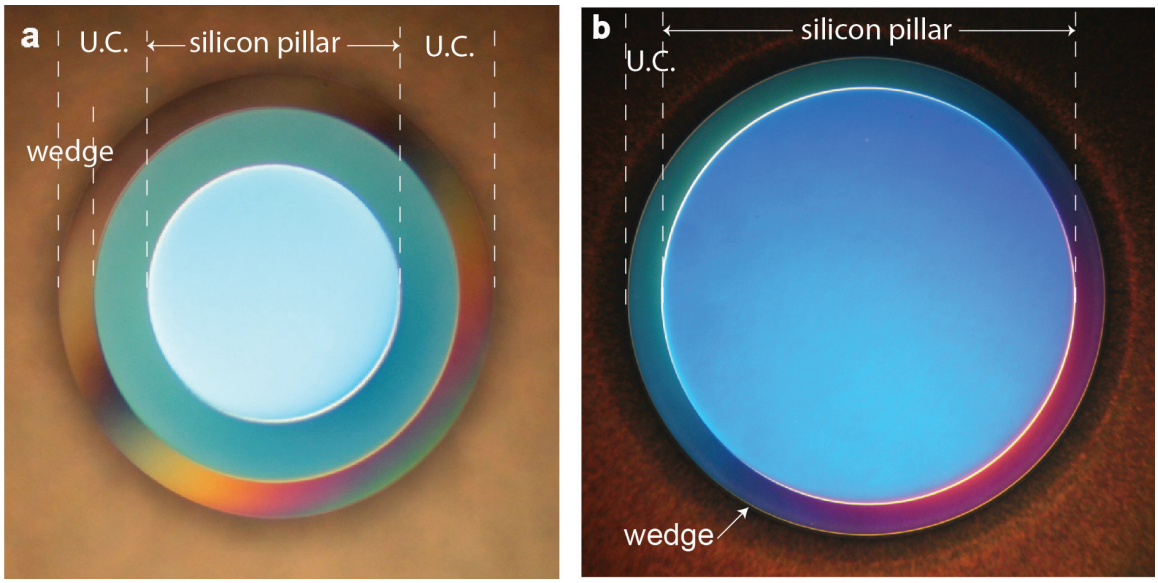

Figure 1.2: **Microscopy photograph of disk resonator.** (a) A wedge disk resonator with diameter of 500 μm. The silicon pillar substrate, the siica disk layer with air-cladding, and the wedge surface are illustrated. (b) A wedge resonator with diameter of 2 mm.

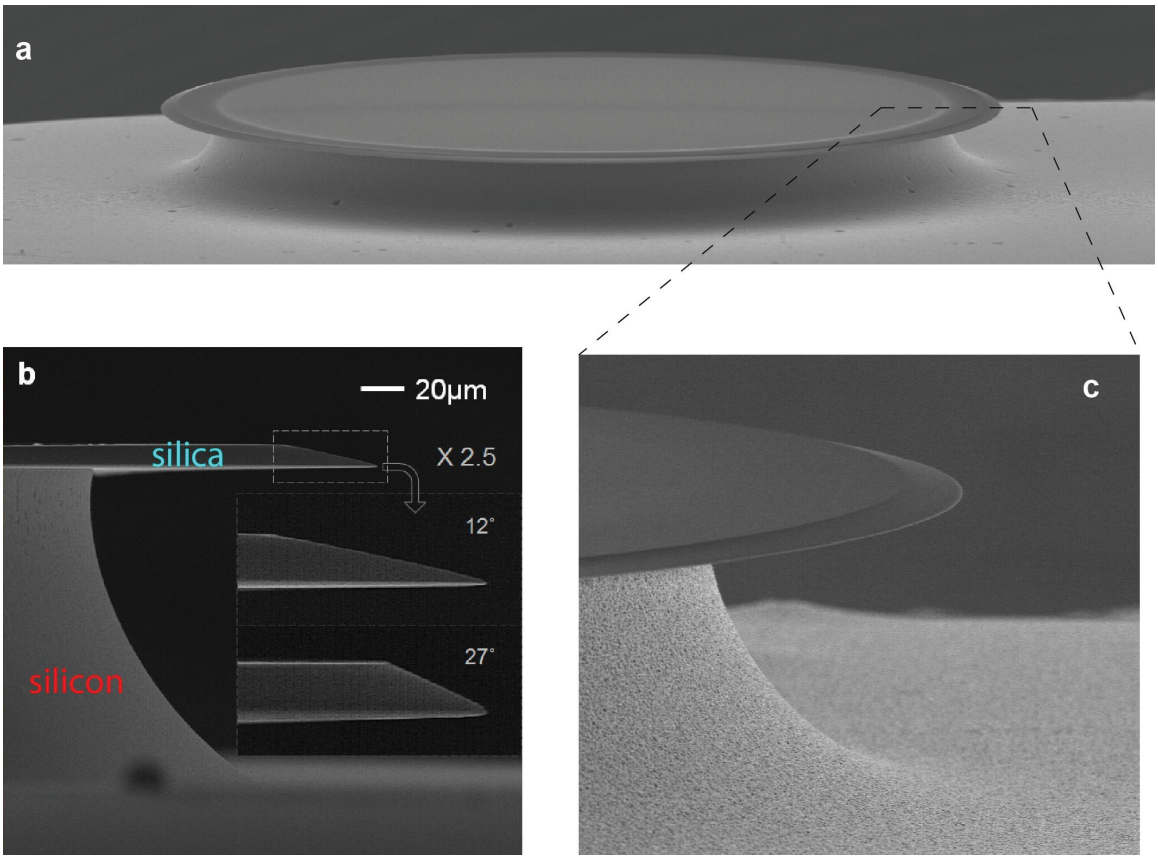

Figure 1.3: **SEM photograph of disk resonator.** (a) A scanning-electron-microscopy (SEM) image of a 2 mm disk resonator. (b) A side view of the silica-on-silicon disk resonator. Wedge angles from 12° to 27° can be controlled by adjustment of the photoresist adhesion during spin-coating. (c) A zoom-in angled view of the resonator showing atomic-level smooth surfaces.

1.3 Ultrahigh-Q Factors of the Planar Silica Disk Resonators

The Q factor of the disk resonators was measured by the resonant transmission spectrum of the cavity. An external-cavity-diode-laser (ECDL) was evanescently coupled to the resonator by a taper fiber [13, 14]. The taper fiber was placed around half of the wedge surface of the resonator, where the optical mode reside underneath the wedge surface in the silica. The output of the cavity is detected by a photodetecotor with 125 MHz bandwidth to record the tranmission spectrum of the cavity. To calibrate the scanning range of the ECDL frequency, a tap of the laser is sent to a fiber Mach-Zehnder Interferometer (MZI) with a calibrated free-spectral-range (FSR) in the range of 5–10 MHz. Thus simultaneous recording of the cavity transmission and the MZI fringe output enables accurate measurement of the cavity linewidth. To expedite the Q measurement of the device, a broad spectral scan exceeding a full cavity FSR is used to record all the resonance modes within one FSR. A fast sampling oscilloscope with sampling rate 5 Gs/s is used to capture a long sequence of time-domain cavity transmission spectrum with abundant data points to resolve the cavity lineshape. The spectrum was then analyzed using a fitting algorithm to identify and fit the resonator modes. This enables a fast acquisition of all the cavity transverse modes and identification of the mode with the highest Q factor. Moreover, the Q factor was also confirmed by independent cavity ringdown measurement.

Figure 1.4 gives the cavity transmission spectral lineshape for 7.5 mm disks with 12° wedge (a) and 27° wedge (b). The 12° device has a loaded linewidth of 0.68 MHz and an intrinsic Q factor of 405 million, while the 27° device has a loaded linewidth of 0.3 MHz and an instrinsic Q factor of 875 million, which is a record Q factor for on-chip resonators. The 27° device in general has a higher Q factor than the 12° devices at the same diameter. A more systematic and complete study on the disk Q factors is given in figure 1.5, showing the Q factors changing with the resonator diameter and also oxide thickness. The increase of the Q factor with diameter and thickness can be understood from the scattering loss induced at the dielectric-air surface. While bulk material loss is constant with diameter, both larger diameter and thicker oxide push the optical mode further away from the surface, thus causing a reduced field amplitude at the surface and subsequently lower losses by surface scattering.

1.4 Precise Size Control of the Disk Resonator

The ability to lithographically define UHQ resonators rather than rely on the reflow process enables a multi-order-of-magnitude improvement in the control of resonator diameter and FSR. This feature is especially important in microcombs and certain nonlinear sources [15, 16]. As a preliminary test of the practical limits of FSR control, two studies were conducted. In the first, a series of resonator

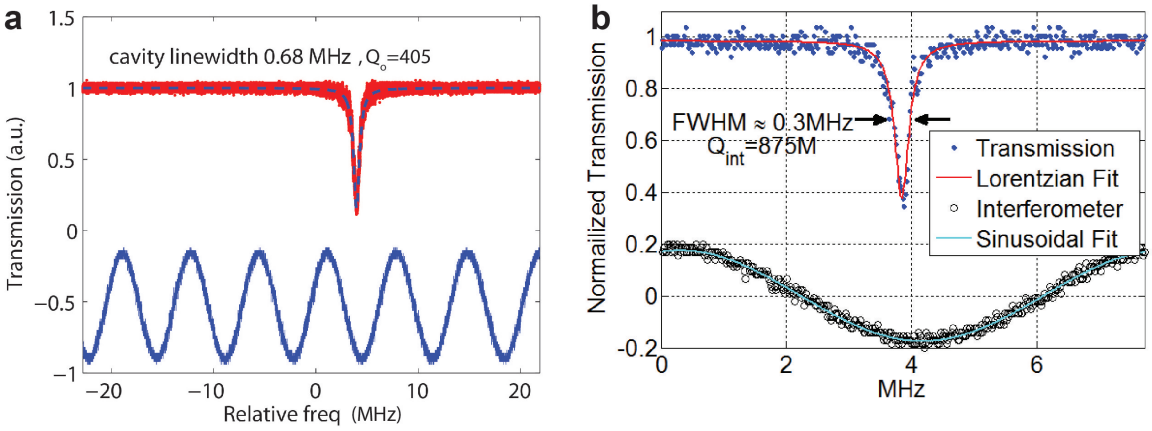

Figure 1.4: **Transmission lineshape of the UHQ resonance.** (a) A transmission lineshape of a 7.5 mm disk resonator with wedge angle of ∼12°. The loaded linewidth is 0.68 MHz, giving the intrinsic cavity Q factor of 405 million. The lower fringe is the Mach-Zehnder Interferometer (MZI) output used for calibration of the laser frequency scan. (b) A transmission lineshape of a 7.5 mm disk resonator with wedge angle 27°. The loaded linewidth is 0.3 MHz, giving the intrinsic cavity Q factor of 875 million.

diameters were set in a CAD file that was to be used to create a photomask. A plot of the measured FSR (fundamental mode) versus CAD file target diameter is provided in figure 1.6. The variance from ideal linear behavior measured on five devices from different locations on the same four-inch wafer is 2.4 MHz, giving a relative variance of better than 1:4500 (FSR ≈ 11 GHz). The inset to figure 1.6 shows that for a second set of four devices from different locations on a separate wafer, but having the same target diameter, the variance is further improved to a value of 0.45 MHz or 1:20000. More data runs will be accumulated over time to provide better statistics, but these preliminary findings are nonetheless very encouraging. There is an overall size reduction that occurs between the mask and final etch diameter of ∼10 μm (10 μm oxide). However, the above data suggest that this size reduction can be accurately calibrated.

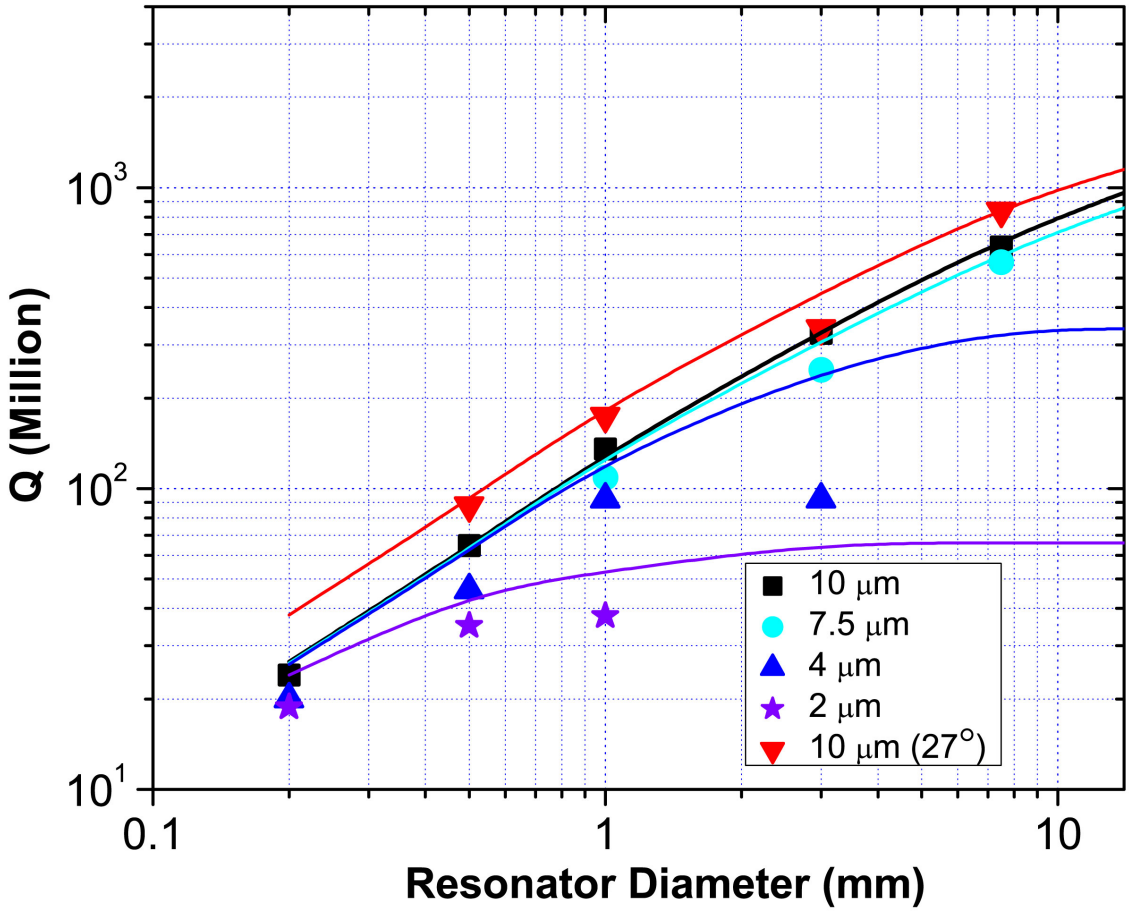

Figure 1.5: **Summary of Q factors with parameters of diameter and oxide thickness.** The markers are experimental data, and the curves are the predicated Q factors from calculation. The increase of the Q factor with diameter and thickness can be understood from the change of surface-scattering loss by these two parameters. While bulk material loss is constant with diameter, both larger diameter and thicker oxide move the optical mode further away from the surface, thus cause a reduced field amplitude at the surface and lower loss by surface-scattering.

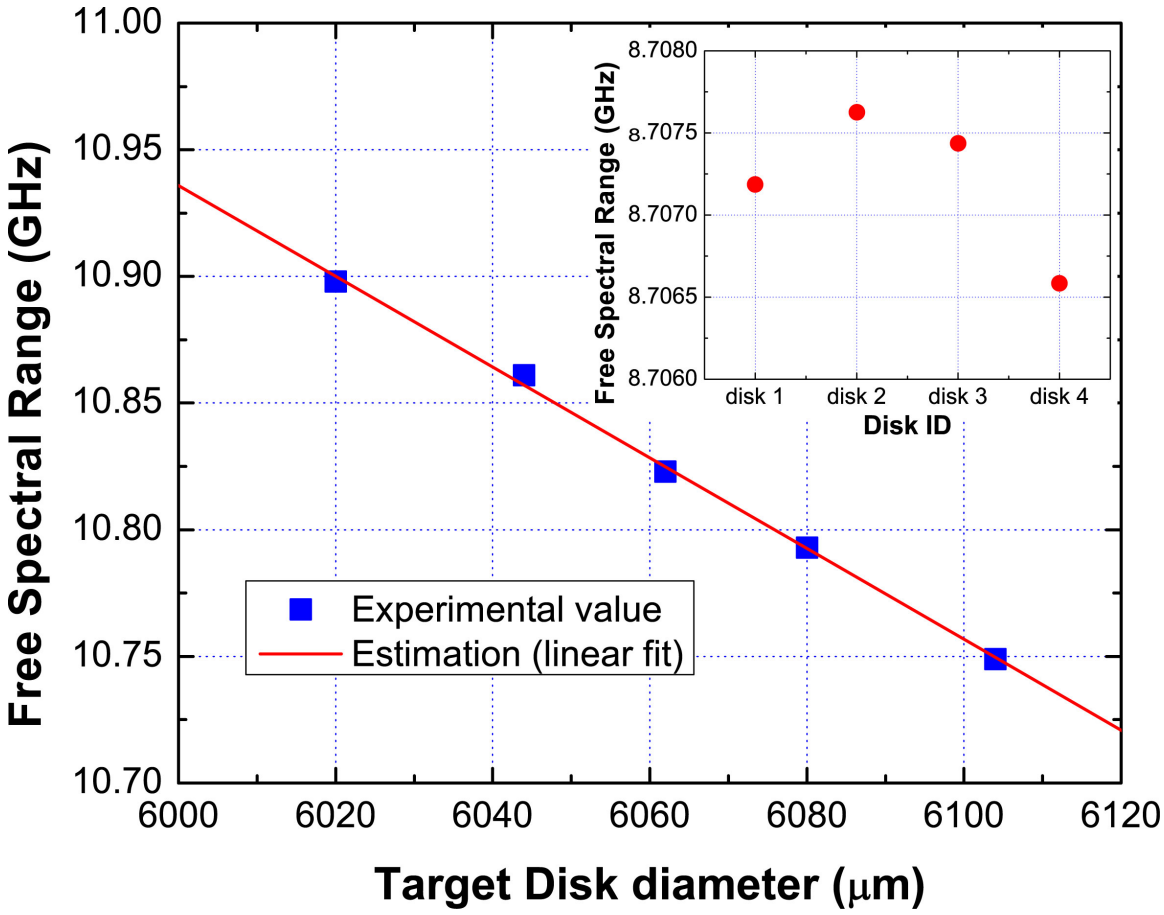

Figure 1.6: **Size control of the disk resonator.** The measured FSR of the device is plotted versus the design diameter on a lithographic mask. The plot shows one device at each size for five different sizes. The r.m.s. variance is 2.4 MHz (relative variance of less than 1:4500). Inset: FSR data measured on four devices with the same target FSR. An improved variance of 0.45 MHz is obtained (a relative variance of 1:20000).

Chapter 2

Sideband Spectroscopy and Dispersion Measurement in Microcavities

2.1 Introduction

Besides cavity Q factor, the measurement of dispersion and its control have become important considerations in nonlinear applications based on microcavities. In this chapter, we also demonstrate a sideband phase-modudlation technique to accurately measure dispersion in a microcavity resulting from both geometrical and material contributions. Moreover, by combining the method with finite element simulations, we show that mapping of spectral lines to their corresponding transverse mode families is possible. The method is applicable for high-Q microcavities having microwave rate free spectral range and has a relative precision of 5.5×10^{-6} for a 2 mm disk cavity with FSR of 32.9382 GHz and Q of 150 milllion.

In microcavities, dispersion has both geometrical (cavity shape) and material contributions, and, as a result, it depends upon the wavelength and the transverse spatial mode family. The measurement of FSR as a function of wavelength provides a convenient way to characterize cavity dispersion. Along these lines, frequency combs have provided a powerful way to measure dispersion in cavities that can be approximately matched in FSR to the comb repetition frequency [17, 18]. Also, in cases where this is not possible, a frequency-comb has been used together with a tunable-diode-laser to measure FSR and dispersion [19]. These techniques, while providing fast, accurate and wideband dispersion measurement, require access to a stabilized frequency comb. In another method, "white light," filtered to a 1 nm bandwidth, has been used for dispersion measurement in a CaF_2 whispering gallery microcavity [20]. Multiple RF beat notes are produced that contain the contribution of all the WGM modes (with different transverse order and azimuthal order) in the 1 nm bandwidth probed. This is a convenient way to measure dispersion, but the method does not

enable correspondence of the optical spectral peaks with the RF beat notes. In this letter, we modify a method that has been used to measure FSR and mirror-induced dispersion in a Fabry-Perot [21] to the case of a microresonator. In that method two FM sidebands were imposed on an optical carrier and then separately tuned so as to attain locking with two cavity modes. In the present work we use a single modulation in combination with a reference interferometer. While not attaining the same level of precision in the earlier work, the present technique does not require locking to the resonator modes and provides sufficient precision to measure both the spectral and transverse mode dependence of dispersion in a high-Q silica microresonator. The technique can be applied in resonators with FSR in the microwave rate range.

2.2 Measurement Method and Uncertainty Analysis

A lithium niobate phase modulator and a microwave source are used to generate a sinusoidally, phase modulated signal on a probe laser at a modulation rate f_m close to the FSR of the resonator such that $FSR > f_m$ (see figure 2.1a). The probe laser is an external cavity diode laser and is scanned across a cavity resonance so as to produce the oscilloscope trace of the transmitted power shown in figure 2.1b. When the phase modulation is "off," the transmission spectrum of the cavity has the single Lorentzian line shape as shown in figure 2.1b (red curve). However, when the phase modulation is "on," the transmission spectrum will show three spectral peaks as the two side peaks come from the phase modulation sidebands that are coupled to the cavity through the neighboring resonances of the initial cavity resonance. The offset frequency ($\Delta f = FSR - f_m$) is then measured by using a Mach-Zehnder interferometer (MZI) to create a fringe-like reference spectrum. If T_d and T_m are corresponding oscilloscope time intervals for the offset frequency and neighboring MZI fringe maxima, then the offset frequency is given by $\Delta f = \frac{T_d}{Tm} FSR_M$, where FSR_M is the FSR of the MZI. Upon determination of the offset frequency, the cavity FSR is determined by $FSR = f_m + \Delta f$.

Using the above results, the uncertainty of cavity FSR is given by

$$\delta FSR = \delta f_m + \frac{T_d}{Tm}\delta FSR_M + \frac{\delta T_d}{Tm} FSR_M + \frac{T_d \delta T_m}{T_m^2} FSR_M. \tag{2.1}$$

The first term on the R.H.S of equation (2.1) is the uncertainty of the modulation frequency. It is determined by frequency uncertainty of the RF synthesizer, which is negligible compared with the other terms (less than 1 Hz).

Concerning the second term in equation (2.1), the FSR of the MZI is measured to kHz level uncertainty by sending a CW external-cavity diode laser into the MZI and measuring the power spectral density (PSD) using a balanced photodetector. When the laser frequency is set to the quadrature point of the MZI, the frequency noise of the laser is discriminated by the MZI fringes.

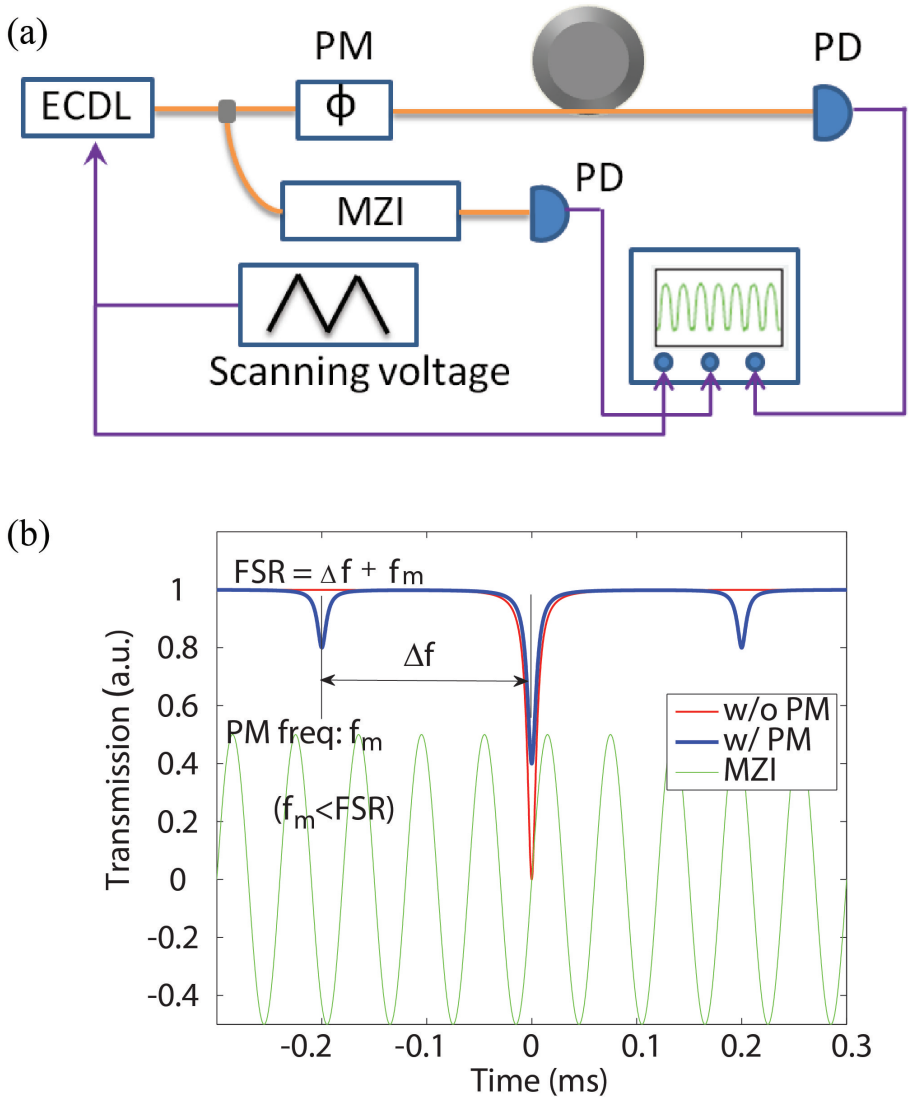

Figure 2.1: **Experimental setup.** (a) A schematic is shown for the sideband spectroscopy method used to measure dispersion. A phase modulator (PM) creates sidebands on a probe laser that are set to coincide approximately with the cavity FSR. Also, a Mach-Zehnder interferometer creates a reference spectrum to measure the offset frequency Δf. The laser is scanned so as to produce the spectrum shown in panel (b). (b) Schematic traces of the sideband spectroscopy are shown. When the phase modulation is "off" the red trace is observed showing that the laser is scanning through a single cavity resonance. With the phase modulation "on" and with its frequency set to be close in value to the cavity FSR, three spectral peaks appear as the two phase modulation sidebands scan through their respective cavity resonances (neighboring the resonance probed by the scan-laser, carrier wave). By using the green interferometer trace to measure the offset Δf and adding this offset to the phase modulation frequency, the cavity FSR can be measured.

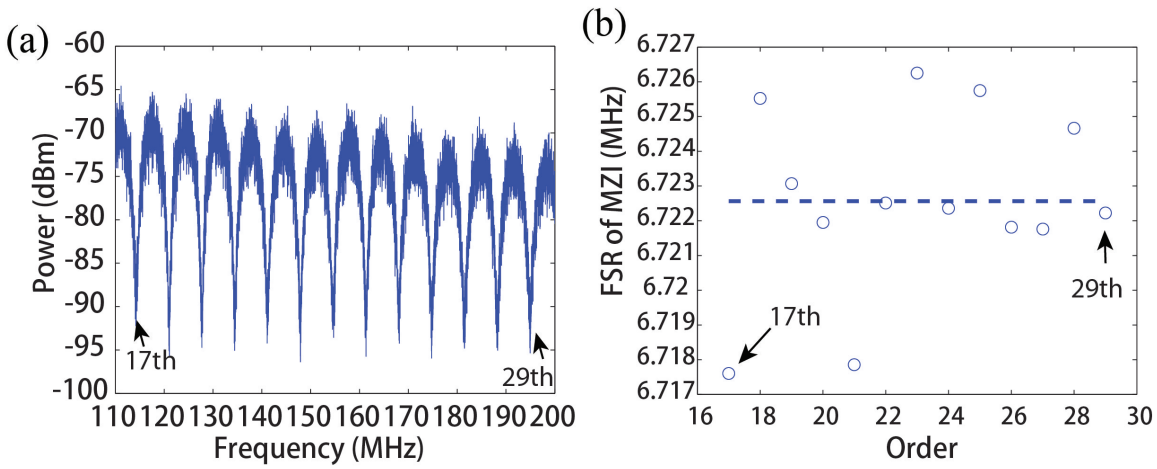

Figure 2.2: **Measurement of the FSR of the Mach Zehnder interferometer (MZI).** (a) Measured power spectrum of the photocurrent output from a balanced photodetector whose inputs detect the complementary outputs of the MZI. For this measurement the laser frequency is close to a quadrature point of the MZI and the spectral measurement extends from 110 to 200 MHz. (b) FSR of the MZI extracted from each order in (a). The dashed line is the average.

As shown in [7, 22] the PSD is then proportional to $\mathrm{sinc}^2(\tau_d f)$, where $\tau_d = \frac{1}{FSR_M}$ is the delay on the MZI. Thus the periodic spectral minima of the PSD can be used to extract the MZI FSR accurately. Figure 2.2a gives the spectrum of the MZI outputs from 110 to 200 MHz, which spans the 17th to 29th spectral minima of the MZI. The frequency location of each minima was divided by its order to create the plot of MZI FSR values in figure 2.2b. The average MZI FSR is 6.723 MHz ± 2.7 kHz. The offset frequency, Δf , is about 1–5 times the FSR of the MZI, which means $\frac{T_d}{Tm} \approx$ 1–5. As a result, the error contribution from the second term in equation (2.1) is no larger than ±15 kHz.

Finally, we consider the error contributions from the third and fourth terms in equation (2.1). In practice, these errors are on the order of 100 kHz in our measurement, based on repetitive measurements of the cavity FSR for one specific cavity mode using the method described above. For instance, 10 measurement of a 6 mm disk resontor with a cavity Q of 200 million gives an FSR of 10.8230 GHz ± 109 kHz. As a result, the overall uncertainty in measurement of microcavity FSR is set by these contributions.

2.3 Cavity Transverse Mode Spectroscopy

We apply the above approach to measure the FSR of different transverse modes of the same cavity. Comparison to finite element modeling then enables a mapping of spectral peaks with spatial modes of the resonator. The TE modes of a 6 mm wedge resonator (FSR of approximately 10.8 GHz) are characterized. Details on the fabrication and properties of this resonator are presented in [7], as well in in chapter 1. Briefly, however, these silica-based devices are fabricated on a silicon wafer using

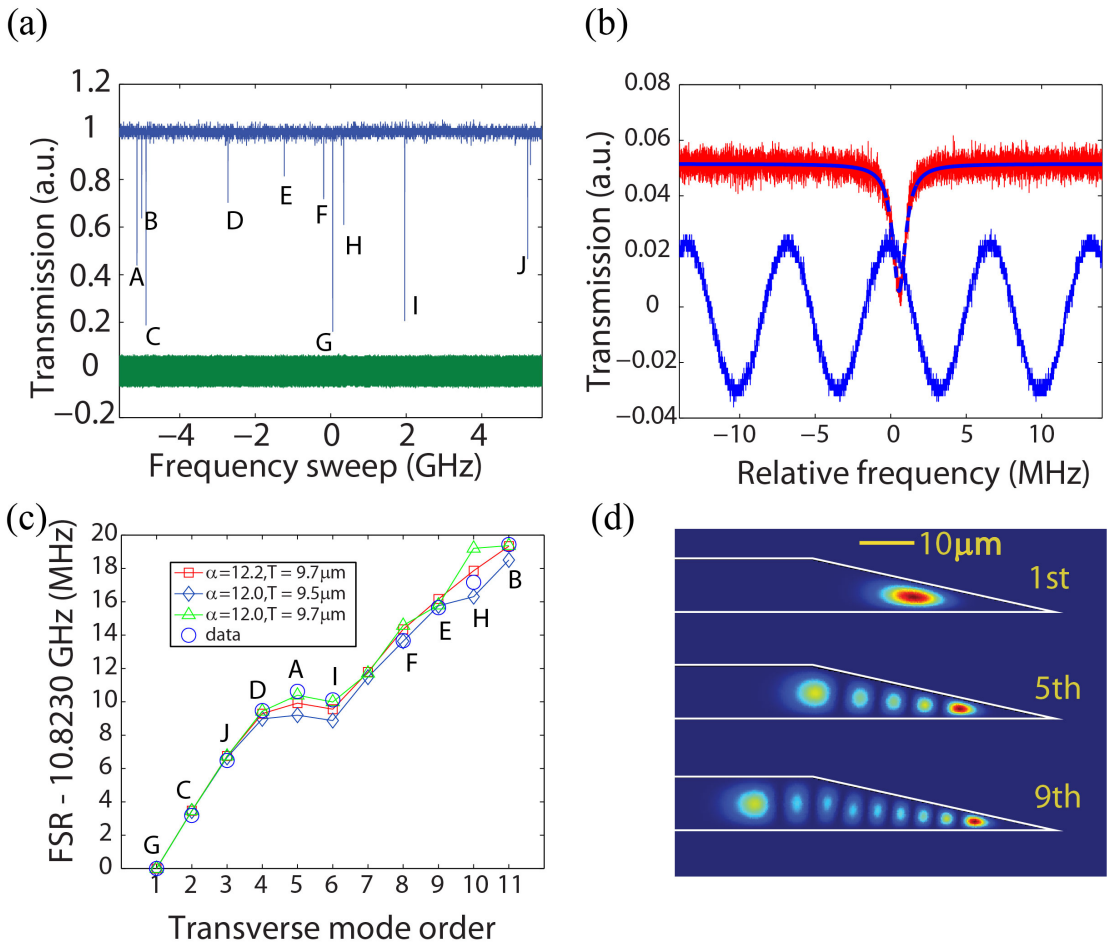

Figure 2.3: **Cavity transverse mode spectroscopy** (a) Transmission spectrum for a 6 mm wedge resonator. Multiple transverse modes (labeled from A to J) are shown within the frequency sweep of one FSR (10.8 GHz). The lower green trace is the Mach-Zehnder reference inteferometer (MZI) (FSR of the MZI is 6.723 MHz, MZI fringes are resolved in panel (b)). By using the MZI fringes and the calibrated MZI FSR, the original horizontal axis (time span, as shown in figure 2.1b) can be converted to frequency span. (b) Zoom-in measurement of the peak G in panel (a). The Lorentzian fit shows a loaded cavity linewidth of 1.03 MHz. This is also the fundamental mode indicated in panels (c) and (d). (c) Mapping of the cavity transverse-order to each spectral peak by comparing the FSR measurement with FEM simulation. Three slightly different cavity geometries are used for FEM simulation, and the FSR of the simulated transverse modes maintains the sequence regardless of geometry. (d) Intensity profile of the 1st, 5th and 9th transverse-order modes calculated by FEM. The corresponding spectral peaks are given to the right of the profile.

only lithography and a combination of wet and dry etching. They have optical Q factors ranging from several hundred million to nearly 1 billion. Their cross section is wedge like and the device characterized in figure 2.3 has a wedge angle $\alpha \approx 12°$ in a silica oxide with thickness $T \approx 10$ μm (measured using an SEM). Schematic cross sections of the device showing three transverse modes are illustrated in figure 2.3d. Optical coupling uses a fiber taper coupler [13, 14].

In figure 2.3a a spectral scan encompassing one FSR is shown. By scanning over two FSRs it is possible to identify repeating peaks that are associated with a particular transverse mode family. The various spectral peaks shown correspond to distinct transverse modes of the device, and are labeled from A to J. In figure 2.3b a "zoom-in" spectrum in the vicinity of peak G is shown to illustrate the measurement technique detailed in figure 2.1. Also shown in figure 2.3b is the Mach-Zehnder reference trace. Measurement results giving the FSR for each transverse mode are provided in figure 2.3c (data are circles). Note that the transverse mode dispersion introduces a difference of about 1 MHz in the FSR of neighboring transverse modes. This difference is easily resolved as the measurement uncertainty is about 100 kHz (see discussion in previous section). In order to identify the cavity modes, we calculate the FSR of different transverse-order modes by FEM simulation in a commercial FEM solver (COMSOL multiphysics). The simulation method is based on the 2-D simulation of the whispering-gallery modes (WGM) of axisymmetric resonators described in [23]. The calculated FSR values are plotted in figure 2.3c for three, slightly different, cavity dimensions (wedge angle and disk thickness). Several other geometries were also simulated, however, the three shown gave the best agreement over the range of modes measured. From the three FEM plots (indicated by triangles, diamonds, and squares), it can be seen that a small perturbation of the cavity dimension maintains the FSR sequence of different orders. Moreover, the three FEM plots are in reasonable agreement with the data. (The 7th transverse mode order is not identified. The reason may be due to unfavorable coupling position or phase match of taper-fiber coupling). Through this comparison it was possible to map each spectral peak to a particular transverse mode family. Several identifications have been made in figure 2.3d, including the fundamental mode "G." It is interesting to note that this fundamental mode has the smallest FSR of all of the modes. This is expected since the fundamental mode should also exhibit the largest effective index. Also, the slight plateau in the FSR versus mode order (see figure 2.3c) is associated with the higher-order-modes extending radially inward beyond the wedge region.

This mapping is based on the increment of the FSR of each transverse mode order; and if the FSRs between two neighboring pairs of transverse modes are close to each other, for example, the 4th-6th modes in figure 2.3c, the modes may not be mapped accurately. The labeling of spectral peaks "D, A, I" to mode order 4, 5, and 6 is therefore only one possible mapping. However, having the FSR of each transverse mode is important by itself and can differentiate between low order and high order modes. It can be particularly usefully in studying stimulated Brillouin lasers [7, 8] and

microcomb generation in microresonators [6, 19].

2.4 Dispersion Characterization of Wedge Disk Resonators

To measure the dispersion within a single transverse mode family, the above technique is repeated for a sequence of spectral peaks having the same transverse mode order. However, because the FSR dispersion of these resonators, $\Delta FSR = FSR_m - FSR_{m-1}$, is usually very small (in the order of 1-10 kHz/FSR, depending on the resonator diameter), it is necessary to measure the cavity FSR over multiple FSR separations. Figure 2.4a shows the cavity FSR for a 2 mm cavity ($\alpha \approx 20°$, T ≈ 8 μm) plotted versus the relative cavity azimuthal mode number M (FSR number) measured around the 1550 nm region. The dashed line is a linear fit which gives a dispersion of 12.2 kHz/FSR. This value is in good agreement with the simulated value (12.8 kHz/FSR, simulation is based on the 2D FEM solver of the whispering-gallery modes of axisymetric microcavities as described in [23]). The RMS error of the FSR measurement is 180 kHz (for a cavity Q of 150 million), which gives a relative precision of 5.5×10^{-6} for a cavity FSR of 32.9382 GHz. In figure 2.4b measurements of the FSR dispersion of disk resonators with three different wedge angles ($\alpha \approx 10°$, $20°$, $30°$) and at two different wavelengths (1550 and 1310 nm) are presented along with the calculated ΔFSR. Figure 4c converts the FSR dispersion values to the more widely used dispersion parameter, $D \equiv \frac{d}{d\lambda}\left(\frac{1}{v_g}\right)$, using $\Delta FSR \approx \frac{c^2\lambda^2 D}{4\pi^2 n^3 R^2}$ [24], where R is the cavity radius, n is the refractive index and λ is the wavelength. Also, the material dispersion parameter, D_M (calculated from the Sellmeier equation [25]), and the geometric dispersion parameter ($D_G = D - D_M$) are plotted. From figure 2.4b and c, it can be seen that the measurement data (in markers) agree reasonably well with the simulation. Also, note that resonators having smaller wedge angles feature larger geometrical dispersion. This is consistent with the centroid of the mode's "orbit" around the resonator being shifted radially inward as wavelength increases, and hence smaller wedge angles enhancing this tendency.

2.5 Conclusion

In conclusion, we have demonstrated a simple and accurate approach to measure the FSR of microcavities by introducing external phase modulation and frequency calibration with an MZI. This FSR measurement method is applicable for high-Q resonators with microwave rate FSR and has a precision of 5.5×10^{-6} (given a cavity Q of 150 million). We have used this approach to measure the FSRs of different cavity transverse modes and find that the cavity transverse mode can be identified from their FSRs when comparing with FEM simulation results. Finally, we have applied the FSR-measurement approach to characterize cavity dispersion, which is important in many nonlinear photonic applications, such as the generation of microcombs.

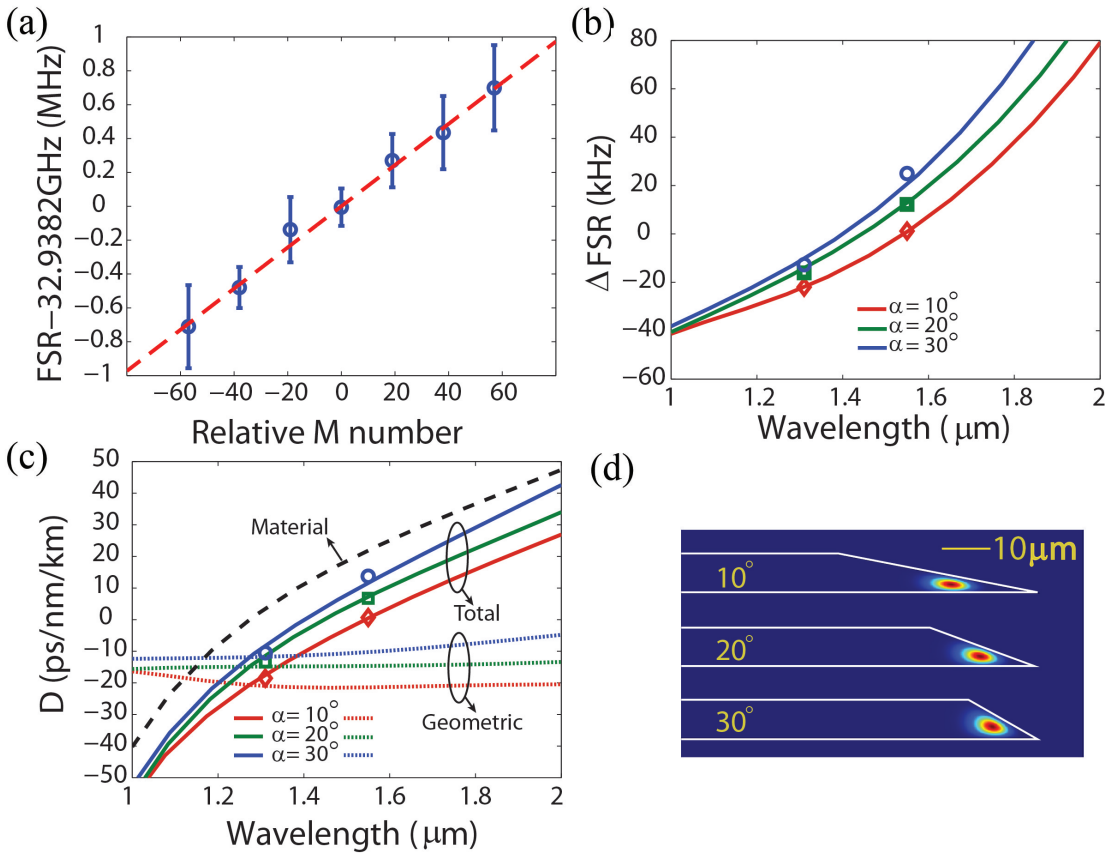

Figure 2.4: **Measurement of dispersion at two wavelengths for three cavity geometries.** (a) Measured cavity FSR (wrt 32.9382 GHz) for 2 mm resonator ($\alpha \approx 20°$, oxide thickness, T $\approx$ 8 μm) plotted versus relative azimuthal mode number M around the 1550 nm spectral region. The dashed, red line is a linear fit giving 12.2 kHz/FSR dispersion. (b) Measured (colored makers) and simulated cavity dispersion, ΔFSR, as a function of wavelength for 2 mm disk resonators with three wedge angles ($\alpha \approx 10°$, 20° and 30°, T $\approx$ 8 μm). (c) Solid lines give the dispersion parameter, D, converted from the ΔFSR values in (b), using $\Delta FSR \approx \frac{c^2\lambda^2 D}{4\pi^2 n^3 R^2}$ [24]. The dashed line is the silica material dispersion from the Sellmeier equation. The three dotted lines are the geometric dispersion, obtained by subtracting the material dispersion from the total dispersion. The measurement data points are given as markers. (d) Intensity profile for 2 mm resonators with 10°, 20°, and 30° wedge angles.

Chapter 3

Microresonator-based Frequency Comb on a Chip

3.1 Introduction

Optical frequency combs provide direct phase-coherent link between optical and RF frequencies, and enable precision measurement of optical frequencies [26–29]. It is now a vital tool for optical clocks [30], precision spectroscopy [31], attosecond physics [32], ultralow-noise microwave generation [33], and astronomical spectrogram calibration [34–36]. Conventional frequency combs are based on octave spanning, self-referenced ultrafast lasers, mainly Ti:Sapphire, Er:fiber, and Yb:fiber mode locked lasers. These mode locked lasers usually have a dispersion-compensated laser cavity (e.g., via chirped mirrors or dispersion-compensated fibers), a gain medium and a high power CW pump laser, and a medium that enables mode locking (e.g., Kerr-lens mode locking or a saturable absorber). The repetition rate (i.e., comb line spacing) of the conventional frequency combs usually operates in the range of 100 MHz - 1 GHz, and the highest repetition rate demonstrated so far is a 10 GHz Ti:Sappire comb [37].

In recent years, a new class of frequency combs have emerged based on parametric frequency conversions in dielectric microresonators [38]. The combination of high optical Q factor and the Kerr effect optical nonlinearity enables optical parametric oscillation in microcavities [39, 40]. Concomitant, nondegenerate four-wave-mixing multiplies the initial Stokes and anti-Stokes waves creating a route to generation of frequency combs [6, 38]. Figure 3.1 illustrates the generation of microreonator-based frequency combs, pumped by a CW laser in a high-Q microcavity with Kerr-nonliearity. These microresonator-based frequency combs (microcombs or Kerr-combs) can potentially miniaturize the numerous applications of conventional frequency combs. Also, microcombs are complimentary to conventional frequency combs in applications which require large line spacings from 10 to 100 GHz, especially in line-by-line pulse shaping for arbitrary waveform generation, astronomical spectrograph calibration and high-speed telecommunications. In addition, in contrast to population inversion and

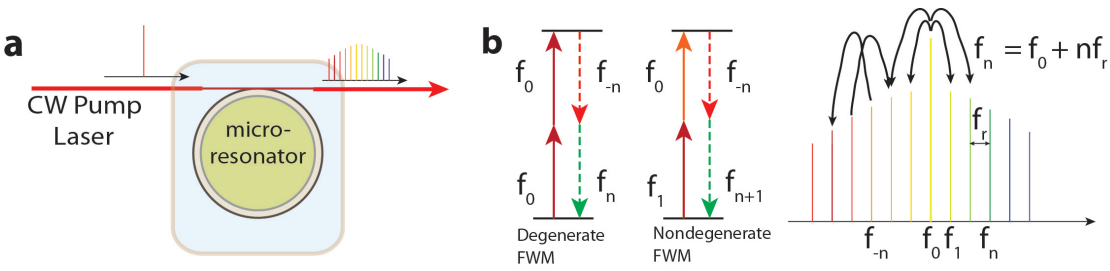

Figure 3.1: **Concept of microresonator-based frequency comb generation** (a) A simple sketch showing microcomb generation from microresonators pumped by a CW laser. (b) Microcomb generation is based on cascaded four-wave-mixing, e.g., degenerate (left) and nondegenerate (middle) FWMs. Microcomb lines have two degrees of freedom, i.e., the comb line spacing f_r, and the offset frequency (pump frequency) f_0.

stimulated emisssion in a laser, microcombs arise from parametric frequency conversion based on phase-matched four-wave-mixing processes. This provides advantages of broad bandwidth tunability that is not limited by specific atomic or molecular transitions.

So far, microcombs (or Kerr combs) have been demonstrated using silica microtoroids [38], CaF_2 diamond-milled rods [41, 42], fiber Fabry-Perots [43], silicon-nitride rings on silicon [44, 45], high-index silica rings on silicon [46] and fused-quartz cavities [47]. Octave span operation has been demonstrated in microtoroids [48] and in silicon nitride resonators [49], with line spacings of 850 GHz and 226 GHz, respectively; full control and stabilization of microcomb lines have been demonstrated for a 86 GHz silica microcomb with 20 nm bandwidth [50]. Microwave-repetition-rate less than 40 GHz (Ka band) is possible in a range of machined bulk devices [41, 42, 47].

A priority in the development of microcombs is the realization of broadband (ideally octave spanning) spectra at detectable microwave repetition rates for comb self-referencing. However, access to these rates involves pumping larger mode volumes and hence higher threshold powers. Moreover, threshold power sets both the scale for power per comb tooth and also the optical pump. Along these lines, in this chapter, we show that a class of resonators having surface-loss-limited Q factors can operate over a wide range of repetition rates with minimal variation in threshold power. The newly developed, surface-loss-limited silica resonator descripted in chapter 1 illustrates the idea. Comb generation on mode spacings ranging from 2.6 to 220 GHz with overall low threshold power (as low as 1 mW) is demonstrated [51, 52]. The work here are the first silicon-chip-based microcombs to access microwave rate less than 86 GHz [51]. And indeed, the 2.6 GHz microcomb demonstrated here has the lowest repetition rate achieved to date for any microcomb. A record number of comb lines for a microcomb (around 1900) is also observed with pump power of 200 mW. The ability to engineer a wide range of repetition rates with these devices is also used to investigate a recently observed mechanism in microcombs associated with dispersion of subcomb offset frequencies. We observe high-coherence, phase-locking in cases where these offset frequencies are small enough so as

to be tuned into coincidence. In these cases, a record-low microcomb phase noise is reported at a level comparable to an open-loop, high-performance microwave oscillator.

3.2 Optical Parametric Oscillation Threshold

The Hamiltonian describing a three mode system of the pump mode a (cavity eigenfrequency ω_0), signal mode b_s (cavity eigenfrequency ω_{s0}), and the idler mode b_i (cavity eigenfrequency ω_{i0}) interacting by the third-order nonlinearity is given by [53]:

$$\begin{aligned} H &= H_0 + V; \\ H_0 &= \hbar\omega_0 a^\dagger a + \hbar\omega_{s0} b_s^\dagger b_s + \hbar\omega_{i0} b_i^\dagger b_i; \\ V &= -\frac{1}{2}\hbar g : (a + b_s + b_i + h.c.)^4 : \\ &= -\frac{1}{2}\hbar g \left(a^\dagger a^\dagger a a + b_s^\dagger b_s^\dagger b_s b_s + b_i^\dagger b_i^\dagger b_i b_i \right) \\ &\quad -2\hbar g (b_i^\dagger b_s^\dagger b_s b_i + a^\dagger b_s^\dagger b_s a + a^\dagger b_i^\dagger b_i a) \\ &\quad -\hbar g (b_i^\dagger b_s^\dagger a a + a^\dagger a^\dagger b_s b_i), \end{aligned} \tag{3.1}$$

where $g = \frac{\hbar\omega_0^2 c n_2}{n_0^2 V_{eff}}$ is the third-order nonlinear coupling parameter. And n_2 is the Kerr nonlinear refractive index such that $n = n_0 + n_2 I$, c is the speed of light, n_0 is the linear refrative index, and V_{eff} is the effective nonlinear mode volume. The physical meaning of g is the frequency shift of the cavity resonance due to Kerr-nonlinearity caused by one photon. The interaction part of the Hamiltonian V contains three types of third-order nonlinear interactions: self-phase modulation, cross-phase modulation and four-wave mixing, respectively.

Using the Heisenberg equation of motion, i.e.,

$$\frac{da}{dt} = \frac{1}{i\hbar}[a, H]; \tag{3.2}$$

and introducing the slowly varying field amplitudes for the pump (A), signal (B_s) and idler (B_i), we arrive at the following coupled mode equations of the field amplitudes for the three modes:

$$\begin{aligned} \dot{A} &= -[i(\omega_0 - \omega) + \frac{\kappa}{2}]A + ig\left[|A|^2 + 2|B_s|^2 + 2|B_i|^2\right]A + 2igA^* B_s B_i + \sqrt{\kappa_{ex}}s; \\ \dot{B_s} &= -[i(\omega_{s0} - \omega_s) + \frac{\kappa}{2}]B_s + ig\left[2|A|^2 + |B_s|^2 + 2|B_i|^2\right]B_s + igB_i^* A^2; \\ \dot{B_i} &= -[i(\omega_{i0} - \omega_i) + \frac{\kappa}{2}]B_i + ig\left[2|A|^2 + 2|B_s|^2 + |B_i|^2\right]B_s + igB_s^* A^2; \end{aligned} \tag{3.3}$$

where ω, ω_s and ω_i are the carrier frequencies of the external pump (A), and the generated signal (B_s) and idler (B_i). κ is the loaded cavity photon decay rate, and κ_{ex} is the external cavity decay

rate. And $s = \sqrt{\frac{P_{in}}{\hbar\omega}}$ denotes the amplitude of the pump power. Due to cavity gemotrical and material dispersion, $\omega_{s0} - \omega_0 \neq \omega_0 - \omega_{i0}$, which is a frequency mismatch. From equation (3.3), it is worth to note that nonlinear phase shift caused by cross-phase modulation (XPM) is twice as large as the nonlinear phase shift due to self-phase modulation (SPM). Thus roughly speaking, parametric oscillation occurs once the cold-cavity frequency mismatch is compensated by the nonlinear frequency shift due to by SPM and XPM, and the pump laser detuning.

By solving the algebra equation (3.3) at steady state, it is easy to shown that the parametric oscillation threshold is given by [39, 53, 54]:

$$P_{th} \approx \frac{\kappa^2 \hbar\omega_0}{8g\eta} = \frac{\kappa^2 n_0^2 V_{eff}}{8\eta\omega_0 c n_2}, \tag{3.4}$$

where $\eta \equiv \frac{\kappa_{ex}}{\kappa}$ is the normalized external coupling parameter. Equation (3.4) can be manipulated into the following form:

$$P_{th} \approx \frac{\pi}{8\eta}\frac{n}{n_2}\frac{\omega}{\Delta\omega_{FSR}}\frac{A}{Q_T^2}, \tag{3.5}$$

where $\Delta\omega_{FSR}$ (ω) is the angular free-spectral-range (optical frequency), A is the nonlinear mode area, and Q_T is the loaded optical Q factor.

3.3 Comparison with Prior Various Microcombs

From equation (3.5), it can be seen that the important parameters for low-threshold microcomb generation are the nonlinear refractive index n_2, nonlinear mode area A, cavity FSR, and the optical Q factor. Other parameters held fixed, it is clear that decreasing FSR (to achieve microwave-rate comb operation) adversely impacts turn-on power. This is because a smaller FSR means a larger cavity size and mode volume to pump. Moreover, in whispering-gallery resonators, the mode area, A, will generally increase with decreasing FSR, thereby causing further degradation of power requirements. At the same time, it is interesting to note the positive impact of increasing Q factor. Higher optical Q creates larger resonant buildup so that a given coupled power induces a larger Kerr nonlinear coupling of signal and idler waves. It also reduces oscillation threshold since optical loss is lowered. The combined effect leads to the inverse quadratic behavior in equation (3.5).

Table 3.1 summaries the important parameters of various microcombs in a variety of materials and devices, prior to our work. The last row is the parameters of our work [51, 52]. Note that our planar silica disk resonator has the highest optical Q for silicon-chip-based devices, and we are the first to demonstrate chip-based microcombs with microwave repetition rate less than 86 GHz. We demonstrated 8.7 - 33 GHz repetition rates of silicon-chip-based microcombs in 2011 [51] and even 2.6 GHz repetition rate from a 25 mm disk resonator in 2012 [52]. Microwave repetition rate less than 40 GHz (Ka band) is very preferable because the current microwave industry provides easy access

to various RF components (e.g., amplifier, syntheziser, divider, mixer, etc.) below this frequency. Also, the microwave repetition rate can be conveniently detected with a commercial-grade high-speed photodetector. Therefore it facilitates the study of microcomb phase noise, line-spacing uniformity, and feedback control. Moreover, microwave repetition rate for an octave-spanning microcomb would be highly desirable because it can be fully stabilized using f-2f nonlinear interferometry for offset frequency stabilization, and repetition rate detection for stabilizing the comb line spacings.

Cavity	Q (typ.)	n_2 (cm^2/W)	A_{eff} (μm^2)	Integration on chip	Smallest Rep rate demo'd	Pump power range (mw)	Ref.
Silica toroid	$\sim 10^8$	2.2×10^{-16}	10	difficult	86 GHz (2008)	10–1000	[50]
Silicon Nitride	$\sim 10^6$	2.5×10^{-15}	0.5	yes	204 GHz (2011)	10–1000	[55]
Silicon Nitride	$\sim 10^6$	2.5×10^{-15}	0.5	yes	115 GHz (2011)	10–1000	[45]
Hydex silica	10^6	5.7×10^{-16}	0.75	yes	200 GHz (2009)	10–100	[46]
Fused quartz	5×10^8	2.2×10^{-16}	100	no	36 GHz (2011)	1–10	[47]
CaF_2, MgF_2	6×10^9	3.2×10^{-16}	2500	no	9.9 GHz (2010)	1–10	[56]
This work	3×10^8	2.2×10^{-16}	30	yes	8.7–33 GHz (2011)	1–100	[51]

Table 3.1: **List of microcomb parameters for various platforms demonstrated before our work.** The last row is our work using the UHQ planar silica disk resonator.

.

3.4 Low-threshold Microcombs from Surface-loss-limited Silica Disk Resonators

The experiment setup for microcomb generation is given in figure 3.2. An external-cavity diode laser in the C band is amplified using an erbium-doped fiber amplifier (EDFA) and then coupled to the disk resonator using a tapered fiber coupler [13, 14]. The pump (TE polarized) is thermally

locked to the resonance [57]. The generated comb lines from the disk resonator are then coupled to the same taper fiber through which spectral monitoring or photodetection (demodulation) is straightforward. Spectral monitoring is performed using both a telecom optical spectrum analyzer (OSA) (600 - 1700 nm) and an infrared OSA (1200 - 2400 nm). Comb lines are demodulated on a high-speed photodetector having a bandwidth of 50 GHz. The resulting microwave beat notes are analyzed on an electrical spectrum analyzer (ESA) and also using a phase noise analyzer (PNA).

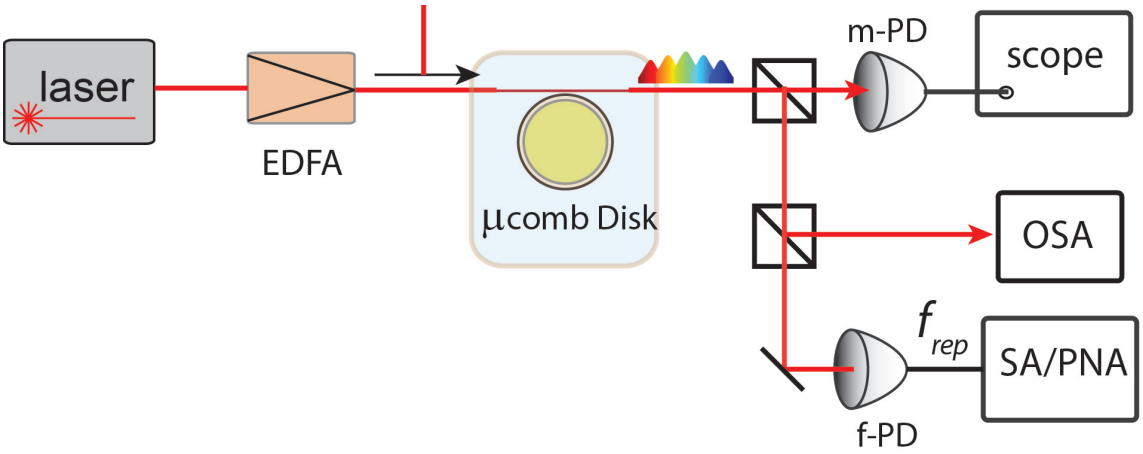

Figure 3.2: **Experimental setup for microcomb generation.** A tunable CW laser is amplified by erbium-doped-fiber-amplifier (EDFA) and then coupled to the disk resonator by tapered fiber. The generated microcombs are characterized by a monitor-photodetector (m-PD) with 125 MHz bandwidth, a fast-photodetector (f-PD) with 50 GHz bandwidth for RF spectrum analysis, and optical spectrum analyzers (OSA).

In figure 3.3a, the comb spectrum of a 2 mm diameter disk (free-spectral-range, FSR, is 33 GHz) having a threshold of 2 mW (figure 3.3b) is shown for excitation only slightly above threshold. This resonator featured an intrinsic Q of 270 million. Only modest pumping above threshold is required to generate a dense comb spectrum on the native line spacing. About 200 comb lines are generated with coupled pump power of only 7.5 mW (figure 3.3c and 3.3d). These are the first demonstration of silicon-chip based mirocombs with line spacing (repetition rate) less than 86 GHz [51, 52].

From equation (3.5), it is seen that the OPO threshold increase inversely with cavity FSR, given the other parameters fixed. Thus in order to maintain low OPO threshold as the size of the resonator increases, the optical Q of the cavity needs to increase. Intuitively, the linear increase of optical Q with regard to diameter will maintain a relative constant cavity finesse, F. Therefore the resonant power enhancement inside the cavity is the same (the intracavity circulating power, $P_{circ} \sim \frac{FP_{in}}{\pi}$ at critical coupling). The dependence of optical Q in whispering-gallery resonators versus resonator diameter (FSR) depends strongly on whether the round-trip losses are set by surface or material losses. In the material-loss limit, Q is independent of FSR and turn-on power will therefore degrade as a comb transitions from millimeter-wave to microwave repetition rates. However,

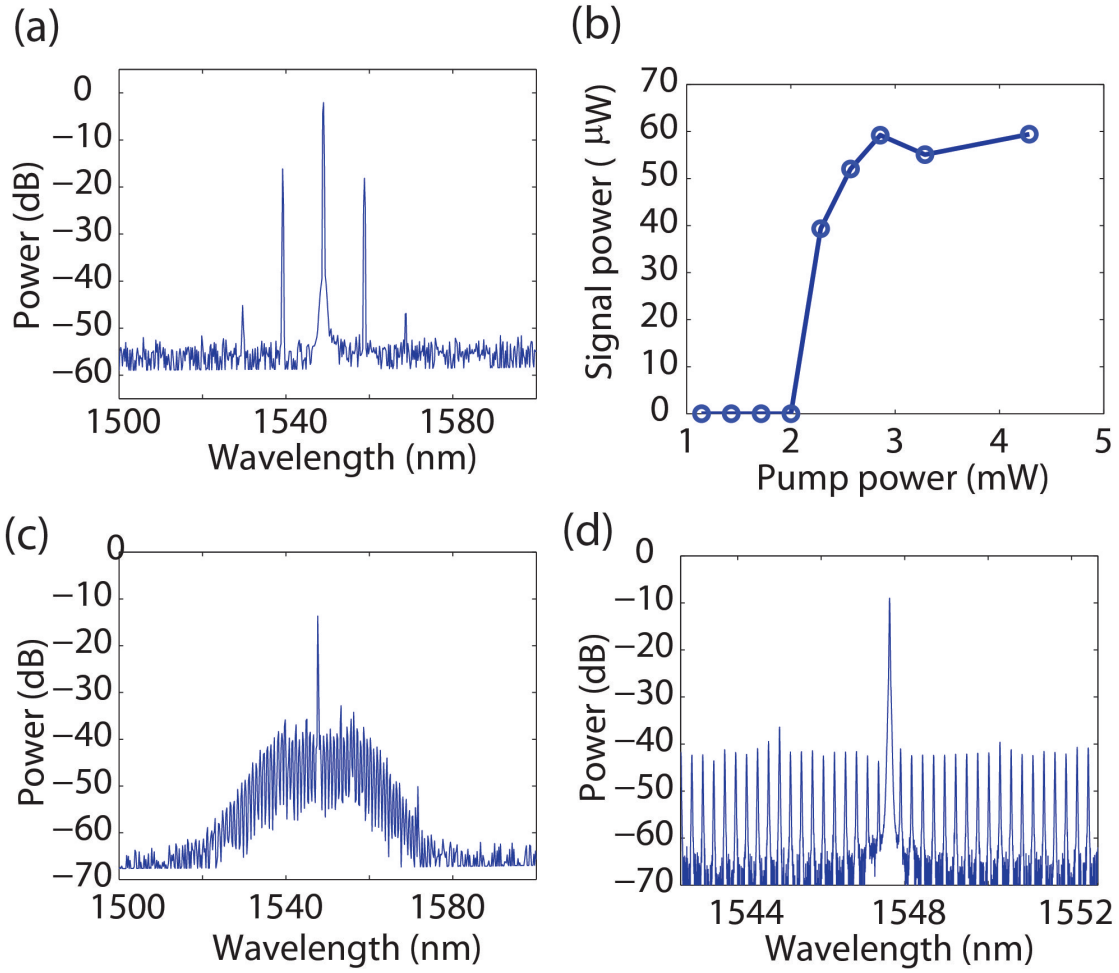

Figure 3.3: **microcomb spectra from a 2 mm disk resonator just above threshold** (a) Optical spectrum of the OPO comb lines from a 2 mm disk resonator just above threshold. (b) The power of the first oscillating, higher-frequency, comb line is plotted versus pump power and shows a threshold turn-on power of approximately 2 mW. (c) Approximately 200 comb lines are generated with coupled pump power of 7.5 mW. (d) A reduced span scan of the spectrum in (c) is shown with comb lines resolved by the OSA.

in surface-loss-limited resonators, the resonator Q factor increases (nearly proportionally) with resonator diameter. This happens because the optical field strength at the resonator surface decreases with increasing resonator diameter. In such cases, the surface-loss-limited behavior of Q offsets the FSR and area dependences, leading to low, turn-on power (and total required power) across a wide range of repetition rates.

To study the effect of surface-loss-limited Q behavior on threshold, a series of devices having a range of diameters were fabricated and characterized. Figure 3.4 shows a plot of the parametric oscillation threshold versus diameter (lower axis) and FSR (upper axis) for several of the devices. Threshold levels associated with different resonator pump modes are displayed and measured variations result from changes in both Q factor and modal area for each pump mode. The lower-order transverse modes of the device are expected to give the lower threshold turn-on power since these have higher Q and smaller mode area [7]. Microcomb oscillation at rates from 2.6 GHz (25 mm diameter) to 220 GHz (0.3 mm) has been observed. The behavior of threshold versus FSR can be understood by considering the dependence of both Q and A versus diameter D. Modeling shows that the mode area, A, scales approximately like $D^{2/3}$. Over the range of diameters for which the resonator is surface-loss-limited, the Q factor scales approximately linearly with D (i.e., the resonator has an approximately constant finesse over this range). In this surface-loss-limited regime, equation (3.5) predicts that the threshold scales like: $P_{th} \sim D^{-1/3}$. Ultimately, at large diameters, the Q factor will saturate to a high, constant value. In this limit, equation (3.5) gives: $P_{th} \sim D^{5/3}$. These two regimes are illustrated in figure 3.4 by the trend curves: $D^{-1/3}$ (dashed curve) and $D^{5/3}$ (dotted curve). The threshold is below 5 mW over a range of FSRs spanning 4.4 GHz to 220 GHz, demonstrating the beneficial effect of surface-loss-limited Q scaling. As an aside, the higher value of threshold for the 2.6 GHz device is a result of this device having a poorer Q factor of around 110 million due to accidental contamination.

Figure 3.5 shows a collection of microcomb spectra from disks with different diameters, excited just above threshold. The coupled pump power levels are all within 1-5 mW. The smallest disk (0.3 mm disk) shows the first oscillation line at the 3rd mode from the pump. Note that the number of the first oscillation line, $\mu \approx \sqrt{\frac{\kappa}{D_2}}$ [54], where D_2 is the difference between neighboring FSRs. These small resonators usually have a larger dispersion value ($D_2 \sim$ 100s kHz) than large resonators. Thus the first oscillation line is close to the pump mode for small resonators. As the cavity size increases, the first oscillation lines usually happens at 20–50 modes away from the pump, as shown in figure 3.5 when the diameter is greater than 1 mm. The first oscillation line is important to affect the microcomb phase noise in the RF domain as the comb grows to a fully-populated spectrum under higher pump power levels [54].

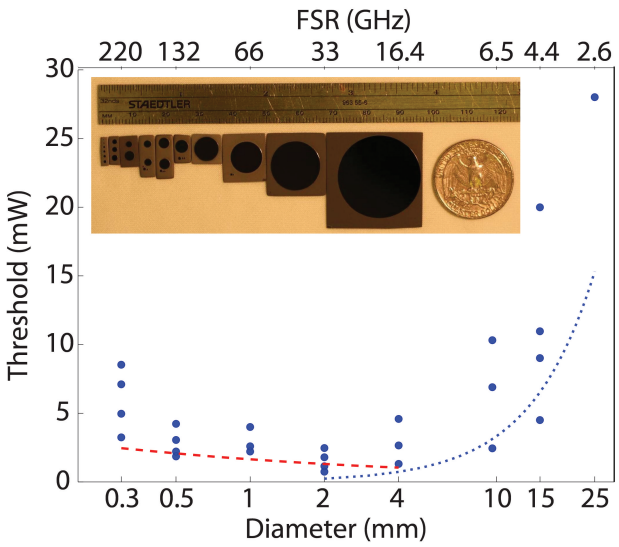

Figure 3.4: **OPO threshold dependence on disk diameter.** Plot showing measured microcomb threshold versus resonator diameter (lower axis) and FSR (upper axis). Also shown are the trend curves of the threshold data using $D^{-1/3}$ (dashed curve) and $D^{5/3}$ (dotted curve). Inset: A photograph of microcomb disk resonators ranging in diameter from 0.3 mm to 25 mm, all of which provide parametric oscillation and comb generation.

3.5 Broadband Microcomb Generation

While low threshold power is important, the total required optical pump power for comb operation also depends on threshold. Using the dimensionless, coupled, nonlinear equations-of-motion for microcombs [54]

$$\frac{\partial a_\mu}{\partial \tau} = -[1 + i\zeta_\mu]a_\mu + i \sum_{\mu' \leq \mu''} (2 - \delta_{\mu'\mu''}) a_{\mu'} a_{\mu''} a^*_{\mu'+\mu''-\mu} + \delta_{0\mu} f, \tag{3.6}$$

where a_μ is the dimensionless field amplitude, $f = \sqrt{8\eta g/\kappa^2}s = \sqrt{P/P_{th}}$ is the dimensionless external pump term, η is the coupling parameter (κ_{ex}/κ), and ζ_μ is the dimensionless dispersion parameter. It can be shown that the power in a comb tooth with mode index μ is given by

$$P_\mu = 4\eta^2 P_{th} \frac{\omega_\mu}{\omega_o} \left| a_\mu \left(\sqrt{\frac{P}{P_{th}}}, \zeta_\mu \right) \right|^2, \tag{3.7}$$

where $a_\mu \left(\sqrt{\frac{P}{P_{th}}}, \zeta_\mu \right)$ is the solution of the coupled equations (3.6), P is the pump power, and ω_μ (ω_o) is the frequency of the mode μ (pump). Here, any variation in the coupling parameter with μ is ignored. For a given dimensionless solution set, $\{a_\mu\}$, threshold power therefore sets the scale for comb power per tooth. Also, the solution set of $\{a_\mu\}$ only depends on the normalized pump term, f, and the normalized dispersion, ζ_μ. Thus for the same cavity dispersion, lower threshold power (P_{th})

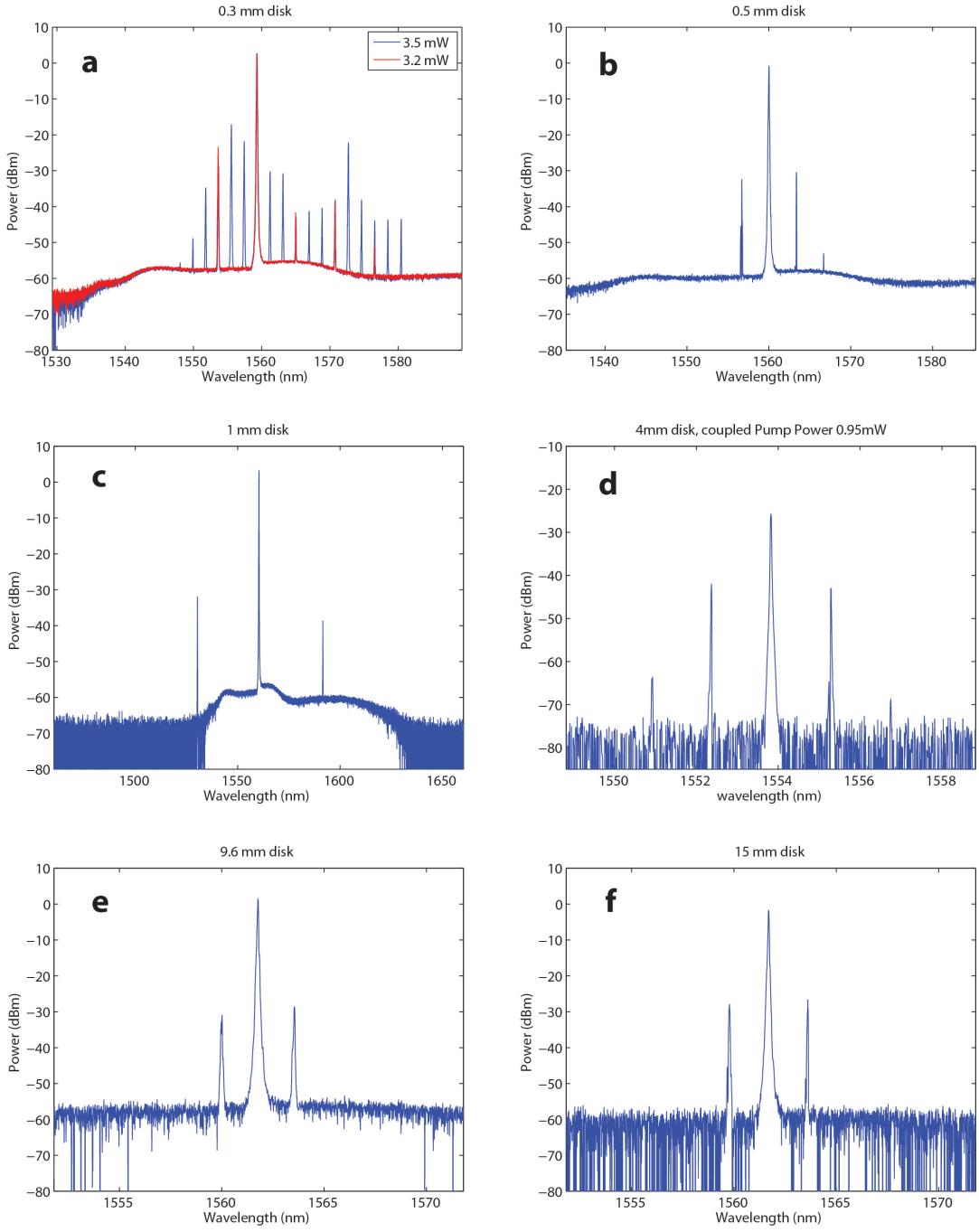

Figure 3.5: **Microcomb optical spectra for various sizes just above threshold.** The OPO thresholds are all within 1–5 mW. (a) Microcomb optical spectrum from 0.3 mm disk with excitation power 3.2 mW (red) and 3.3 mW (blue). The first oscillation line mode is the 3rd mode from the pump. (b) 0.5 mm disk. (c) 1 mm disk. (d) 4 mm disk. (e) 9.6 mm disk. (f) 15 mm disk.

will increase the normalized pumping parameter f, therefore improves the pumping efficacy of comb line generations. We would expect these features of threshold to exacerbate the power requirement of comb operation in the microwave regime. Therefore, higher optical Q not only lowers the OPO threshold, it also enhances the cascaded process of four-wave mixing and new comb line generation by improving the normalized pumping parameter.

The low OPO threshold for a wide range of disk sizes discussed in section 3.4 are advantageous for broadband microcomb generation at low to medium pump power levels. Figure 3.6 shows the efficient generation of broadband microcomb spectra with 66 GHz line spacing (1 mm disk) at different pump power levels. A microcomb spectra spanning close to 300 nm with only 8.4 mW coupled pump power is shown in figure 3.6a. As the pump power increases to 30 mW in figure 3.6b, the comb is more-densely populated and shortest-wavelength comb line extends to around 1260 nm. The clusterlike comb spectra around 1400 nm region is believed to be associated with anticrossing of cavity eigenmodes. As the pump power grows to around 200–300 mW, the comb spectra extends from around 1200 to 2000 nm, as shown in figures 3.6c–f. The comb span here is already 3/4 octave (106 THz) with 66 GHz line spacing. The shortest wavelength in figure 3.6f is 1060 nm.

Broadband microcomb spectra from a variety of disk sizes are also obtained. Figure 3.7a shows a 132 GHz microcomb spectrum with pump power 100 mW from a 0.5 mm disk. We can see that the comb lines extend towards the longer wavelength. This is because the zero-dispersion wavelength (ZDW) in a small disk size is above 1550nm (ZDW from pure materical dispersion is around 1320 nm). The strong geometric confinement in smaller disk sizes (e.g., 0.5 mm) will introduce a considerable amount of normal dispersion to shift the ZDW into longer wavelengths. Figure 3.7b shows a 37 GHz microcomb spectrum with coupled pump power 180 mW from a 1.8 mm disk. This comb spectrum extends more toward the shorter wavelength as the ZDW is shorter than 1550nm, and the longer wavelength has too much anomalous dispersion to prohibit efficient comb line generation. A 33 GHz microcomb spectrum with coupled pump power 200 mW from a 2 mm disk is shown in figure 3.7c, with around 500 nm bandwidth. This spectrum spans nearly half an octave (62 THz) and contains about 1900 comb lines, which is to the authors knowledge the largest number of comb lines so far generated from a microcomb. Finally, a microcomb spectrum with 22 GHz spacing and 170 nm bandwidth from a 3 mm disk with only 20 mW coupled pump power is shown in figure 3.7d.

It is also worth to discuss the detection methods of comb optical spectrum. Because a large amount of the pump laser power is bypassing cavity directly when cascade four-wave mixing happens, the microcomb spetrum is usually accompanied by a strong CW pump line. This CW pump line will rise the noise floor of the optical spectrum analyzer (OSA), due the limited dynamic range of the instrument. Also, under high power pumping conditions, the CW pump line will need to be attenuated prior to the OSA, which attenuates the comb line power also. Thus, a narrow band-reject

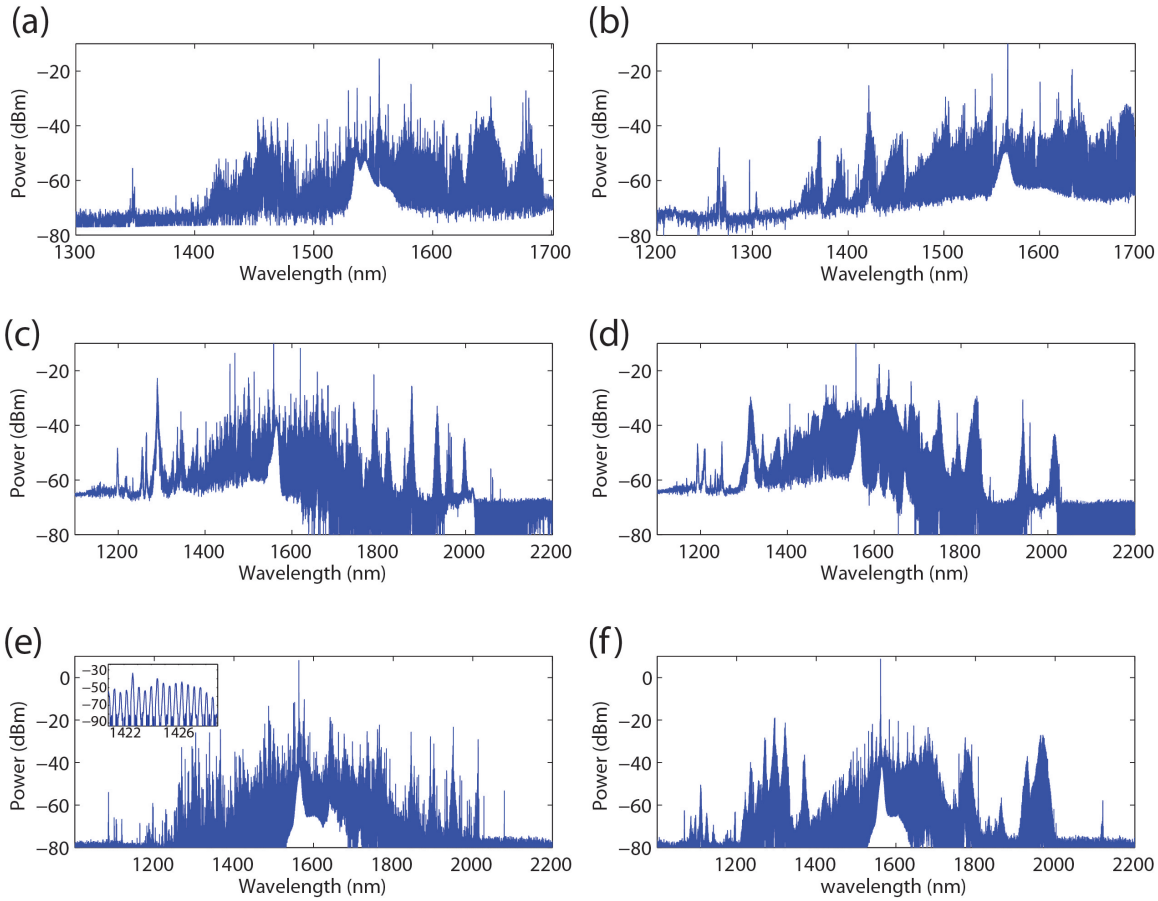

Figure 3.6: **Various broadband microcomb spectra (all 66 GHz spacing) from 1 mm disk resonators.** (a) A 66 GHz microcomb spectrum with coupled pump power only 8.4 mW. (b) A 66 GHz microcomb spectrum with coupled pump power only 30 mW. (c)–(f) Microcomb spectra from 1 mm disks pumped around 200–300 mW.

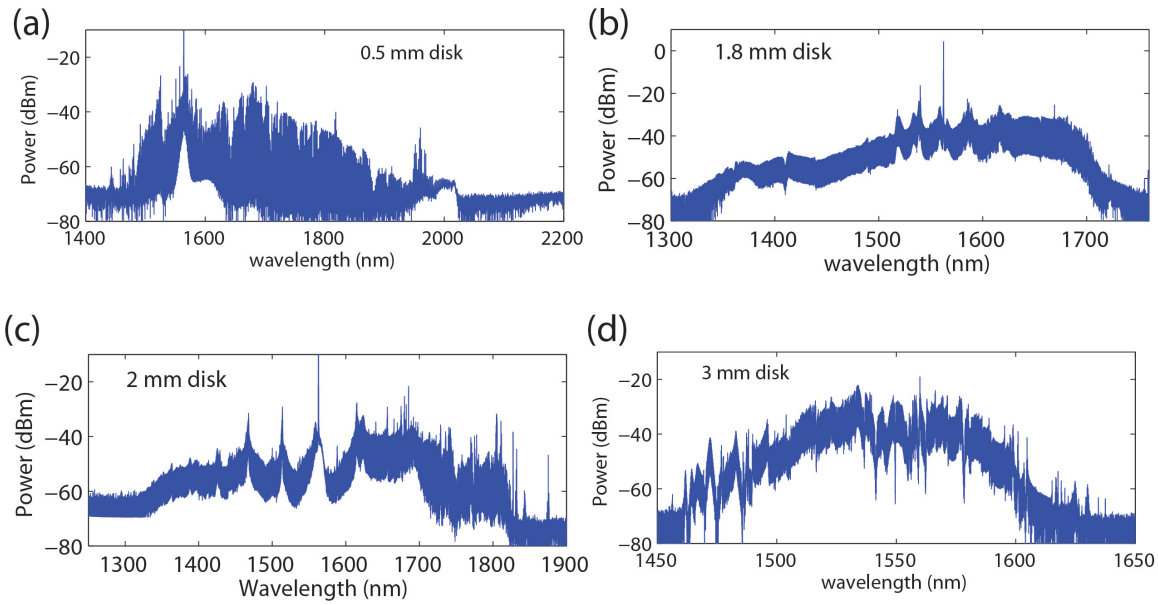

Figure 3.7: **Broadband microcomb spectra (22–132 GHz spacings)** (a) A 132 GHz microcomb spectrum with pump power 100 mW from a 0.5 mm disk is shown. The spectrum extends towards the longer wavelength because the zero-dispersion wavelength is above 1550 nm, due to the strong geometric dispersion by tight geometric confinement at smaller diameters. (b) A 37 GHz microcomb spectrum with coupled pump power 180 mW from a 1.8 mm disk. (c) A 33 GHz microcomb spectrum with coupled pump power 200 mW from a 2 mm disk. (d) A 22 GHz microcomb spectrum with coupled pump power 20 mW from a 3 mm disk.

filter (e.g., using a fiber-bragg-grating filter) can be used to suppress the pump laser by ∼40–50 dB, therefore improving the optical detection efficiency of comb lines. Figure 3.8 shows the difference in comb spectra detection with the pump line unsuppressed (3.8a) and suppressed by FBG filter (3.8b). An improvement of 16 dB in the optical signal-to-noise ratio (OSNR) is obtained by suppressing the strong CW pump line.

The microcombs demonstrated above are in the range of 20–200 GHz range. On the other hand, it is also interesting to access even smaller repetition rates down to a few GHz. The Ti:Sapphire comb can operate up to a few GHz typically (a 10 GHz Ti:Sa comb was demonstrated based on a 30-mm-long ring laser cavity very recently [37]). We have demonstrated microcomb operation below 10 GHz, therefore bridging the repetition rate gap between conventional combs (by mode-locked lasers) and microcombs (see figure 4 in [6]). Figure 3.9 shows the microcomb spectra with 2.6 GHz rep rate (a) and 6.8 GHz rep rate (b), from 25 and 9.6 mm disk resonators, respectively. In comparison, the lowest rep rate demonstrated from other types of microcombs was 9.9 GHz from a bulk CaF_2 resonator [56]. Indeed, the 2.6 GHz microcomb demonstrated here is a record value of microcomb rep rate for any kinds of resonator platform.

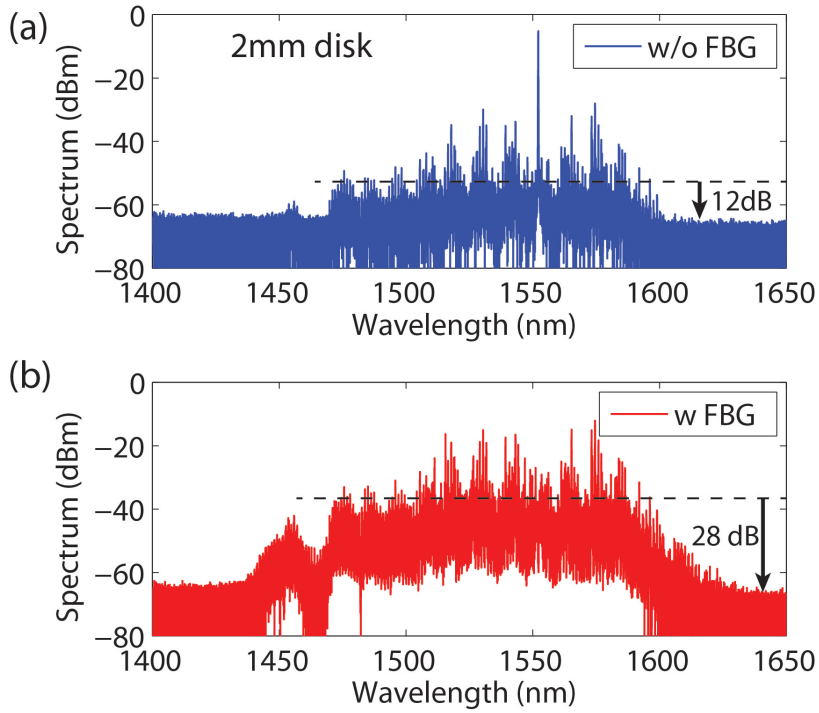

Figure 3.8: **Comparision of comb spectra detection w/wo FBG filter** (a) A 33 GHz microcomb spectrum from a 2 mm disk, with pump unsuppressed. The optical signal-to-noise ratio (OSNR) in the optical spectrum is 12 dB, as illustrated by the dashed black lines. The pump laser is attenuated prior to the OSA. Note that reduce the attenuation of the pump laser will also rise the noise floor of the instrument at the same time. (b) The detected comb spectrum for the same microcomb as in (a), however with the CW pump line suppressed by a FBG filter. The OSNR is increased by 16 dB.

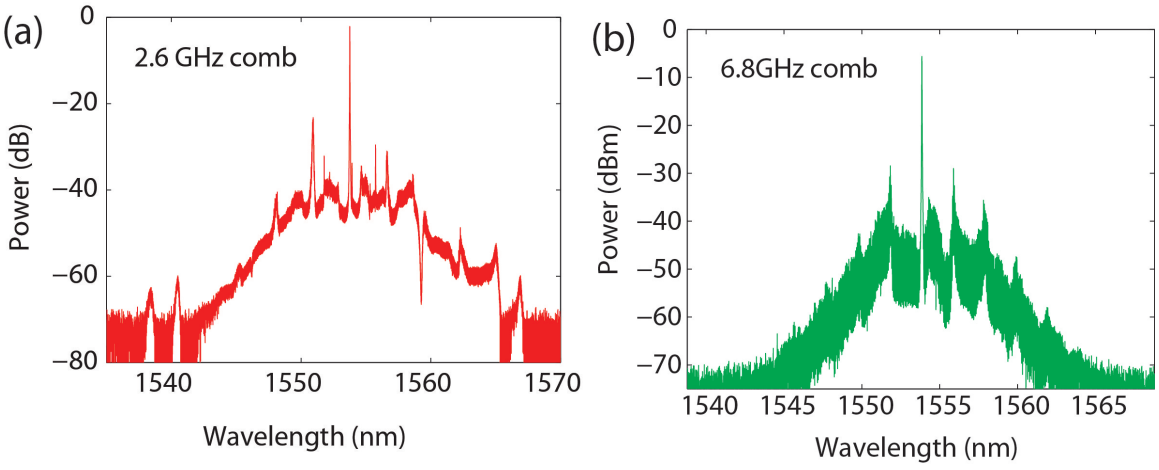

Figure 3.9: **Microcomb spectra with 2.6 and 6.8 GHz line spacings.** (a) A 2.6 GHz comb spectrum from a 25 mm disk. (b) A 6.8 GHz comb spectrum from a 9.6 mm disk. These combs are the smallest repetition rate demonstrated so far for any microresonated-based frequency combs.

3.6 Implication for Octave-spanning Microcomb with Microwave (≤40 GHz) Line Spacing

We have demonstrated broadband microcomb generation in section 3.5, accessing the important region of microwave-rate line spacings so far. Half an octave span (62 THz) for 33 GHz line spacing and 3/4 octave span (106 THz) for 66 GHz line spacing are demonstrated using 2 mm and 1 mm disks, respectively. Thus these results pave the way toward a fully octave-spanning comb using UHQ disk resonators.

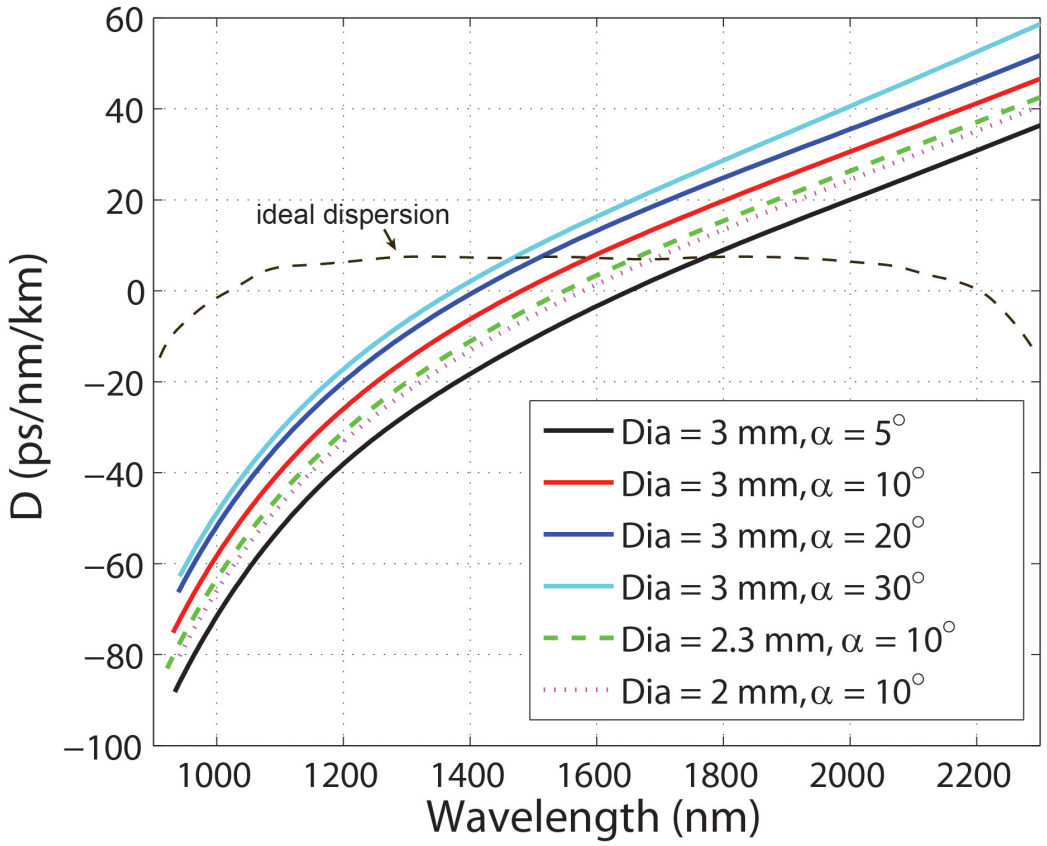

Figure 3.10: **Dispersion of disk resonators with different diameter and angles.** The dispersion parameter, $D \equiv \frac{d}{d\lambda}\left(\frac{1}{v_g}\right)$. The calculation is based on FEM-simulation of cavity eigenfrequencies for the fundamental mode. For 3 mm disks, the zero-dispersion wavelength (ZDW) can be shifted by around 300 nm by engineering the wedge angle, α, from 5° to 30°. The dispersion curve for the wedge resonators are not flat, i.e., containing a certain amount of third-order dispersion. Thus D becomes too much anomalous toward the infrared wavelength, and normal dispersion toward the visible wavelength, therefore limiting the bandwidth of microcomb. The gray dashed curve is an ideal cavity dispersion for broadband generation of octave-spanning microcombs with microwave (≤40 GHz) line spacing.

The current bandwidth of the microcomb generated by disk resonators are limited by the cavity

dispersion. Figure 3.10 shows a plot the dispersion parameter, $D \equiv \frac{d}{d\lambda}\left(\frac{1}{v_g}\right)$, for various wedge angles and diameters. The cavity dispersion can be engineered by changing the thickness and wedge angle, α. Figure 3.10 shows that the zero-dispersion wavelength (ZDW) can be shifted by 300 nm by changing α from 5° to 30°. This allows us to engineer the ZDW around 1550 nm (pump laser wavelength) for different resonators sizes. However, single wedge resonator contains a certain mount of higher-order dispersion (e.g., third-order dispersion, TOD), a signature resulting from the uncompensated material dispersion of silica. This produces too high anomalous dispersion toward the infrared region, and normal dispersion toward the visible region, as illustrated in figure 3.10. This kind of dispersion curve prohibits the growth of the comb bandwidth in both directions. (In simple terms, four-wave-mixing is a phase-matched process. Too-high-anomalous dispersion requires more nonlinear phase shift from the pump laser and the generated comb lines, while normal dispersion is in general not preferable for phase matching [58]). Thus such characteristic of the dispersion curve in current devices limits the ultimate comb bandwidth. An example of an ideal dispersion curve (grey dashed line) is plotted in figure 3.10, having a wide bandwidth of low second-order dispersion (D), and low third-order dispersion (flatness). We are currently progressing toward such kind of dispersion curves by novel engineering of the resonator structure to compensate the characteristic material GDD and TOD.

3.7 RF Noise of the Microcomb

One important characteristic of microcomb is the equidistance of the comb line spacings. A mean equidistance level on the order of mHz at 1 second is measured for a microcomb with large line spacing of 7 nm from a 75-μm-diameter toroid microcavity [38]. In that experiment, because the line spacing beat note is too large to be detected using a photodetector, an external fiber comb is used for multi-heterodyne beat note detection and frequency counting [38]. Here, because of the microwave line spacings of the microcombs, in principle a single narrow RF beat note from a fully populated microcomb is sufficient to verify the equidistance of the line spacings. However, in our experiments, the demodulated microcomb RF beat note shows very rich and involving dynamics. The RF spectrum could show a single RF tone, multiple RF tones, RF linewidth broadening, and broad RF beat notes. Similar effects are also reported in a fused-quartz microcomb system with around 36 GHz line spacing [47]. In addition, complementary studies in the time domain also shows that the microcomb lines exhibit either highly or partially coherent phase relations [45].

Figure 3.11 shows the typical dynamics of comb RF noise and optical spectrum progressing with the decrease of the pump detuning. The microcomb is generated by a 3 mm disk resonator with 21.9 GHz FSR. It starts with cascaded optical parametric oscillation lines in state I, with no RF beat note observed at cavity FSR. In state II, more comb lines are generated around/between the

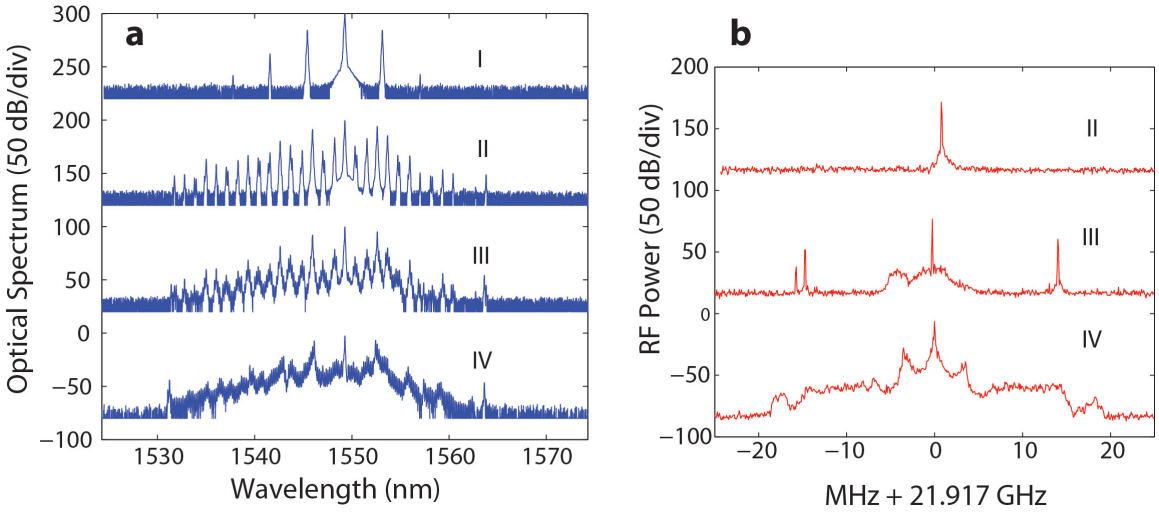

Figure 3.11: **Evolution of the microcomb RF noise.** A 21.9 GHz microcomb is generated from a 3 mm disk resonator. While tuning the pump laser close to resonance, a progression of the microcomb optical (a) and RF (b) spectra is observed. I: the first oscillation lines are located multiple FSRs away from the pump, and no RF beat note at 21.9 GHz is observed. II: more comb lines are generated around the first oscillation lines, forming a cluster like optical spectrum. The RF spectra is a single narrow beat note at cavity FSR. III: The different clusters of comb lines are connected. Multiple RF tones are observed. IV: A fully populated comb spectrum is generated. The corresponding RF noise is a broad beat note.

first oscillation lines, forming cluster like regions in the optical spectrum. The corresponding RF spectrum is a single narrow beat. As the pump detuning decreases, the comb line clusters begin to grow and merge together, shown in state III. Multiple RF tones and RF skirt noise are observed. Finally, when the comb lines are completely populated and smooth in the optical domain in state IV, the RF spectrum shows a broad beat note with no features of resolving a narrow RF tone.

One important aspect of the linewidth broadening of the RF beat note progressing with the merging of the comb clusters is to check whether the linewidth broadening is coming from different wavelength region of the comb lines or not. One speculation was that the different spectral regions of the comb lines contribute to RF beat notes with slightly different frequencies, due to different local cavity dispersions. However, we filter the microcomb with a tunable bandpass filter (BPF) with 1 nm bandwidth and detect the RF beats in different regions. Our results show that different wavelength regions have the same broad RF beats as the total RF beat note. The BPF in the experiment contains about 6 comb lines.

In another experiment, in order to examine the phase noise of individual comb line, we also carried out heterodyne mixing of the comb lines with a tunable external-cavity diode laser (ECDL). The microcomb is generated from a 3 mm disk resonator with 21.986 GHz line spacing, and is shown in figure 3.12a. The pump laser (a narrow-linewidth fiber laser) and the ECDL laser line are both present in the optical spectrum. A zoom-in view of the ECDL laser line with the comb lines is given

in figure 3.12d. The demodulated RF beat is a broad spectrum with around 10 MHz lindwidth (3.12b). Interestingly, the baseband comb amplitude noise, given in figure 3.12c, has a very similar shape with the RF noise. The beat notes between individual comb line and the ECDL are given in figures 3.12e-h, at wavelength 1522, 1540, 1560 and 1575 nm, respectively. It can be seen that even individual comb line features significant amount of linewidth broadening and increase in its phase noise, at all the wavelength regions.

The involving dynamics of microcomb RF noise described above is systematically studied and explained in [54]. According to [54], the microcomb formation first goes through degenerate FWM to generate primary sidebands (spaced by Δ), located at multiple cavity modes from the pump mode. The secondary comb lines are generated around the primary lines and form subcombs (cluster-like comb lines described above) with a native spacing δ ($\delta/2\pi \approx$ FSR). The spacing Δ is not in general an integer multiple of δ. Thus the different subcombs have different offset frequencies. (The subcomb offset frequency, ξ, is defined as $\Delta \mod \delta$). Nevertheless, the individual comb spacings in different subcombs residing at different spectral regions are equal, resulting in a single narrow overall RF beat when the subcombs are isolated. Therefore, the proper labeling of the microcomb line frequencies is not exactly the same as the conventional comb lines. In microcombs, the optical spectrum of the whole microcombs contains multiple equidistant subcombs of index i, composed of lines of index n (relative to the pump mode), at optical frequencies $\omega_n^{(i)}$ separated by the same spacing δ [54]:

$$\omega_n^{(i)} = \omega_p + \xi_i + n \times \delta, n = 0, \pm 1, \pm 2, ... \tag{3.8}$$

The merge of two subcombs, with index i and j, in the optical domain would give rise to offset beats in the RF domain, located at$|\xi_i - \xi_j|$ from the central native-line-spacing beat δ. This implied that multiple comb tooth reside in the same cavity mode, spaced by $|\xi_i - \xi_j|$. Thus it also results in a baseband beat of $|\xi_i - \xi_j|$ from DC. Finally, when many subcombs merge together to form a fully populated smooth optical spectrum, the different offset beats also merge together to form a significantly broadened RF beat in the microwave domain and a broad baseband noise close to DC.

3.8 RF Phase Lock of Microcombs

As described in section 3.7, lower repetition rate combs are prone to unstable microwave beats. This happens because the comb oscillation initiates on a nonnative line spacing and grows into a set of secondary combs, each that can feature a distinct offset frequency. In the present system, the ability to fabricate a wide range of FSRs has been used to search for cases in which the resulting dispersion in offset frequencies is low enough to allow pump-detuning-alignment of the underlying subcomb offset frequencies. We have observed alignment and measured for the first time a locking of the

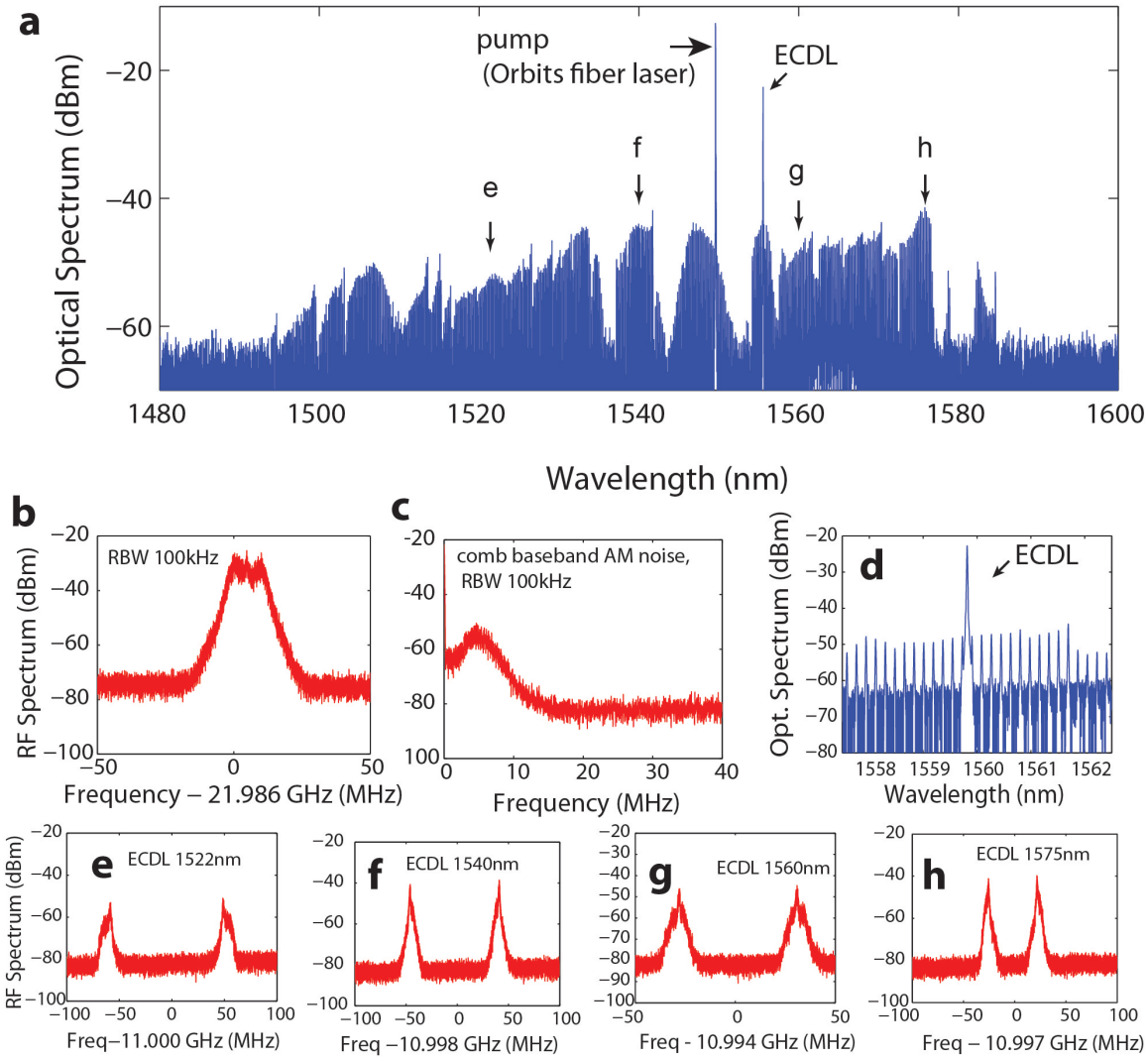

Figure 3.12: **Study of comb phase noise by heterodyne mixing with a separate laser.** A 21.986 GHz microcomb is generated from a 3 mm disk resonator. The comb phase noise is studied by heterodyne mixing different comb teeth with a separate tunable ECDL (external-cavity diode laser). (a), microcomb optical spectrum, the pump laser is a narrow linewidth fiber laser (Orbits lightwave, Inc.), and the mixing tunable ECDL laser is also shown. (b) Demodulated RF spectrum of the microcomb shows a broad beat note. (c), Comb baseband amplitude noise, detected by a monitor photodetector with 125 MHz bandwidth, shows a similar shape with the RF beat note in (b). (d), zoom-in view of the mixing tunable ECDL with microcomb lines. (e) Beating notes are detected from the heterodyne mixing of the ECDL and the closest two neigbouring comb lines. The ECDL is tuned such that it is located almost at the center of the two neighbouring comb lines. ECDL is set at 1522nm. (f) ECDL is set at 1540nm. (g). ECLD is set at 1560 nm. (h) ECDL is set at 1575 nm.

phase across a broad span of comb lines. The effect now described has been observed for a broad range of repetition rates spanning 4 GHz to 26 GHz.

Figure 3.13 shows the comb generation and evolution in a 21.953 GHz comb as the pump detuning is gradually decreased. Here the pump laser is a CW fiber laser with effective linewidth of ∼1kHz. The optical spectrum and corresponding RF spectrum (low and higher resolution) are presented at each detuning. The launched pump power in the fiber is 11 mW when the laser is off resonance. For state I, the coupled pump power is 2.8 mW, and both the primary combs (2.5 nm spacing) and secondary combs (subcombs with native spacing 22 GHz) are visible in the optical spectrum. In this state, only one RF tone is observed. From state II to state V, more power is coupled into the cavity and the subcombs grow and begin to overlap, resulting in additional beat notes. Also, we observe that the beats tend to merge toward the native-line beat note with continued tuning of the pump toward the optical resonance. For state VI, the multiple beats merge to create a broad pedestal region around the central beat note. For state VII, the broad pedestal snaps into a single sharp tone with very narrow linewidth and low phase noise.

In light of the discussion in [54] we interpret these results as controlled tuning of the underlying subcomb offset frequencies into a state (state VII) of degeneracy. Moreover, the "snapping" effect and ability to maintain this state over long periods of time suggest that some kind of locking phenomena is at work that self-injection-locks the subcombs into degeneracy once a certain locking range is attained through pump tuning. As further evidence of the phase locking, figure 3.14 shows a sequence of phase noise spectra taken for the states given in figure 3.13. For the phase lock state VII, the phase noise is about 20 - 30 dB lower than the non-phase-locked states. There are approximately 80 comb lines that are phase locked. It is worth noting the very low phase noise level (-113 dBc/Hz at 10 kHz offset for 22 GHz carrier) is not only a record low phase noise state for a microcomb, but also a level in line with high performance microwave oscillators when operated open loop.

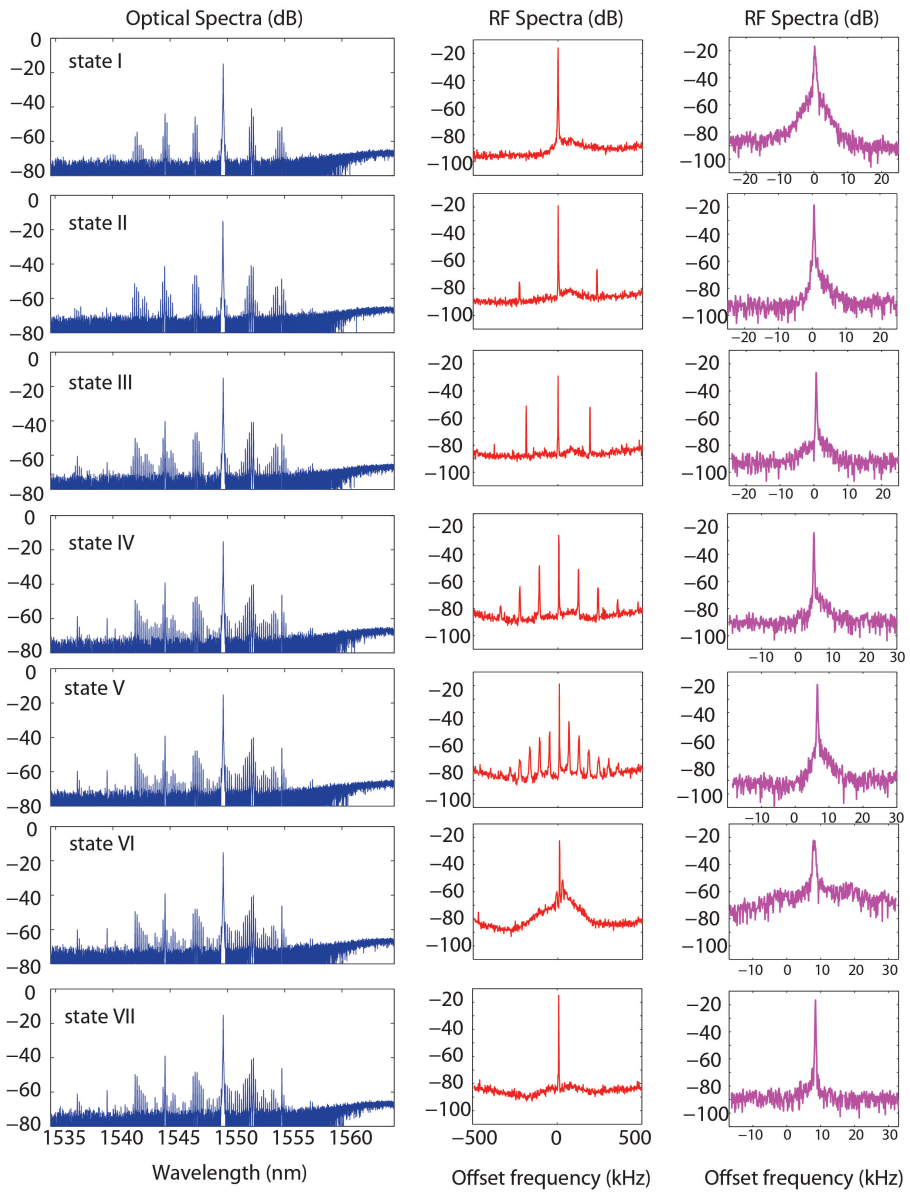

Figure 3.13: **RF Phase lock dynamics.** Recorded optical spectra (left column) and RF spectra (middle and right columns) for different amounts of pump-laser detuning. Detuning is gradually decreased from state I to VII and simultaneously increases the coupled pumping power. The merging beat note spectrum evident in each state of the microcomb is a result of tuning underlying subcomb offset frequencies into coincidence. In State VII there is a sudden collapse of the spectrum into a single, narrow beat note. The frequency scale for the RF spectra is set with the zero at 21.953 GHz. The span and resolution setting are 1 MHz and 100 Hz for the middle column spectra, and are 50 kHz and 100 Hz for the right column spectra.

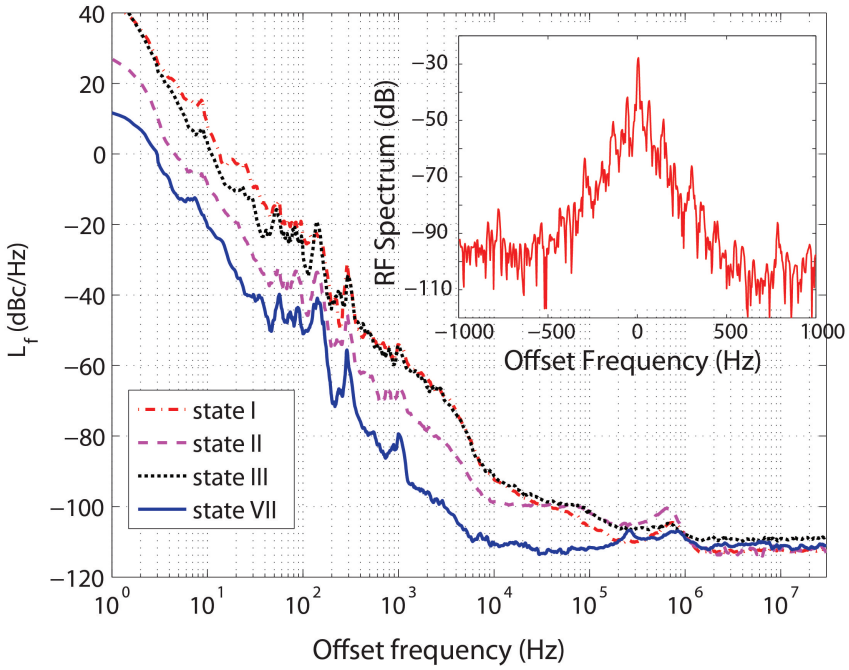

Figure 3.14: **Phase noise and RF spectrum at RF phase lock.** Main panel: Single sideband phase noise of the comb beat note (carrier at 21.953 GHz) for four of the states presented in figure 3.13. The phase lock state (state VII) shows a very low phase noise of -113 dBc/Hz at 10 kHz offset frequency. Inset: Spectrum of the RF beat note when the microcomb is in the phase lock state (state VII). Span is set to 2000 Hz and the resolution bandwidth is 10 Hz.

Chapter 4

Pulse Generation and Phase Noise Transfer of Microcomb

4.1 Introduction

The generation of laser pulses with duration on the femtosecond timescale has had significant impact in the fields of physics, chemistry, biology, and engineering. Examples include femtochemistry [59], the generation of high-harmonics and phase-controlled pulses [60], multiphoton microscopy [61], and precision spectroscopy and frequency metrology [26, 29]. Most commonly, femtosecond-duration pulses are generated via the phase-locking of numerous frequency modes that oscillate simultaneously in a laser having broad bandwidth gain and dispersion management. In this case, the Fourier superposition of a comb of equally spaced frequency modes with constant relative phase produces a repetitive train of ultrashort pulses, the duration of which is given by the inverse of the frequency bandwidth [62]. In laser systems, both active and passive techniques have been employed to fix the relative phases of the modes; however, passive phase-locking via the ultrafast Kerr nonlinearity has produced the shortest optical pulses with duration of just a few optical cycles [63, 64].

While the generation of pulses from the phase-locked comb of a laser oscillator has nearly a 50-year history [65], a recent development is that an equally spaced comb of optical frequencies can also be produced from parametric laser oscillation in a dielectric microresonator [38]. In principle, if the optical modes from such a parametric microcomb oscillator could be phase-locked, these devices would also produce a train of ultrashort pulses. The properties of microresonator combs are significantly different from those of conventional lasers in several aspects that require new physical understanding and could lead to unique advantages for some applications. Importantly, the characteristic size of these microresonators is on the millimeter or submillimeter scale, and the construction is monolithic and compatible with planar lithographic fabrication techniques. These factors could lead to inexpensive and robust devices producing ultrashort pulses at gigahertz rates. Additionally, in contrast to population inversion and stimulated emission in a laser, microresonator combs arise

from parametric gain via nonlinear four-wave mixing with a single CW pump. This provides advantages of broad bandwidth tunability that is not limited by specific atomic or molecular transitions.

It has been demonstrated that microresonator comb lines can have phase locked, coherent relative phase relations to enable ultrashort pulse generation by external line-by-line shaping of phase and intensity [45, 47]. Also, RF phase locking of microcomb beat note from multiple-RF tones to a single low-noise tone by pump laser detuning alignment is reported [52] (discussed in section 3.8). Theoretical work has predicted the existence of different regimes of mode-locked operation that could result in ultrashort pulses [66, 67]; however, only very recently have measurements reported evidence of soliton generation directly from a microresonator parametric oscillator [68, 69]. In this chapter (sections 4.2–4.4), we report on a phase-locked microresonator comb that produces repetitive bursts of 400 fs pulses without external line-by-line pulse shaping. Behavior consistent with mode-locking is supported by a single narrow RF beat signal at 22 GHz and high-contrast frequency-resolved optical gating (FROG) measurements. Moreover, under different pump detunings, we observe an incoherent alternative microcomb state, characterized by a broad RF beat note and a low-contrast FROG measurement with a constant background.

In the second half of the this chapter (sections 4.5–4.8), we investigated the characteristics of the microcomb RF phase noise. We showed that the frequency fluctuations of the pump laser relative to the resonator is greatly reduced by thermal lock. An explicit formula of the thermal reduction gain of laser frequency noise is derived. We measured the transfer function of the laser phase noise to the microcomb RF phase noise, and found that the thermo-locked laser frequency noise is the major noise source of the comb phase noise. We further demonstrated a shot-noise-limited microcomb phase noise (-156 dBc/Hz for offsets greater than 10 MHz) for the first time, a significant improvement over the white noise floor of the precedent microcombs. Finally, stabilization of the microcomb repetition rate (22 GHz) is realized by phase lock loop control using a microwave source and acousto-optic modulator.

4.2 Temporal Pulse Formation and Measurement Setup

It is important to examine the spectral phase relations of the microcomb lines and its effect on the temporal pulse formation and temporal mode locking. In figure 4.1, we calculated the temporal pulse structures for a sparsely populated microcomb (left column) and a fully populated microcomb (right column), assuming flat spectral phase or random-distributed spectral phase relations. The line spacing of the comb lines are 22 GHz from a 3 mm disk resonator, with cavity round trip time 45 ps. For the sparse microcomb, the subcombs are marginally connected, as shown in figure 4.1a. Its temporal structure within one cavity round trip time shows a well-isolated wavepacket with high contrast and nearly zero background level. The wavepacket contains a periodically spaced

ultrashort pulses, the time interval of which is equal to the inverse of the primary subcomb spacings in figure 4.1a. However, for the case of random-distributed phase relations (spectral phase plotted as red circles in figure 4.1b), the temporal formation and its autocorrelation (AC) is a continuous multipeak structure with low contrast, as shown in figure 4.1d. Similarly, for the fully populated smooth microcomb with a flat phase, the temporal domain collapses into a single ultrashort pulse within one cavity round trip time, as shown in figure 4.1g. The temporal domain for the spectral random phase relation of comb lines (plotted in figue 4.1f) is a noiselike continuous structure. Significantly, the autocorrelation for the noiselike temporal structure contains a featured coherent spike at zero delay and 50% background level. From this simulation, it can been seen that a high-contrast, isolated pulse measurement from microcomb is a clear indication of a regular or constant phase relations between the comb lines. Furthermore, depending the "randomness" of the spectral line phases, the background level in the autocorrelations would change from zero to ∼50%.

The experiment layout we use to investigate the temporal and RF characteristics of the microcomb is given in figure 4.2b. The microresonator is a silica-on-silicon planar disk resonator having diameter of 3 mm [7]. These disk resonators have been used to demonstrate microcomb operation with low-threshold (1mW) and microwave to millimeter-wave repetition rates from 2.6 to 220 GHz [52]. A tunable narrow-linewidth CW fiber laser (short-term linewidth of ∼1 kHz) that is amplified by an Erbium-doped fiber amplifier (EDFA) is evanescently coupled into the resonator with a tapered fiber [13, 14]. For longer-term reliable operation, the taper is placed in physical contact with the microresonator. The resonator transmission with microcomb output is split into several channels. One channel goes to a monitor photodetector (m-PD A, bandwidth 125MHz) for transmission monitoring, and another channel goes through a Fiber-Bragg-Grating (FBG) notch filter to suppress the CW pump. The microcomb with CW pump suppressed is further split into another four channels, which are used for microcomb power monitoring (m-PD B with 125 MHz bandwidth), RF beat note detection (f-PD with bandwidth 50 GHz), optical spectrum monitoring, and temporal pulse characterization with scanning frequency-resolved optical gating (FROG) [70]. For the FROG measurement, the microcomb (with CW pump suppressed) is amplified first by another EDFA to average power of about 200 mW. Using these combinational detection schemes, both the RF and temporal dynamics of a microcomb can be fully characterized.

4.3 Subpicosecond Pulses from a Microcomb

We pump a high Q resonance (Q = 73 million) of a 3 mm disk resonator (FSR ≈ 21.95 GHz) with off-resonance power of 70 mW. The full progression of the microcomb spectra with the decrease of the pump detuning is shown in figure 4.3. It starts with the first-oscillation OPO lines in progression I, and cascades to higher order OPO lines in II. Subcombs around the first OPO lines are formed in

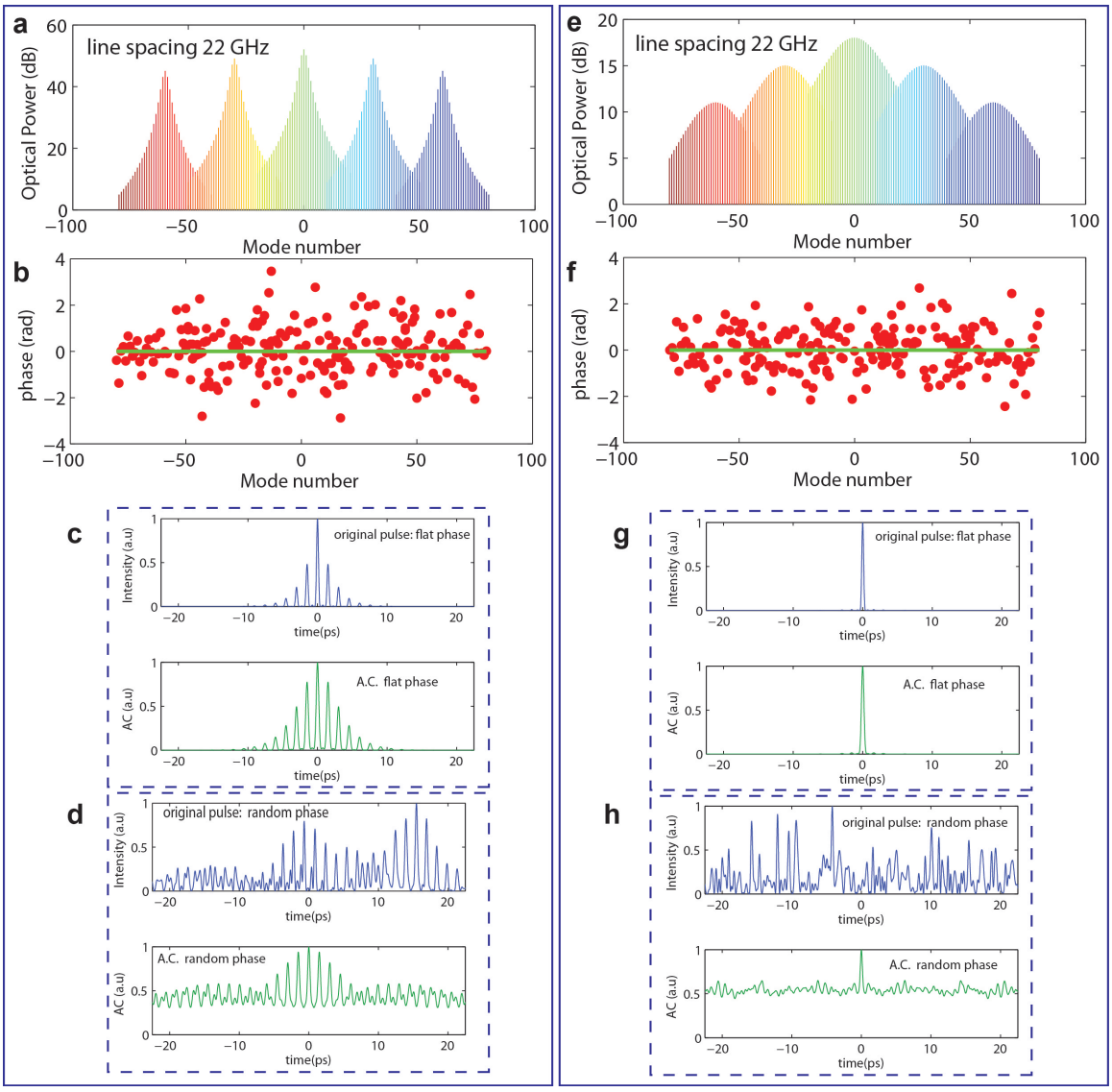

Figure 4.1: **Illustration of temporal pulse formation.** (a) Optical spectrum of a sparse microcomb with subcombs marginally connected. (b) Spectral phase of each comb line for random phase relations (red circles) and flat phase relations (green line). (c) Temporal pulse formation (upper panel: original pulse; lower panel: autocorrelation) is simulated from the spectral intensity in (a) and flat phase relations in (b). Both the temporal pulse and its autocorrelation within one cavity round trip show an isolated pulse wavepacket with high contrast, and nearly zero background. (d) Temporal pulse and its AC are shown for the random phase relations of the sparse comb lines given in (b). (e)-(h): The similar temporal pulse formation is simulated for a fully populated smooth microcomb. The multipeak wavepacket in (c) collapses into a single ultrashort pulse in (g) for the case of flat phase relations. For the case of random phase relations, the temporal domain shows a noiselike structure and an AC with a coherent spike at zero delay and about 50% background.

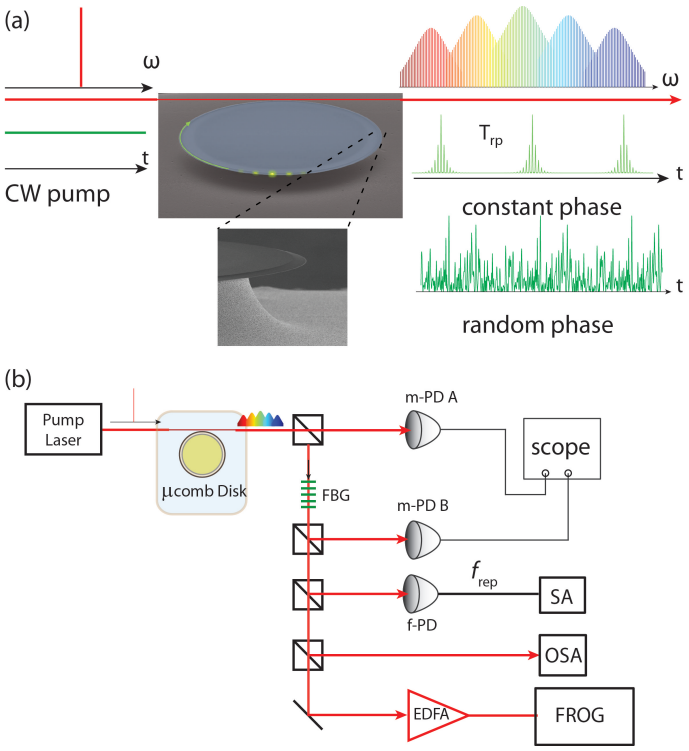

Figure 4.2: **Experimental setup.** (a) Mode locking of a microcomb producing short pulses from a monolithic resonator on a silicon chip. (b) Experimental layout. m-PD: monitor photodetector; FBG: fiber-Bragg-grating filter; f-PD: fast photodetector; SA: rf spectrum analyzer; OSA: optical spectrum analyzer; FROG: frequency-resolved optical gating.

III (with twice-FSR line spacing). More comb lines are generated between the first OPO lines at IV. Clusters of subcombs with native mode spacing (fundamental FSR) is formed in V. At state V, the microcomb features a single narrow RF beat note at 21.948 GHz, shown in figure 4.4a. The temporal field is characterized with a background-free second-harmonic FROG measurement (figure 4.4b upper panel). We have also recorded FROG spectrograms over longer delays to verify that a repetitive pulse pattern is detected at a period of the cavity round-trip time (∼45 ps). Significantly, the FROG spectrogram shows a high-contrast, isolated wavepacket. Furthermore, the pulse wavepacket has a highly modulated temporal profile, with multiple ultrashort temporal pulses separated by 1.6 ps, which corresponds to the modulation in the comb spectrum with primary spacing of 5.0 nm. The FROG spectrogram in figure 4.4b is used to numerically retrieve the complex optical field [70]. The retrieved FROG spectrogram is shown in figure 4.4b (lower panel), and it differs from the measured spectrogram with an error of 5.5%. Figure 4.4c shows the retrieved temporal pulse intensity and phase. The full-width-half-maximum (FWHM) of each periodic pulse within the wavepacket is 500 fs. This is in good agreement with the FWHM of the autocorrelation (600fs), obtained by integration of the FROG trace. The retrieved spectral intensity is plotted in figure 4.4d. The spectral envelope from the FROG measurement (resolution of $\leq$2 nm) is in good agreement with the independent measurement of the optical spectrum (blue curve), which was acquired at a much higher resolution of 50 pm.

While this mode of pulse generation is sensitive to detuning and the taper coupling, we have observed similar behavior over many days under repeated resetting of the coupling and the detuning. In fact, using a second 3 mm disk resonator, we increased the coupled pump power to 135 mW and obtained the quasi-continuous microcomb spectrum shown in figure 4.5a. In this state, the RF beat note is a similar stable single narrow tone as in figure 4.5b, which implies that the comb elements are separated by the same repetition rate with no additional frequency offset [54]. The measured and retrieved FROG spectrograms are given in figure 4.5c, and the retrieved temporal pulse structure is shown in figure 4.5d. This temporal characterization (FROG spectrogram and retrieval) shows a high-contrast, regular-structured isolated pulsed wavepacket with near zero-background. Moreover, the FWHM of each pulse under the wavepacket in this case is 400 fs, which is consistent with the FWHM of the AC by integration from the FROG trace (540 fs).

Based on the model put forth in [54], a single narrow RF tone for a quasi-continuous microcomb (figure 4.5a) means that the different subcombs have the same offset frequencies [54], and the comb lines spacings are equidistant. A high-contrast, isolated pulse measurement from the microcomb implies that the phase relations of the different comb lines are fixed and regular distributed. (Both of these aspects are consistent with mode-locking behavior.)

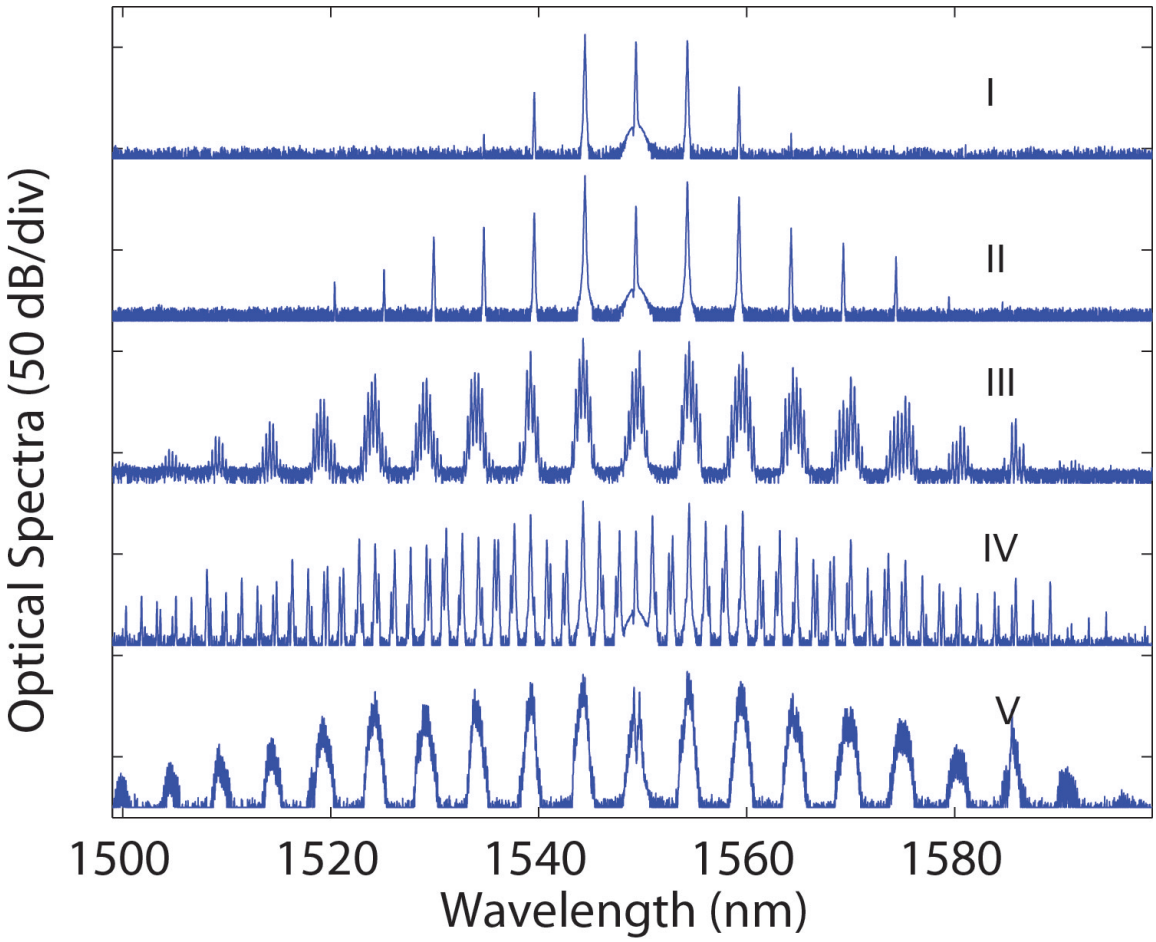

Figure 4.3: **Tuning of a microcomb to a mode locked state generating short pulses.** An narrow linewidth fiber laser (Orbits Lightwave) with off-resonance power 70 mW is gradually tuned into a high Q resonance (Q = 73 million) of a 3 mm disk resonator. A progression of the microcomb optical spectra with the decrease of the pump detuning is shown. It starts with the first-oscillation OPO lines in progression I, and cascades to higher order OPO lines in II. Subcombs around the first OPO lines are formed in III (with twice-FSR line spacing). More comb lines are generated between the first OPO lines at IV. Clusters of subcombs with native mode spacing (fundamental FSR) is formed in V. At state V, the microcomb features a single narrow RF beat note and a high-contrast, isolated pulse measurement, shown in figure 4.4.

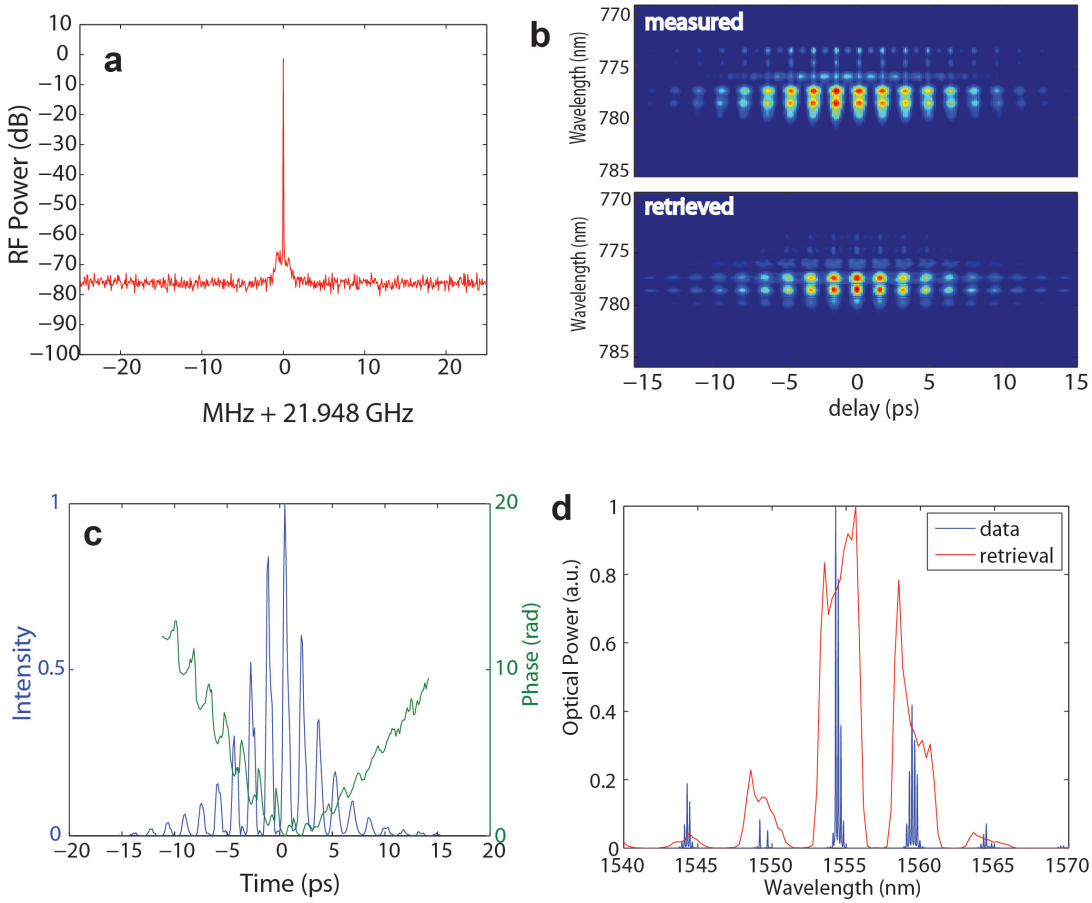

Figure 4.4: **Subpicosecond pulses from a sparse microcomb.** (a) RF spectrum of the microcomb in state V of figure 4.3 showing a single narrow beat (span 50 MHz, RBW 3kHz). (b) upper: measured FROG spectrogram of the microcomb. lower: reconstructed FROG spectrum. Delay span is 30.5 ps. The cavity round trip time (T_{rp}) is 45 ps. A even larger delay scan was taken to confirm that another repetitive FROG patterns the same as this spectrogram was measured T_{rp} away. The FROG trace shows a highly modulated, isolated wavepacket with high contrast. (c) Retrieved temporal pulse intensity and phase showing bursts of subpicosecond pulses. Each pulse under the wavepacket has duration of 500 fs. (d) Retrieved comb spectral intensity (red) together with measured comb spectrum by OSA after EDFA (blue).

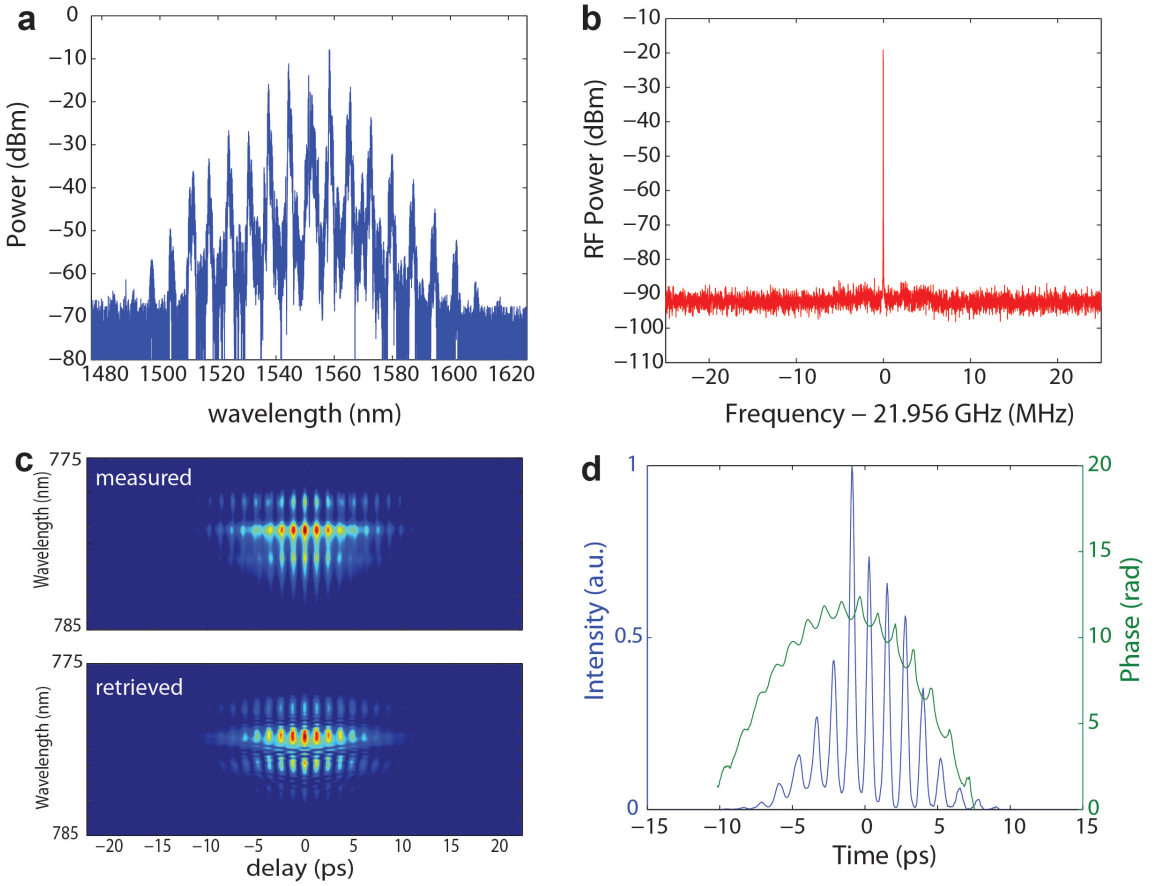

Figure 4.5: **Subpicosecond pulses from a quasi-continuous microcomb.** (a) Optical spectrum of a quasi-continuous microcomb. (b) RF spectrum of the microcomb showing a single narrow RF beat note. Span 50 MHz, RBW 1kHz. (c) upper: measured FROG spectrogram of the microcomb. lower: reconstructed FROG spectrogram. Delay span is equal to the cavity round trip time (∼45 ps). (d) Retrieved temporal pulse intensity and phase showing bursts of subpicosecond pulses. Each pulse under the wavepacket has duration of 400 fs.

4.4 Incoherent Microcomb Characterized by FROG and RF Beat

For a comparative study, we show in figure 4.6 a typical operation condition of the microcomb, accompanied by a FROG spectrogram with a constant background, and a very broad RF beat note. These data are obtained within the same cavity mode as figure 4.5, but with less coupled pump power of ∼100 mW (by a larger detuning). The optical spectrum of this microcomb, as shown in figure 4.6a, is a fully populated continuous spectrum. The inset of figure 4.6a shows a broad RF beat note with a flat top. We note that the characteristics of the optical and RF spectra of this microcomb have similarities to the description of the chaotic region of microcomb generation [67]. The broad RF beat note in this region implies that the relative phase and/or amplitudes of the microcomb lines are rapidly fluctuating in time. This is also supported by the temporal autocorrelation measurement. Figure 4.6b shows the FROG trace with delay scan of one cavity round trip (∼45 ps, upper panel), and the autocorrelation (AC) trace obtained from integration of the FROG spectrum at each delay point (lower panel). A constant background with a coherent spike at zero delay is observed in the AC and FROG. Moreover, the background level is 40%, which is consistent with the case of a noiselike field with Gaussian-distributed random phases [45, 62]. These observations are in clear contrast to the mode locking behavior in the temporal and RF domain described in section 4.3.

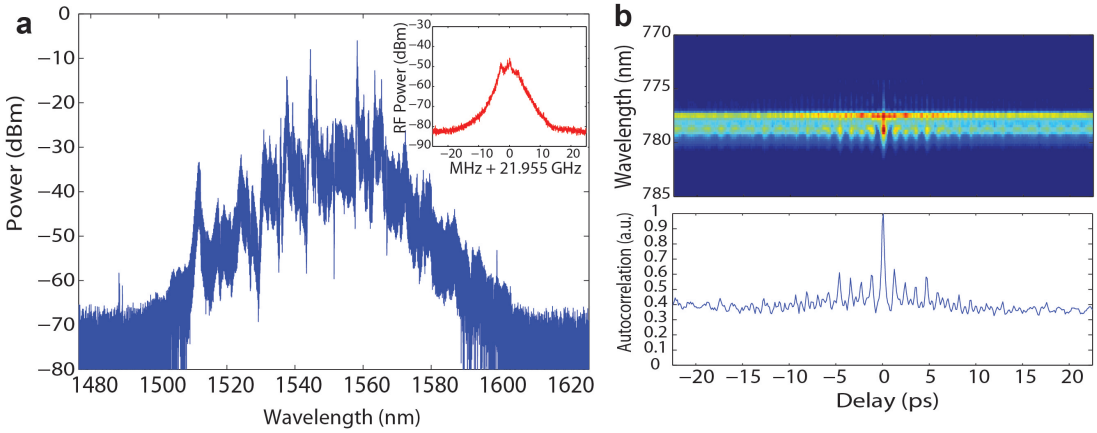

Figure 4.6: **Incoherent microcomb characterized by FROG and RF beat.** (a) Optical spectrum of a fully populated microcomb. Inset: Broad RF beat note of the microcomb, span 50 MHz, RBW 50 kHz. (b) Upper: FROG spectrogram of the microcomb temporal structure; Lower: autocorrelation (AC) of the temporal structure of the microcomb. Both the FROG and AC shows a constant background (40%) and a coherent spike at zero delay.

In summary, we have observed phase-locked behavior of a microresonator frequency comb that produces stable and temporal output characterized by a single narrow RF beatr at 21.95 GHz and high-contrast, isolated temporal pulses with duration as short as 400 fs. Measurement of the system

dispersion, combined with SHG-FROG measurements imply that the observed pulse structure is characteristic of the field circulating in the resonator. Moreover, the temporal structure of this phase-locked state differs from recent experiments and predictions of isolated solitons [66, 68, 69]. In addition, we have observed an alternative incoherent microcomb state that is characterized by a broad RF beat note and a 40% constant autocorrelation background, under a different pump detuning. This state has similarities to chaotic dynamics recently described by Matsko [67].

4.5 Laser Frequency Noise Reduction Due to Cavity Thermal Lock

4.5.1 Thermal-induced Linewidth Broadening in Millimeter-sized Disk Resonators

Thermal nonlinear effects in microresonators have been studied previously [57, 71, 72], including thermal oscillation instability, thermal linewidth broadening, and wavelength hysteretic response. One important characteristic of the cavity dynamic thermal response is the "shark-fin"-like cavity lineshape (thermal triangle), when the input power of the laser is above certain threshold and the laser is scaned accross the cavity resonance [57]. In simple terms, the thermal triangle is due to the nonlinear cavity resonance shift as a result of the cavity heating (scan toward resonance) and cooling (scan away from resonance). Typically, the thermal-induced cavity resonance shift is inverse proportional to the cavity mode volume (heat capacity). Thus the millimeter-sized disk resonators show much less thermal broadening than μm-sized microtoroids. Figure 4.7a shows the measured thermal-broadened cavity lineshape of a 2 mm disk resonator (loaded linewidth 2.9 MHz) under a series of input power levels from 6 μW to 1 mW. The corresponding cavity resonance shift is plotted versus the input power in figure 4.7b.

4.5.2 Thermal Reduction Gain of Laser Frequency Noise

It has been known that microresonators can be passively locked to an external laser due to thermal self-stabilities [57]. This kind of passive lock of is also called "thermal lock." However, the exact formula of thermo lock, showing the linewidth reduction the laser, has not been derived. In this subsection, we start from coupled mode equations including the thermo-optic effects, and use perturbation approach to derive the exact form of laser frequency noise reduction due to cavity themal lock.

The coupled mode equations [73] describing the cavity mode amplitude including the thermo-

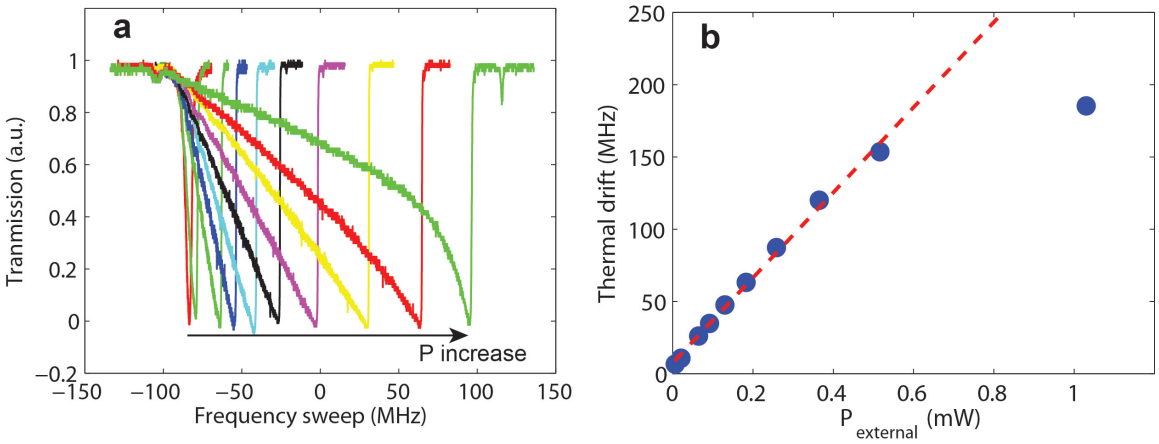

Figure 4.7: **Thermal-induced cavity nonlinear resonance shift.** (a) The thermal nonlinearity of the cavity (refractive index and thermal expansion) results in a dynamic cavity lineshape with a broadened shark-fin shape when the input power increases. The cavity diameter is 2 mm, and the loaded cavity linewidth is 2.9 MHz. The input power is increased from 6 μW to 1 mW. (b) Thermal-induced cavity resonance shift is plotted versus the external input power from 6 μW to 1 mW.

optic effects, and cavity temperature increase, ΔT, is given as

$$\dot{a} = -[i\Delta - ig_{th}\Delta T + \frac{\kappa}{2}]a + \sqrt{\kappa_{ex}}s; \tag{4.1}$$

$$\dot{\Delta T} = -\gamma_{th}\Delta T + \Gamma_{abs}|a|^2 c_{th}; \tag{4.2}$$

where a is the complex optical cavity field amplitude normalized such that $|a|^2$ is intracavity field energy, $|s|^2$ denotes the input optical power, $\Delta \equiv \omega_l - \omega_0$ is the bare laser detuning from the cold cavity resonance (ω_o), and κ is the cavity field energy decay rate. γ_{th} is the temperature decay rate, Γ_{abs} is the component of the optical energy dissipation due to material absorption, c_{th} is the thermal heat capacity of the cavity, and $g_{th} = -\frac{\mathrm{d}n}{\mathrm{d}T}\frac{\omega_o}{n_o}$ is the thermo-optic tuning coefficient.

Using the perturbation approach, we assume that the laser frequency fluctuation with a small parameter ϵ, causing the resonance detuning $\Delta = \Delta_0 + \epsilon\Delta_1(t)$. Then the optical mode amplitude and the cavity temperature increase can be expanded in terms of the small parameter ϵ (to the first order),

$$a = a_o + \epsilon a_1(t); \tag{4.3}$$

$$\Delta T = \Delta T_o + \epsilon \Delta T_1(t); \tag{4.4}$$

This yields the following set of coupled equations due to the zeroth order terms and the first order

terms,

$$0 = -\left[i\Delta_o - ig_{th}\Delta T_o + \frac{\kappa}{2}\right] a_o + \sqrt{\kappa_{ex}}s = -\left[i\Delta'_o + \frac{\kappa}{2}\right] a_o + \sqrt{\kappa_{ex}}s; \tag{4.5}$$

$$0 = -\gamma_{th}\Delta T_o + \Gamma_{abs}c_{th}|a_o|^2; \tag{4.6}$$

and

$$\dot{a_1} = -\left[i\Delta_o - ig_{th}\Delta T_o + \frac{\kappa}{2}\right] a_1 - [i\Delta_1 - ig_{th}\Delta T_1]\, a_o; \tag{4.7}$$

$$\dot{\Delta T_1} = -\gamma_{th}\Delta T_1 + \Gamma_{abs}c_{th}(a_o a_1^* + a_o^* a_1); \tag{4.8}$$

where $\Delta'_o = \Delta_o - g_{th}\Delta T_o$ is the time-averaged (DC) detuning for the hot-cavity. From equations (4.3) and (4.4), the time-averaged cavity field amplitude, $a_o = \sqrt{\kappa_{ex}}s/(i\Delta'_o + \frac{\kappa}{2})$, and the time-averaged temperature increase of the cavity, $\Delta T_o = \Gamma_{abs}c_{th}|a_o|^2/\gamma_{th}$. Thus the cavity temperature increase is proportional to the external input power, and inverse proportional to the heat capacity of the cavity (cavity mode volume), as discussed in section 4.5.1.

Because the cavity field damping damping rate, $\kappa/2$ is much fast than the thermal damping rate of the cavity, γ_{th}, we can use rate equation approximation for the first order perturbation equations (4.7) and (4.8), and obtain

$$a_1 = \frac{i[g_{th}\Delta T_1 + \Delta_1]a_o}{i\Delta'_o + \frac{\kappa}{2}}. \tag{4.9}$$

This yields,

$$a_o a_1^* + a_o^* a_1 = \frac{2g_{th}\Delta T_1|a_o|^2\Delta'_o}{{\Delta'_o}^2 + \frac{\kappa^2}{4}} - \frac{2|a_o|^2\Delta_1\Delta'_o}{{\Delta'_o}^2 + \frac{\kappa^2}{4}}. \tag{4.10}$$

Plugging equation (4.10) into equation (4.8),

$$\dot{\Delta T_1} = -\left[\gamma_{th} - \frac{2\Gamma_{abs}c_{th}g_{th}|a_o|^2\Delta'_o}{{\Delta'_o}^2 + \frac{\kappa^2}{4}}\right]\Delta T_1 - \frac{\Gamma_{abs}c_{th}2|a_o|^2\Delta_1\Delta'_o}{{\Delta'_o}^2 + \frac{\kappa^2}{4}}. \tag{4.11}$$

Taking the Fourier transform of equation (4.11), it yields,

$$\tilde{\Delta T_1}(\Omega) = \frac{-\frac{\Gamma_{abs}c_{th}2|a_o|^2\Delta'_o}{{\Delta'_o}^2+\frac{\kappa^2}{4}}}{\gamma_{th} - \frac{2\Gamma_{abs}c_{th}g_{th}|a_o|^2\Delta'_o}{{\Delta'_o}^2+\frac{\kappa^2}{4}} + i\Omega}\tilde{\Delta}_1(\Omega). \tag{4.12}$$

On the other hand, the laser detuning with regard to the hot cavity contains the time-averaged terms and the first-order perturbation terms,

$$\Delta'_{th} = [\Delta_o - g_{th}\Delta T_o] + [\Delta_1 - g_{th}\Delta T_1] = \Delta'_o + \Delta'_1, \tag{4.13}$$

where $\Delta'_1 = \Delta_1 - g_{th}\Delta T_1$ is the first order laser detuning fluctuations with regard to the hot cavity.

Thus the spectrum of the laser detuning fluctuations is

$$\tilde{\Delta}_1'(\Omega) = -g_{th}\Delta\tilde{T}_1(\Omega) + \tilde{\Delta}_1(\Omega). \tag{4.14}$$

Plugging equation (4.12) into equation (4.14), we have the spectral density of the laser detuning fluctuations wrt the hot cavity:

$$|\tilde{\Delta}_1'(\Omega)|^2 = \frac{\gamma_{th}^2 + \Omega^2}{[\gamma_{th} + \alpha P_{in}]^2 + \Omega^2}|\tilde{\Delta}_1(\Omega)|^2; \tag{4.15}$$

where $\alpha = \frac{\mathrm{d}n}{\mathrm{d}T}\frac{\omega_o}{n_o}\Gamma_{abs}c_{th}\frac{2\kappa_{ex}\Delta_o'}{\left[\Delta_o'^2 + \frac{\kappa^2}{4}\right]^2}$. $|\tilde{\Delta}_1(\Omega)|^2$ is in fact the spectral density of the free-running laser frequency fluctuations $S_{\omega\omega}(\Omega)$. We can define the thermo-lock reduction gain of laser frequency noise (wrt to cavity) as

$$R(\Omega) = \frac{\gamma_{th}^2 + \Omega^2}{[\gamma_{th} + \alpha P_{in}]^2 + \Omega^2}. \tag{4.16}$$

From equation (4.15), it can be seen that the thermo lock bandwidth, αP_{in} is proportional to the input power. And when $\Omega \gg [\gamma_{th} + \alpha P_{in}]$, the frequency noise reduction gain $R(\Omega) \approx 1$. This is reasonable as the laser frequency noise components fluctuating faster than the thermo lock bandwidth is not affected by the cavity thermo-lock. Moreover, when $\Omega \ll \gamma_{th}$ (the intrinsic thermo damping rate), $R(\Omega) \approx \frac{1}{[1+\alpha P_{in}/\gamma_{th}]^2}$.

4.5.3 Measurement of Laser Frequency Noise Reduction Due to Thermo Lock

In order to measure the power spectral density of the laser frequency noise fluctuations with regard to cavity under thermo lock, we can consider the transmitted cavity power fluctuations. This is because the cavity resonance lineshape acts as a frequency discriminator to convert the frequency noise to power fluctuations in the transmitted signal. The power spectral density of the cavity transmission, $S_{PP}(\Omega)$, is related to the power spectral density of the laser frequency noise $S_{\omega\omega}^{las-cav}(\Omega)$,

$$S_{PP}(\Omega) = P_{in}^2 H(\Omega) S_{\omega\omega}^{las-cav}(\Omega), \tag{4.17}$$

where P_{in} is the input power, and $H(\Omega)$ is the direct cavity transfer function, which has the following form [74],

$$H(\Omega) = \frac{\kappa_{ex}^2}{\left[\Delta^2 + \kappa^2/4\right]^2}\frac{4\Delta^2(\kappa_i^2 + \Omega^2)}{\left[(\Delta+\Omega)^2 + \kappa^2/4\right]\left[(\Delta-\Omega)^2 + \kappa^2/4\right]}. \tag{4.18}$$

When the Fourier frequency $\Omega \ll \kappa$, the cavity transfer function can be written as a simple form,

$$H = \frac{4\kappa_{ex}^2\kappa_i^2\Delta^2}{\left[\Delta^2 + \kappa^2/4\right]^4}. \tag{4.19}$$

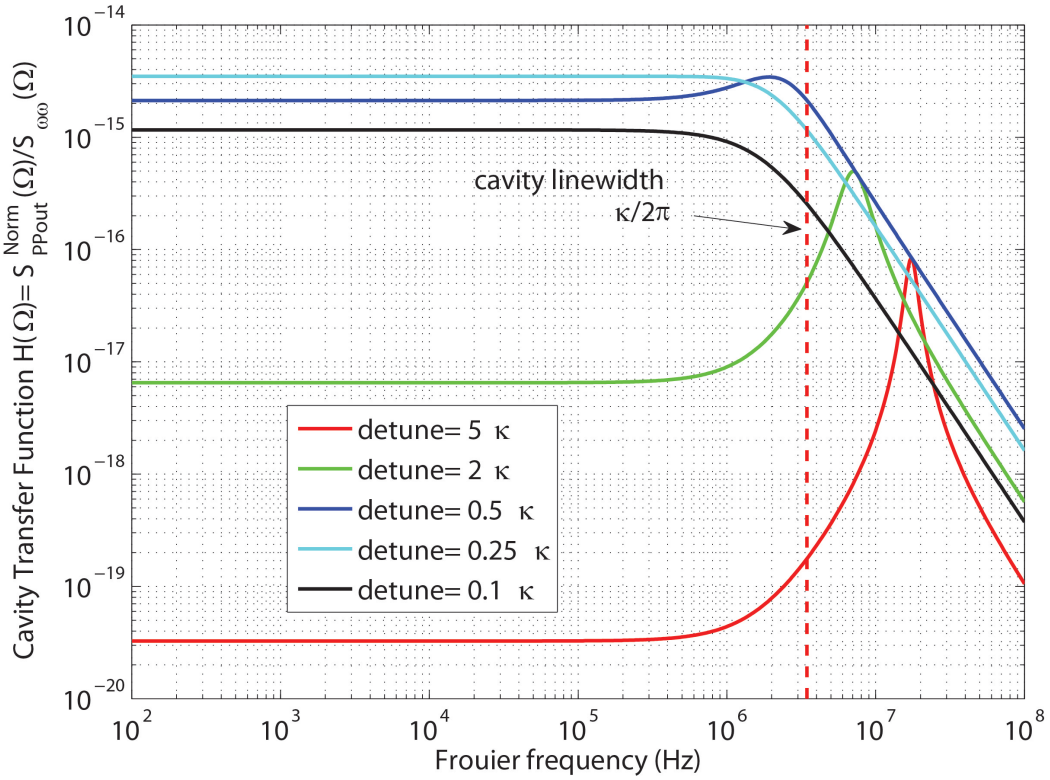

Figure 4.8: **Direct cavity transfer function.** The direct cavity transduction $H(\Omega)$ is plotted under different detunings. The cavity is critically coupled and the loaded cavity linewidth $\kappa/2\pi = 3.45$ MHz. The cavity transfer function is almost constant for Fourier frequencies much less than the cavity linewidth, showing DC response of the cavity discrimination of laser frequency noise. When detuning $\Delta > \kappa$, the transfer function peaks when the Fourier frequency equals to the detuning.

Equation (4.19) is a constant value, independent of the Fourier frequency. That is the DC response of the cavity Lorentzian lineshape. Also, we can see the cavity transfer function depends on different detunings (Δ). Figure 4.8 plots the transfer function for a cavity with loaded linewidth ($\kappa/2\pi$) of 3.45 MHz at critical coupling, from far away from resonance (5κ) to close to resonance (0.1κ). The DC response of cavity transfer is shown when the Fourier frequency is much less than the cavity linewidth. Also, it is interesting to note that when detuning $\Delta > \kappa$, the transfer function peaks at the Fourier frequency which is equal to the detuning. This is because the Fourier components (Ω) of the laser frequency noise get maximum enhancement by the cavity resonance when $\omega_l \pm \Omega = \omega_o$.

A 3 mm disk resonator with loaded linewidth of 3.45 MHz at critical coupling is used for the measurement of laser frequency noise while thermo-locked to a cavity resonance using an external cavity diode laser (ECDL). A series of input power levels (from 0.4 mW to 14.5 mW) is used and at each power level, the laser is detuned at half linewidth point (i.e., $\Delta = \kappa/2$). The measurement results are given in figure 4.9. The magenta curve in figure 4.9a is the background noise when the

laser is off-resonance, which is coming from the laser RIN and shot noise. The rise of the background noise at large Fourier frequencies is due to the division of shot noise to the cavity transfer function. Also plotted is the free-running laser frequency noise, measured independently by a Mach-Zehnder Interferometer (MZI). We can see that at low input power (e.g., 0.4 mW), the laser frequency noise measured by the cavity is in good agreement with the one measured by MZI, for Fourier frequencies above 1 kHz, which is the thermo lock bandwidth at this power level. As the input power increases, the laser frequency noise measured by the cavity gets more suppressed, and the thermo lock bandwidth increases too.

Taking the ratio between the thermo-locked and free-running frequency noises, we can get the thermo lock reduction gain of laser frequency noise, $R(\Omega)$, which is plotted in figure 4.9b. It is clear that the thermo lock reduction gain and also its bandwidth increase with the increase of the input power. Also plotted are the calculated reduction gain curves using corresponding power levels, which is in good agreement with the measured curves. Also note that the thermo reduction gain is 0 dB for large Fourier frequencies above the thermo lock bandwidth, as shown in equation (4.16).

4.6 Phase Noise Transfer Function of a Microcomb

The RF noise of a microcomb is a very complex and important subject in the development and applications of microcombs. In section 3.7 and 3.8, we showed that the microcomb RF spectrum can be a single RF tone, multiple tones, and broad RF beat notes. Based on the discussion in [54], it is the noncommensuration between the primary comb line spacing (Δ) and the native comb spacing (δ), and the merging of the subcombs that cause these involved characteristics of microcomb RF noise. In this section, we mainly study noise contributions to the microcomb RF phase noise (single-sideband phase noise spectrum) when the microcomb exhibits a reasonably stable, single RF tone. Two important noise sources are considered, e.g., the frequency noise and the relative intensity noise of the pump noise. Physically, the laser frequency noise will induce intracavity power fluctuations, which modulates the cavity refractive index through the Kerr-nonlinearity and temperature change. Likewise, the intensity noise of the pump laser is coupled into the cavity directly. Thus these two noise sources are important factors contributing to the comb RF phase noises.

The effects of the free-running laser frequency noise and RIN are considered for the phase noise a 36 GHz microcomb based on fused-quartz rods [47]. However, the measurement was based on the DC response of the laser frequency drift and intensity change. Here we devised a scheme to measure the full frequency response (from 100 Hz to 30 MHz) of the comb phase noise due to laser phase modulation (PM) and intensity modulation (IM). Moreover, we point out the importance of thermo-lock to the comb phase noise, because the frequency fluctuations between the pump laser and cavity (which introduces power and refractive index fluctuations) are greatly suppressed within

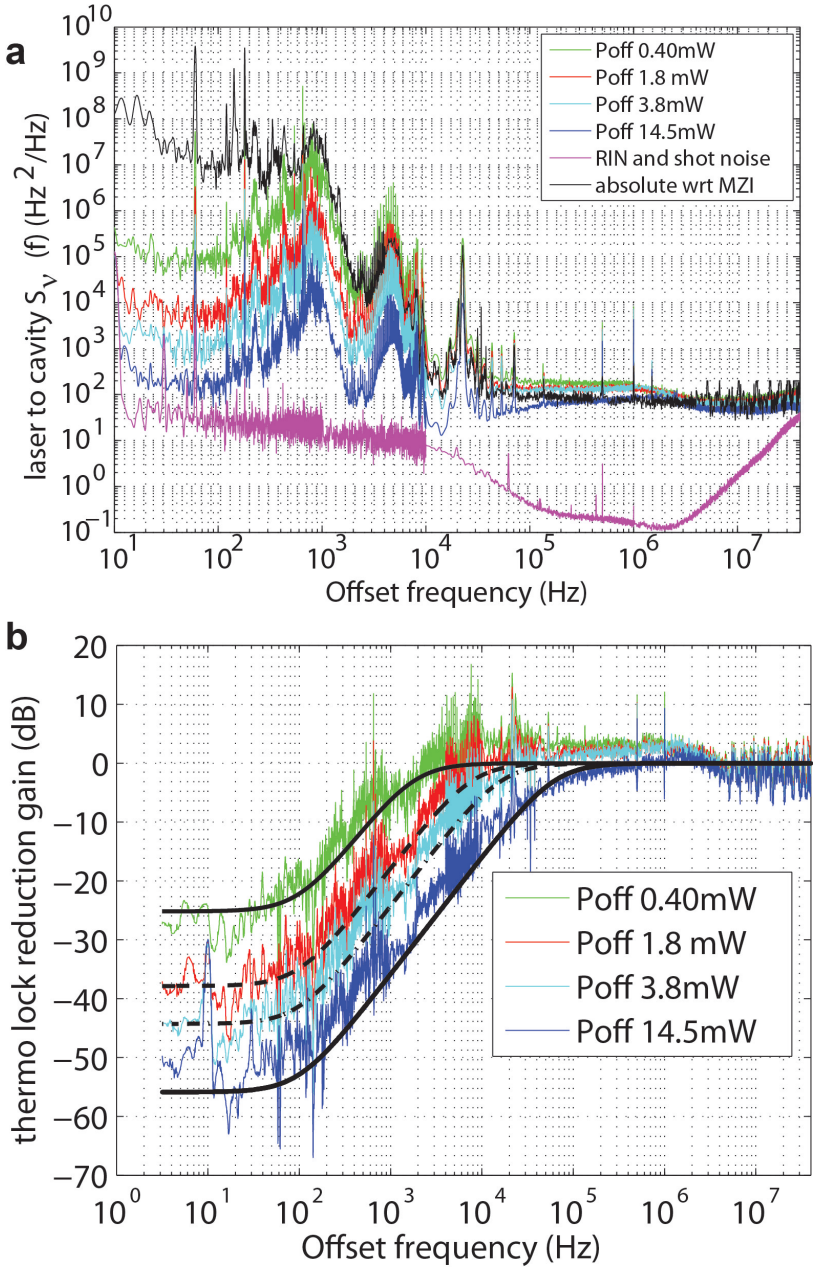

Figure 4.9: **Measurement of laser frequency noise reduction due to thermo lock.** (a) The laser frequency noise spectrum while thermo locking to a cavity is measured at different input power levels. With the increase of input power, the laser frequency noise is more suppressed wrt the cavity and the thermo lock bandwidth increases too. The back curve is the free-running laser frequency noise measured by an independent MZI, with no thermo locking. The magenta curve is the background noise due to laser RIN and shot noise. Background noise rises above 1MHz is a result of the shot noise divided by the cavity transfer function. (b) The thermo lock reduction gain of laser frequency noise is plotted with the increase of the input power levels. The black curves are the calculations based on equation (4.16), using the corresponding input power levels.

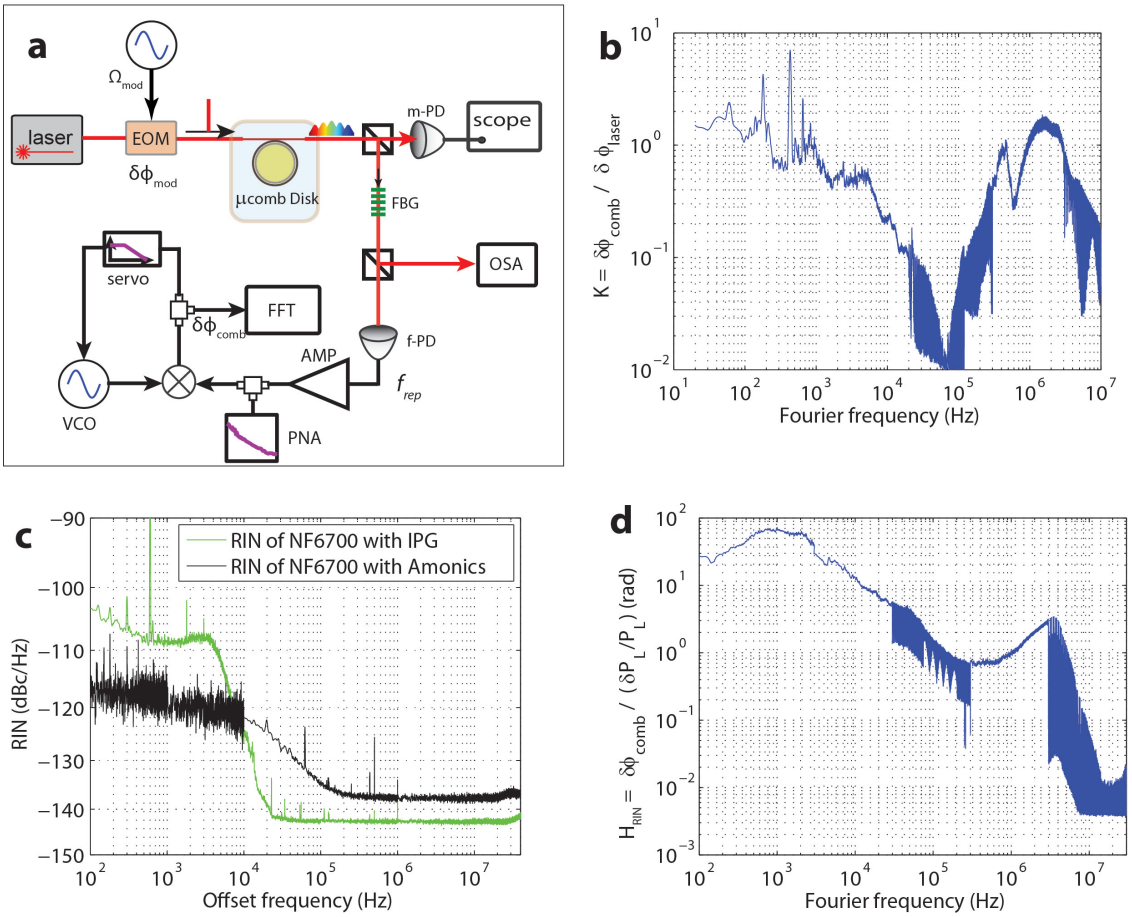

Figure 4.10: **Measurement of transfer function of microcomb phase noise from laser FM and AM noise.** (a) Experiment setup for the measurement of a 22 GHz microcomb phase noise transfer function by laser phase modulation (or intensity modulation). (b) The measured comb phase noise transfer function from laser phase modulation, $K = \frac{\delta\phi_{comb}}{\delta\phi_{laser}}$. (c) Laser relative intensity noise (RIN) using two different a IPG EDFA and Amonics EDFA. (d) Measured comb phase noise transfer function from laser intensity modulation. $H_{RIN} = \frac{\delta\phi_{comb}}{\delta P/P}$.

the thermo-lock bandwidth, compared with the free-running laser frequency fluctuations.

The experimental setup for measuring the comb phase noise transfer function is given in figure 4.10a. An EOM phase modulator (or intensity modulator) is used to introduce PM (or IM) sideband tones on the pump laser. The microcomb, with linespacing 22 GHz from a 3 mm disk resonator, is filtered using a FBG notch filter to reject the CW pump. The demodulated comb RF signals, containing the original comb RF tone at 22 GHz, and the induced sidebands due to pump laser PM (or IM) actuation, are amplified and phase compared to a frequency synthesizer VCO through a loose phase-lock-loop (PLL). The phase amplitude of the comb RF sideband can be inferred by analyzing the baseband spectrum of the phase comparator output (mixer IF channel). The comb

phase noise transfer function from the laser phase noise is defined as

$$K(\Omega) = \frac{\delta\phi_{comb}(\Omega_{mod})}{\delta\phi_{laser}(\Omega_{mod})}. \tag{4.20}$$

Likewise, the transfer function of the comb phase noise from the laser intenisty modulation, is defined as

$$H_{RIN}(\Omega) = \frac{\delta\phi_{comb}(\Omega_{mod})}{\delta P(\Omega_{mod})/P_o}. \tag{4.21}$$

Using the described measurement scheme, the full frequency responses of the microcomb phase noise from PM and IM are measured. Figure 4.10b shows the frequency response due to PM ($K(\Omega)$), from ∼100 Hz to 10 MHz. Figure 4.10d shows the frequency response due to IM ($H_{RIN}(\Omega)$), from 100 Hz to 30 MHz. Also, figure 4.10c gives the measured laser RIN using two different EDFAs for the experiment, e.g., the IPG EDFA and the Amonics EDFA. The frequency noise of the pump laser (ECDL) is given in figure 4.9.

With the measured form of the transfer function of microcomb phase noise from pump laser PM and IM, we can project the microcomb RF phase noise, using the laser frequency noise spectrum and RIN spectrum. Because the thermo lock reduces the frequency fluctuations between the pump laser and cavity resonance, the frequency noise under thermo lock should be used as the input FM noise source term. Thus the projected comb phase noise from laser phase noise, $S_\phi^{laser}(\Omega)$, under thermo lock is

$$S_\phi^{comb}(\Omega) = |K(\Omega)|^2 S_\phi^{laser}(\Omega). \tag{4.22}$$

And the projected comb phase noise from laser RIN, $S_I^{laser}(\Omega)$, is given as,

$$S_\phi^{comb}(\Omega) = |H_{RIN}(\Omega)|^2 S_I^{laser}(\Omega). \tag{4.23}$$

Figure 4.11 gives the projected comb phase noise (single-sideband phase noise $L_\phi(f)$) using the two input noise sources of the pump laser phase noise and RIN. The red curve is the actual measured comb RF phase noise. The cyan curve is the laser phase noise under thermo lock. The blue curve is the projected comb phase noise based on equation (4.22). And the green and black curves are the projected comb phase noise based on equations (4.23), using the measured two RIN spectra by IPG and Amonics EDFA in figure 4.10c. We can see that the major noise source to the comb RF phase noise is the laser phase noise. And the projection based on the laser phase noies and measured transfer function agrees well with the measured comb phase noise. The contribution from the laser RIN is much lower than the measured value.

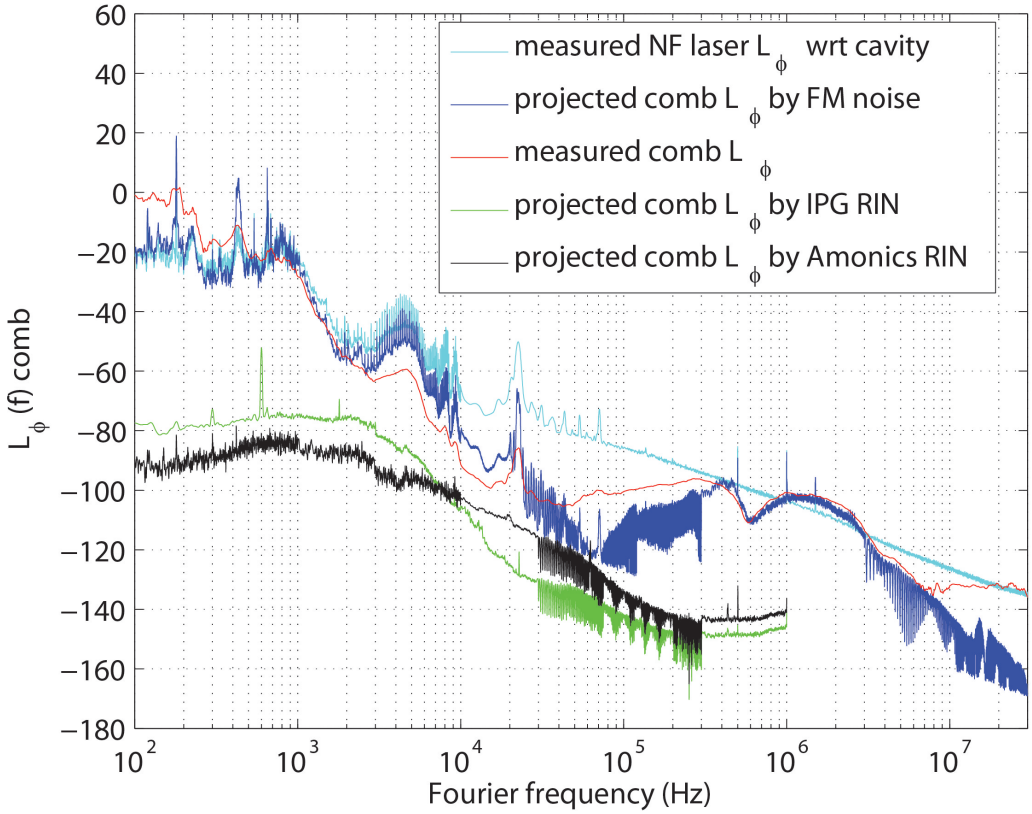

Figure 4.11: **Projected microcomb RF phase noise.** Two input noise sources, i.e., the pump laser frequency noise and intensity noise (RIN), are considered for their effects on the comb RF phase noise. Because thermo lock reduces the relative frequency fluctuations between the pump laser and the cavity, the reduced laser frequency noise under thermo lock bandwidth is considered as the input noise source to the system. The cyan curve is the measured laser phase noise with respect to the cavity under thermo lock. And the blue curve is the projected comb RF phase using the laser frequency noise and the measured transfer function $K(\Omega)$. Similarly, the contribution to comb phase noise from the laser RIN using two different EDFAs are also plotted, shown as the green (IPG EDFA) and the black (Amonics EDFA) curves. The red curve is the actual comb RF phase noise. We can see that the main noise source contributing to the comb RF phase noise is the laser frequency noise under thermo lock. Also the projected comb phase noise using the laser frequency noise (thermo-locked) is in good agreement with the measured comb phase noise.

4.7 Shot-noise-limited Microcomb RF Phase Noise

In section 4.6, we studies the frequency response of microcomb RF phase noise from 100 Hz to 10 MHz, and see the important noise source to the microcomb phase noise is the pump laser frequency/phase noise under thermo lock. At even larger offset (Fourier) frequencies, the microcomb phase noise exhibits a white noise characteristic, independent of the offset frequency. It is very likely that the white phase noise part is determined by the thermal (Johnson) noise of the photodetector load impedance (low optical incident power), or the photon shot noise (high incident power). Typically, these microcomb white phase noises are in the range of -110 dBc/Hz to -135 dBc/Hz [47, 52, 58, 75]. Thus the relative high values of these demonstrated white phase noises implies that these microcombs are operated in the thermal-noise limited region upon photodetection. Realizing shot-noise-limited region of microcomb phase noise is important for applications like low-noise microwave generation [33, 76]. Typically, the generated photocurrent should be greater than ∼1 mA to access the shot-noise limited region (shot noise greater than thermal noise). High output power of the microcomb lines is a critical factor to achieve the shot-noise microcomb phase noise.

In this section, we report on the first realization of a shot-noise-limited microcomb phase noise. A white single-sideband phase (SSB) noise level of -156 dBc/Hz for a 22 GHz microcomb is measured for a generated average photocurrent of 7.9 mA. The measured SSB phase noise of the microcomb is given in figure 4.12a. The microcomb operates at a fixed state, while the incident power levels are changed by adjusting the optical attenuation level to the fast photodetector. Then the SSB phase noise is measured correspondingly at these power levels. The average photocurrent (I_{DC}) is 7.9, 4, 2, 1, 0.5, 0.25, 0.063 mA from lower to upper phase noise curves. The lowest SSB phase noise curve (red) shows a white phase noise of -156 dBc/Hz. The inset of figure 4.12a gives the RF spectrum of the micocomb beat note, with span 1 MHz and RBW 1 kHz. The optical spectrum of the microcomb is givein in figuer 4.12b. In order to verify that the white phase noise measured at 7.9 mA (red curve in figure 4.12a) is indeed photon shot-noise limited, we plot the white phase noise level versus the generated average photocurrent (I_{DC}) in figure 4.12d. The measured white phase noise (yellow square markers) first shows a -20 dB per decade dependence with the photocurrent when I_{DC} <∼1 mA, and then shows a -10 dB per decade dependence with photocurrent when I_{DC} >∼1 mA. These two distinct photocurrent dependences agree very well with the thermal-noise-limited region and shot-noise-limited region of microwave generation by frequency combs [33]. Thus we have demonstrate, for the first time, a shot-noise-limited microcomb phase noise as low as -156 dBc/Hz, which is also a record low value for microcombs.

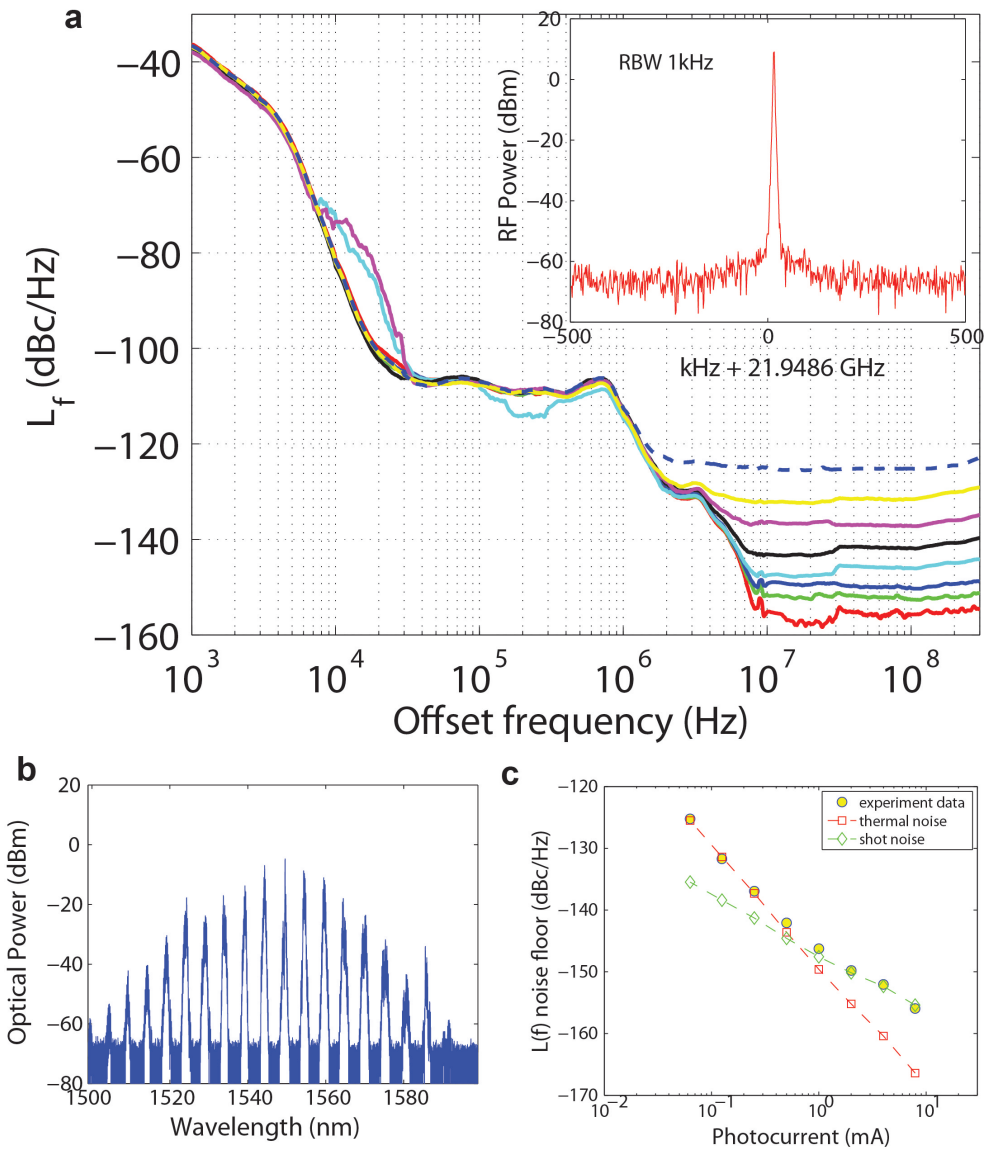

Figure 4.12: **Shot-noise-limited microcomb phase noise.** (a) The single-sideband phase noise of a 22 GHz microcomb is plotted. The incident optical power on to the fast photodetector (PD) from the generated microcomb is gradually decreased from the lower to upper phase noise curves by adjusting an attenuator before the PD. The average photocurrent(I_{DC}) is 7.9, 4, 2, 1, 0.5, 0.25, 0.063 mA from lower to upper phase noise curves. The inset is a RF spectrum of the microcomb beat note centered at 21.9486 GHz. (b) The optical spectrum of the 22 GHz microcomb is plotted. (c) The white phase noise of the microcomb is plotted versus the generated photocurrent. The experimental data (yellow circles) shows two distinct photocurrent-dependence regions. When I_{DC} <∼1 mA, the white phase noise floor shows a -20 dB/dec dependence with the photocurrent, which is a characteristic of thermal noise limited phase noise. When I_{DC} >∼1 mA, the white phase noise floor shows a -10 dB/dec dependence on the photocurrent, a characteristic of shot-noise limited phase noise. The square markers and the diamond markers are the calculated white phase noises based on thermal noise+NF of the RF amplifier, and the shot noise, respectively.

4.8 Stabilization of the Repetition Rate of Microcomb

Full stabilization of microcomb spectral lines requires the stabilization of two parameters, the comb repetition rate (f_{rep}) and the comb offset frequency(f_{ceo}), as each comb tooth can be determined by $f_m = f_{ceo} + mf_{rep}$. This requires an octave-spanning spectrum with stable enough line spacing beat signal. Nevertheless, other possible stabilization schemes, which involve two independent parameters, can also be applied. For example, stabilization of f_{rep} and any single microcomb tooth (typically the pump laser), or stabilization of two microcomb teeth. These methods do not require an octave-spanning spectrum. However, they need another optical frequency reference for the stabilization of the comb tooth, e.g. an independent fiber comb, an atomic reference, or an ultrastable reference cavity.

Microcomb repetition rate (line spacing) control has been demonstrated for a 86 GHz toroid device by feedback to the pump current of EDFA [50], and recently mechanical control to fused-quartz microrod device by squeezing the resonator directly through a piezo-electric element [77]. Here, we demonstrate stabilization of the beat note of a microcomb by feedback control using an acousto-optical modulator (AOM). The actuation mechanism for beat note tuning is pump power modulation. Figure 4.13a gives the measured tuning curve of a 22 GHz microcomb beat note with the increase of the pump power. The diagram for feedback control of comb line spacing is given in figure 4.13 b. A phase detector (RF mixer) generates a phase error signal between the comb beat note and the microwave synthesizer. The error signal is used for phase lock loop control by pump power modulation using an AOM. The SSB phase noise of the 22 GHz microcomb is given in figure 4.13c, with free running (red curve) and stabilized (blue curve) cases. A reduction of phase noise more than 85 dB is obtained at 10 Hz offset. The two insets of figure 4.13c show the stabilized RF beat notes, with a span of 1 MHz and 2 kHz, respectively. The spurs in the 2 kHz span spectrum (lower inset) are the harmonics of 60 Hz power line.

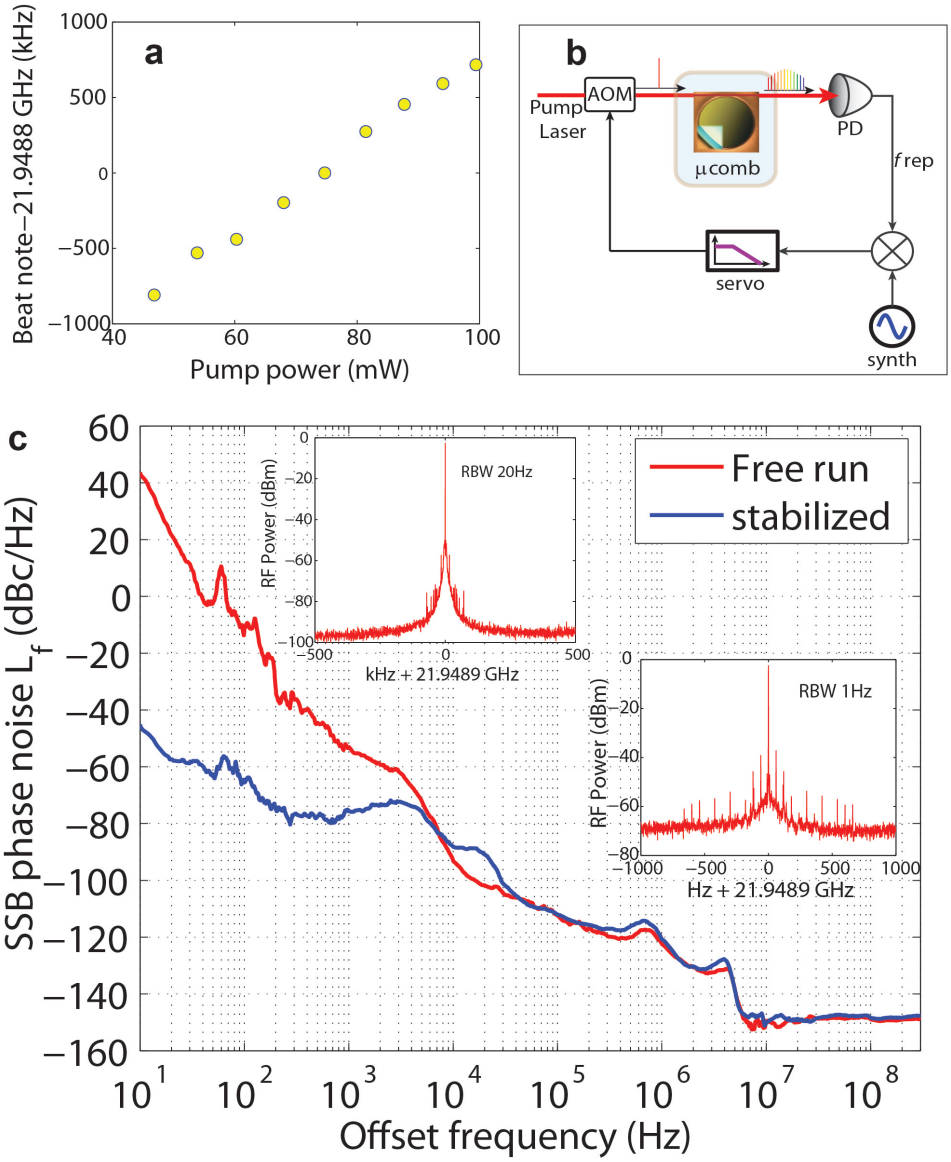

Figure 4.13: **Stabilization of microcomb repetition rate.** (a) Actuation of comb line spacing (repetition rate) is realized by modulation of the pump power. This figure plots the change of the beat note versus the change of the pump power. The microcomb optical spectrum is given in figure 4.12b. (b) Diagram for microcomb repetition rate stabilization. The microcomb RF beat note is phase compared with an microwave synthesizer and the error signal is used for phase lock loop control by pump power modulation using an acousto-optic modulator (AOM). (c) SSB phase noise of a 22 GHz microcomb. (red: free-run; blue: stabilized). Inset gives the RF spectra for the stablized beat notes, with span 1 MHz and 2 kHz, repectively. The spurs in the lower inset are the harmonics of the power line.

Chapter 5

Highly Coherent, Low-Frequency-Noise Stimulated Brillouin Lasers on Silicon

5.1 Introduction

Ultrahigh coherence (low-frequency noise) is a priority in a remarkably wide range of applications including high-performance microwave oscillators [33], coherent fiber-optic communications [78, 79], remote sensing [80], and atomic physics [81, 82]. In these applications, the laser forms one element of an overall system that would benefit from miniaturization. For example, in coherent communication systems a laser (local oscillator) works together with taps, splitters and detectors to demodulate information encoded in the field amplitude of another coherent laser source. Therein, narrow-linewidth lasers increase the number of information channels that can be encoded as constellations in the complex plane of the field amplitude [78, 79]. In yet another example, the lowest, close-to-carrier phase-noise microwave signals are now derived through frequency division of a high-coherence laser source using an optical comb as the frequency divider [33]. The miniaturization of these all-optical microwave oscillators could provide a chip-based alternative to electrical-based microwave oscillators, but with unparalleled phase noise stability. Moreover, with the advent of microcombs [6, 38], such an outcome seems likely provided that similar strides are possible in miniaturization of high-coherence sources and reference cavities. Typically, however, miniaturization comes at the expense of coherence, because quantum and technical noise contributions to laser coherence increase as laser-cavity form factor is decreased. Recently, however, there has been remarkable progress in achieving highly coherent, compact laser sources. Both Erbium and Raman microlasers with short-term, Schawlow-Townes linewidths in the range of 10 Hz have been reported [83, 84]. Also, a fully packaged narrow linewidth laser that uses feedback from an ultrahigh-Q resonator to a semiconductor laser has also been demonstrated [85].

In this chapter, we demonstrate a stimulated Brillouin laser that attains the highest level of coherence reported for a chip-based device. Schawlow-Townes noise less than 0.06 Hz^2/Hz is measured at an output power of approximately 400μW. Also significant is that the low-frequency technical noise (with effective linewidth of $\sim$1 kHz) is comparable to commercial narrow-linewidth fiber lasers (currently a benchmark for good frequency stability). The devices use a new ultrahigh-Q cavity [7] that enables precise matching of the Brillouin gain shift to the free spectral range, thereby guaranteeing reliable oscillation. The devices are efficient, featuring more than 90% conversion of lower-coherence pump to high-coherence output and threshold powers as low as 60 microwatts. Moreover, we have studied novel characteristics of this laser's operation, including cascaded operation, threshold tuning, mode-pulling phenomena, and a study of the Schawlow-Townes linewidth for the Brillouin laser. Concerning the latter, while conventional (inversion-based) optical lasers feature a Schawlow-Townes noise that is immune from thermal quanta, Brilluoin lasers, on account of coupling to the mechanical bath, feature a significant mechanical noise contribution to the laser phase noise. We both derive this contribution and use the theory to extract the thermal quanta contribution from data. Finally, the potential application of these devices as spectral purifiers for lower coherence lasers is discussed.

5.2 Stimulated Brillouin Scattering in High-Q WGM Cavities

Stimulated Brillouin scattering involves the interaction between light and acoustic (mechanical) fields in a dielectric due to the coupling by electrostriction effect [86]. In a simple quantum mechanical picture, a pump photon $(\mathbf{k}_p, \Omega_p)$ annihilates and scatters in to down-shifted Stokes photon $(\mathbf{k}_s, \Omega_s)$ and an phonon $(\boldsymbol{\beta}_B, \Omega_B)$, shown in figure 5.1a. This process satisfies energy and momentum conservation rules:

$$\begin{aligned} \Omega_p &= \Omega_s + \Omega_B, \\ \boldsymbol{k}_p &= \boldsymbol{k}_s + \boldsymbol{\beta}_B. \end{aligned} \tag{5.1}$$

For backward Brillouin scattering, equation (5.1) gives the Brillouin shift frequency, $\Omega_B/2\pi = 2nV_a/\lambda_p$, where V_a is the acoustic wave velocity and λ_p is the pump wave wavelength. This process is originally a parametric process. However, under the cases that the acoustic field decays much faster than optical field, the resulting adiabatic elimination of the more strongly damped (acoustic) field results in corresponding amplification of the other, less-strongly damped (optical) field. This turns the parametric process into a stimulated scattering process.

Stimulated Brillouin scattering in silica fibers [87] has been utilized to generate narrow-linewidth fiber lasers [88, 89], slow light [90], and microwave signals [91, 92]. However, stimulated Brillouin laser

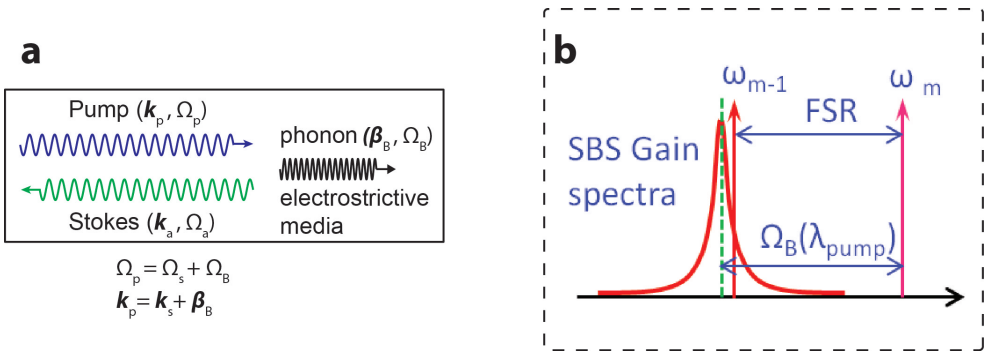

Figure 5.1: **SBS in WGM cavities.** (a) Stimulated Brillouin Scattering (SBS) in a dielectric with electrostriction. The process involves a pump photon $(\mathbf{k}_p, \Omega_p)$, a down-shifted Stokes photon $(\mathbf{k}_s, \Omega_s)$, and a scattered phonon $(\boldsymbol{\beta}_p, \Omega_p)$. Energy and momentum conservations are to be satisfied in the scattering process. (b) SBS in a WGM cavity. The narrow bandwidth of the SBS gain spectrum ($\sim$ 20–60 MHz in silica) requires the pump mode (ω_m) and Stokes mode (ω_{m-1}) to align with the Brillouin gain profile.

in high-Q whispering-gallery-mode (WGM) microresonators had been elusive because the required energy and momentum conservations of the photon and phonon modes in WGM cavities are difficult to achieve simultaneously. Simply put, realization of microcavity based SBLs requires precise match of a pair of cavity modes to the Brillouin shift, as illustrated in figure 5.1b. Specifically, the narrow bandwidth ($\sim$20–60 MHz in silica) of the Brillouin gain [93] requires better than 1:1000 control of the resonator diameter to obtain a match and more realistically it requires 1:10000 control for consistent low-threshold turn-on power. In the recent demonstrations of SBS in high-Q SBS cavities [15, 16], a statistical approach was implemented in which the high spectral density of transverse modes in CaF_2 resonators [15] or silica spherical cavities [16] offered a reasonable likelihood of finding a reasonably well-matched pair of resonator modes.

In the present work, the statistical approach [15, 16] is replaced by the precision control of the cavity free spectral range (FSR) using a ultrahigh-Q planar disk resonator geometry [7]. These devices are the first chip-based Brillouin devices. Their coherence sets a record for frequency stability of any chip-based device. Moreover, the fine lithographic fabrication of the devices enables a series of studies of the novel properties of the chip-based Brillouin lasers, including cascaded operation, frequency pulling, threshold tuning, etc.

5.3 Theoretical Derivations of SBS Threshold and Cascaded Operation

The couple mode equations for the pump mode and the different orders of Brllouin Stokes modes are given as:

$$\begin{cases} \dot{a} = [i\Delta - \frac{\kappa}{2}]a + \sqrt{\kappa_{ex}}s - g^c b^2 a, \\ \dot{b_1} = -\frac{\kappa}{2}b_1 + g_c a^2 b_1 - g^c b_2^2 b_1, \\ \dot{b_2} = -\frac{\kappa}{2}b_2 + g_c b_1^2 b_2 - g^c b_3^2 b_2, \\ ... \\ \dot{b_N} = -\frac{\kappa}{2}b_N + g^c b_{N-1}^2 b_N, \end{cases} \tag{5.2}$$

where a is the cavity pump field, b_i is the ith Stokes field, s is the launched pump field, κ_{ex} is the external coupling rate, and $\kappa = \kappa_{ex} + \kappa_o$ is the total photon damping rate for the loaded cavity. Also a, b_i are normalized such that their square modulus are the intracavity mode energies, s is normalized such that $|s|^2$ gives the incident pump power. Here g^c is the cavity Brillouin gain and is related to the bulk Brillouin gain parameter g_0 by $g^c = \frac{c^2 g_0}{n^2 V_{eff}(1+\frac{4\Delta\Omega^2}{\Gamma^2})}$ (Lorentzian Brillouin gain spectrum), where V_{eff} is the mode volumn, Γ is the Brillouin phonon damping rate, $\Delta\Omega$ is the offset of the cavity FSR to the Brillouin shift frequency. The coupled mode equations (5.2) resembles to the cascaded Raman rate equations [94].

Let's first consider the Brillouin scattering to the first-order Stokes only. Taking N=1 in equation (5.2), it is easy to find that

$$|a|^2 = \frac{\kappa}{2g^c}, \tag{5.3}$$

$$s_{th} = \frac{\kappa a}{2\sqrt{\kappa_{ex}}}. \tag{5.4}$$

Thus the intracavity pump field is clamped due to the onset oscillation of the first-order Stokes. Also, equation (5.3) is the threshold field energy inside the cavity for particular Stokes order to excite a higher order Stokes. From equation (5.4), the threshold power for the first-order Stokes is

$$P_{th} = |s_{th}|^2 = \frac{\kappa^3}{8\kappa_{ex} g^c} \overset{C.C.}{=} \frac{\pi^2 n^2 V_{eff}}{g_b Q_T^2 \lambda^2}, \tag{5.5}$$

where "C.C." means "critical coupling" ($\kappa_o = \kappa_{ex} = \kappa/2$), and $g_b \equiv \frac{g_0}{1+\frac{4\Delta\Omega^2}{\Gamma^2}}$.

The output power for the first-order Stokes versus the input pump power is

$$P_{1st} = \sqrt{\frac{2\kappa_{ex}^3}{\kappa g_c} P_{in}} - \frac{\kappa\kappa_{ex}}{2g^c} \overset{C.C.}{=} P_{th}(\sqrt{\frac{P_{in}}{P_{th}}} - 1). \tag{5.6}$$

Equation (5.6) shows that the output power the first-order Stokes is proportional to the square root of the pump power. If the intracavity energy of the first-order Stokes reaches the threshold value, $\frac{\kappa}{2g^c}$ (equation (5.3)), the output power of the first-order Stokes is then clamped, and the intracavity energy of the pump is unclamped. This process can be cascaded into even higher-order

Stokes. It is easy to derive the threshold pump power for the second-order Stokes is

$$P_{th,2nd} = \frac{\kappa^3}{2\kappa_{ex} g^c} \overset{C.C.}{=} \frac{4\pi^2 n^2 V_{eff}}{g_b Q_T^2 \lambda^2}. \tag{5.7}$$

The output power for the second-order Stokes versus the input pump power is

$$P_{2nd} = \frac{\kappa_{ex}^2}{\kappa^2} P_{in} - \frac{\kappa \kappa_{ex}}{2g^c}, \tag{5.8}$$

where we can see the output power of the second-order Stokes is linearly dependent on the pump power. The different kinds of output power dependence of the first(odd)- and second(even)-order Stokes on the pump power is similar to the case of cascased Raman scattering in WGM cavities [94], where similar coupled mode of equations were applied.

5.4 SBS Resonator Device and Experimental Setup

The combination of ultrahigh-Q and precision control of FSR has not previously been possible, and is essential for reliable fabrication of low-threshold SBL lasers. Very briefly, the fabrication of these devices uses an 8-10 micron thick thermal oxide layer that is lithographically patterned and etched into circular disks using buffered HF. The etched, oxide disks then act as a mask for selective, dry-etching of the silicon. This dry etch process creates a whispering gallery resonator through undercut of the silicon. By proper control of both the wet and dry etching processes, the Q of the resulting resonator can be nearly 1 billion. Moreover, the lithography and etching process provide diameter control of 1:20,000, giving only 0.5 MHz of FSR uncertainty for a cavity of 10 GHz FSR. This level of control is more than sufficient to place the microcavity FSR within the Brillouin frequency shift. Figure 5.2b shows a top view of a resonator fabricated using this procedure. Additional details on fabrication and characterization of these resonators are described in [7].

Figure 5.2a shows the experimental setup used to test the SBLs. Pump power is coupled into the resonator by way of a fiber taper coupler [13, 14]. Stimulate Brillouin laser (SBL) emission (odd-orders) is coupled into the opposing direction and routed via a circulator into a photodiode and an optical spectrum analyzer. The transmitted pump wave is monitored using a balanced homodyne receiver so as to implement a Hänsch-Couillaud locking of the pump to the resonator [95, 96]. Figure 5.2c shows the typical experimental traces for the transmitted pump, back-propagating Stokes wave slightly above threshold and the Hänsch-Couillaud error signal as the pump laser is scanned across the microcavity resonance.

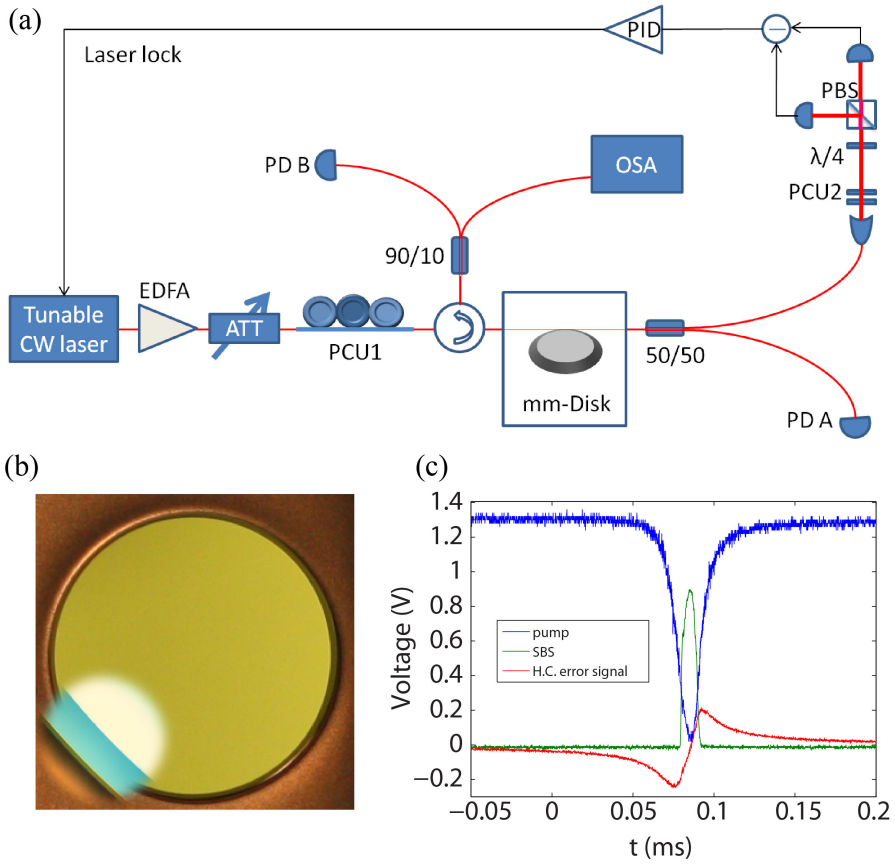

Figure 5.2: **Experimental setup.** (a) A tunable CW laser is amplified through an EDFA and coupled into the disk resonator using the taper-fiber technique. The SBL emission in the backward direction propagates through the fiber circulator, and is monitored by a photodetector (PD B) and an optical spectrum analyzer (OSA). The pump is monitored by a separate photodetector (PD A) and is also coupled to a balanced-homodyne detection setup (Hänsch-Couillaud technique) to generate an error signal for locking the pump laser to the cavity resonance. (b) A micrograph of the SBL disk resonator used in this experiment. The disk has a diameter of approximately 6.02 mm. (c) Experimental oscilloscope traces for transmitted pump, back-propagating SBL and Hänsch-Couillaud error signal.

5.5 Cascaded versus Single-line Brillouin Laser Action

By proper control of taper loading, the SBL can be operated in two distinct ways: cascade or single-line. Figure 5.3(a) shows the optical spectrum of a single-line SBL and figure 5.3(b) shows the spectrum for cascaded operation up to the 9th order. In cascade, the waveguide loading is kept low so that once oscillation on the first Stokes line occurs, it can function as a pump wave for a second Brillouin wave and so on. Single-line operation, on the other hand, is often desirable in system applications [78, 79] and can be obtained by increasing the resonator waveguide coupling. While cascading can still be made to occur at a sufficiently high pumping power, increased waveguide loading forestalls this process by increasing the oscillation threshold. Significantly, there is no penalty in efficiency as a result of the increased waveguide loading. Indeed, because the internal loading on the pump rises with increased Stokes power, one can preset the waveguide loading to an overcoupled condition such that the pump wave will become critically coupled only at the desired Stokes power. Alternately, in cases where waveguide coupling can be varied, the coupling can be adjusted so as to always achieve critical coupling of the pump as the first-order Stokes wave increases in power. Figure 5.3(c) shows just this scenario. The power of the first-order Stokes laser line is plotted versus the pump power with the cavity loading adjusted to maintain critical coupling in each step. A linear relationship is obtained and the differential pumping efficiency is 95%.

It is also interesting to measure the dependence of the different SBL Stokes emission lines with respect to the pump power. In section 5.3, we have shown that the first-order Stokes power scales with the square root of the pump power while the second-order Stokes power scales linearly with the pump power (given a fixed taper-fiber coupling condition). Figure 5.4(a) shows the output power of the 1st-order Stokes line versus pump power with the cavity loading fixed (at critical coupling below threshold), and also a curve fitting using $P_{th}\left(\sqrt{\frac{P_{in}}{P_{th}}}-1\right)$. The flattening of the first-order power for pump power exceeding 150 μW results from the onset of threshold for the second-order Stokes line. On account of gain clamping, the first-order Stokes line (now acting as the pump wave for the second-order Stokes laser oscillation) experiences circulating power clamping beyond this power. Figure 5.4(b) shows the output power of the second-order Stokes emission versus input pump power with the cavity loading fixed. The linear dependence is, again, consistent with observations reported earlier for cascaded Raman laser action.

5.6 Frequency Pulling in the SBL

Frequency/mode pulling in a conventional laser oscillator is well studied. In a laser having an atomic gain medium, the atomic dispersion modifies the round-trip phase of the intracavity field and "pulls" the laser oscillation frequency from the passive cold cavity value toward that of the atomic resonance

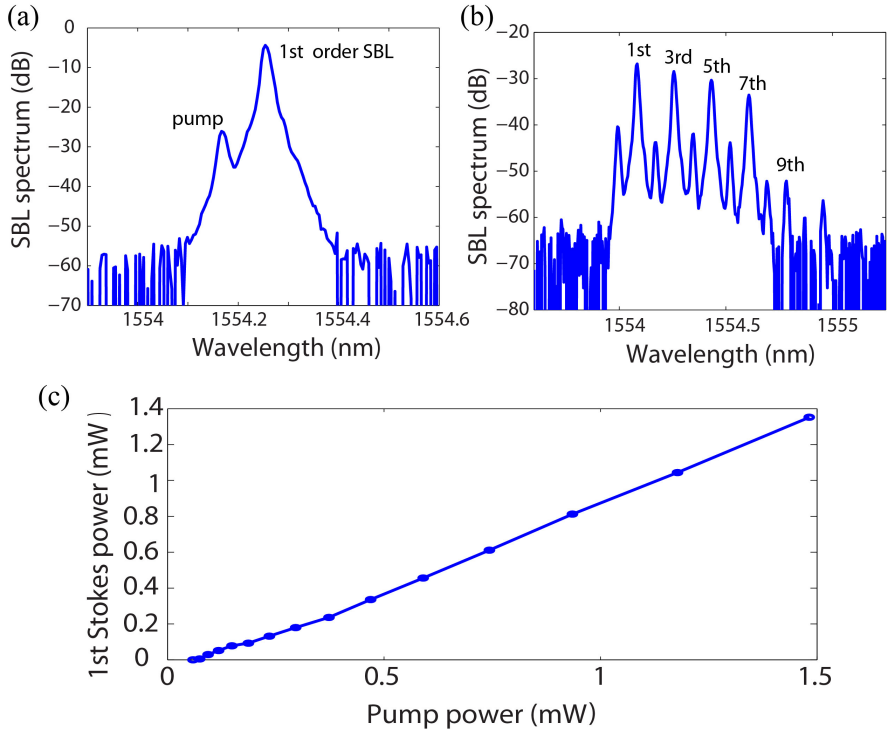

Figure 5.3: **SBL optical spectra and output power versus pump power for single-line operation.** (a) A spectrum showing single-line SBL operation wherein only the first-order emission line is excited. (b) Spectrum showing cascaded SBL operation up to the 9th order. In both figures, the spectrum is collected in the backward direction with the pump and even order SBL emission lines suppressed on account of their propagation in the forward direction (i.e., the observed, weak level for these signals in the spectrum is a result of weak back-reflection in the experimental setup). (c) Output power of the first-order Stokes wave while adjusting the cavity loading so as to maintain critical coupling in each step. The differential efficiency is around 95%.

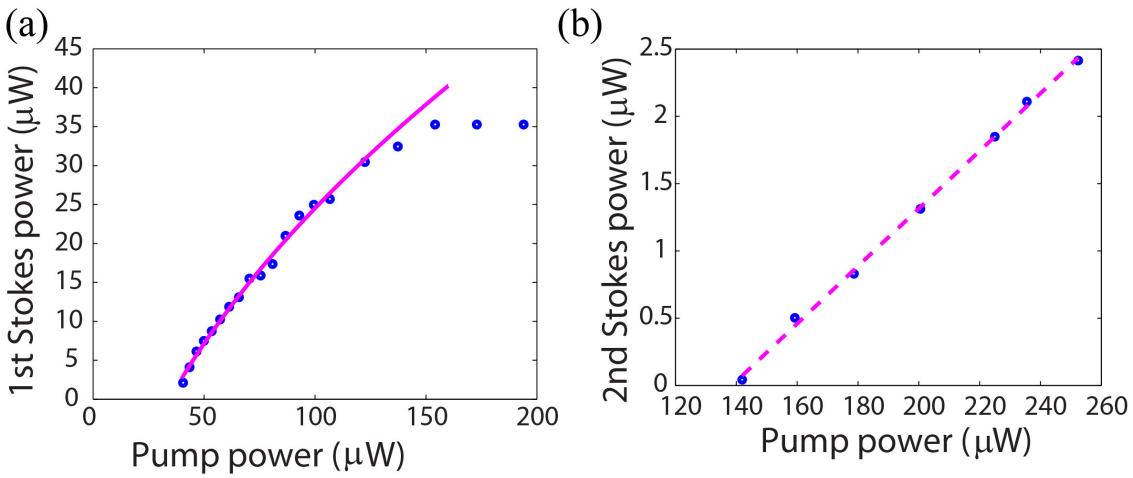

Figure 5.4: **SBL output power dependence on pump power in cascaded operation.** (a) Experimental output power of the first-order SBL versus the pump power. A threshold of 40 μW is obtained. The output power of the first-order SBL is clamped for pump power above 150 μW because the second-order SBL begins oscillation. Also shown is the fitted curve using $P_{th}\left(\sqrt{\frac{P_{in}}{P_{th}}}-1\right)$. (b) Experimental output power of the second-order SBL versus the pump power. Also shown is the linear fit with respect to the pump power.

[97]. The Brillouin gain can also introduce dispersive phase shift inside the microcavity. Recently, mode pulling in a fiber Brillouin laser was accounted for to explain frequency tuning range under a novel strain tuning mechanism [98]. However, to the authors' knowledge there has never been a quantitative measurement of mode pulling in Brillouin lasers.

To model the pulling, in modification to the coupled mode equations (5.2), we introduce the detuning of the oscillating waves to the cold-cavity eigen-frequency, and also the imaginary part of the SBS gain. Let us consider a pump field, A (frequency ω_p), first-order Stokes field, a (frequency ω_s), with corresponding "cold cavity" resonant frequencies ω_o and ω_1. The fields are normalized so that their square modulus gives the photon number in the cavity. They satisfy the following equations of motion:

$$\dot{A}_o = [i(\omega_p - \omega_o) - \kappa/2]A_o + i\sqrt{\kappa_{ex}}s - g^c|\alpha|^2 A_o, \tag{5.9}$$

$$\dot{\alpha} = [i(\omega_s - \omega_1) - \kappa/2]\alpha + g^c|A_o|^2\alpha, \tag{5.10}$$

$$g^c = \frac{g_0^c}{1+\frac{2i[\omega_p-\omega_s-\Omega]}{\Gamma}} = \frac{g_0^c(1-\frac{2i\Delta\Omega}{\Gamma})}{1+\frac{4\Delta\Omega^2}{\Gamma^2}}, \tag{5.11}$$

where A_o and α are the slowly varying amplitudes for the pump and the stokes fields, $\Delta\Omega = \omega_p - \omega_s - \Omega_B$, and Γ is the full-width half maximum linewidth of the Brillouin gain. Also, Ω_B is the Brillouin shift frequency, which depends on the pump wavelength λ_p according to $\Omega/2\pi = \frac{2nV_A}{\lambda_p}$, n is the refractive index of silica and V_A is the acoustic velocity in silica. Also, κ is the photon

damping rate of the loaded cavity, and κ_{ex} is the waveguide coupling rate. s is the input pump field amplitude, normalized such that $|s|^2$ gives the incident photon rate. (As an aside, equation (5.11) is valid in the limit that the Brillouin linewidth is narrower than the Brillouin shift. This condition is satisfied in the present system.)

The real part of equation (5.11) gives the Brillouin gain spectrum with Lorentzian line shape and the imaginary part is dispersive component that will "pull" the Brillouin oscillation frequency. Steady state solution of these equations yields the following pair of equations,

$$|A_o|^2 = \frac{\kappa}{2}\frac{1+\frac{4\Delta\Omega^2}{\Gamma^2}}{g_0^c}, \tag{5.12}$$

$$\omega_s - \omega_1 - \frac{g_0^c\frac{2\Delta\Omega}{\Gamma}}{1+\frac{4\Delta\Omega^2}{\Gamma^2}}|A_o|^2 = 0. \tag{5.13}$$

Equation (5.12) gives the threshold intracavity pump photon number. Equation (5.13) is the frequency pulling equation. Substituting equation (5.12) into equation (5.13) gives the first-order Stokes lasing frequency ω_s. In the experiment, the beat frequency between the pump and first-Stokes wave is measured ($\Delta\omega_{beat} = \omega_p - \omega_s$) and this is given by the following expression

$$\Delta\omega_{beat} = \frac{1}{1+\frac{\kappa}{\Gamma}}(\Delta\omega_{FSR} + \frac{\kappa}{\Gamma}\Omega_B), \tag{5.14}$$

where $\Delta\omega_{FSR} = \omega_o - \omega_1$ is the cold cavity free spectral range. Usually, $\Gamma/2\pi \approx \times$ (20 - 60) MHz for silica waveguides. Also, $\kappa/2\pi \approx \times 1$ MHz in our cavity so that $\kappa \ll \Gamma$. Under these conditions, equation (5.14) can be approximated in the following form,

$$\Delta\omega_{beat} - \Delta\omega_{FSR} = \frac{\kappa}{\Gamma}(\Omega_B - \Delta\omega_{FSR}), \tag{5.15}$$

where $\Delta\omega_{beat} - \Delta\omega_{FSR} = \omega_1 - \omega_s$ is the frequency pulling caused by Brillouin dispersion. Note that the effect of this equation is to pull the Stokes lasing frequency toward the line center of the Brillouin gain (in analogy to the atomic resonance in conventional laser systems). Moreover, when the FSR matches the Brillouin shift, the frequency pulling is zero.

Figure 5.5 summarizes the experimental results of the frequency pulling study. In this measurement, the pump wavelength is sequentially tuned along the cavity modes within the same mode family. The SBL threshold, cold-cavity FSR and Brillouin beat frequency are measured at each wavelength. Also plotted are the linear fits to the cold cavity FSR and Brillouin beat as well as quadratic fit to the threshold power. Considering the threshold behavior first, the quadratic fitting of the threshold power is in agreement with equation (5.12). The minimum threshold corresponds to excitation at the peak of the Brillouin Lorentzian gain spectrum (i.e., the cold cavity FSR = Brillouin shift), and the rise of the threshold corresponds to excitation at frequency detunings that

are progressively further away from the gain peak. It is easily shown that $\frac{d\Omega_B}{d\lambda_p} = -\frac{\Omega_B}{\lambda_p} = -2\pi\times$ 7 MHz/nm [7], meaning that 1nm increase of the pump wavelength will decrease the Brillouin shift by 7 MHz. Thus, from the quadratic fit, the Brillouin gain bandwidth is estimated to be $\Gamma/2\pi =$ 51 MHz. The cavity mode has intrinsic Q of 300 million, giving a corresponding value for $\kappa/2\pi$ of 1.29 MHz at critical coupling. Thus from equation (5.15), where all terms depend on λ_p, the frequency pulling coefficient $\frac{d\Delta\omega_{beat}}{d\lambda_p}$ is estimated to be $-2\pi\times$ 0.20 MHz/nm. The linear fit in figure 5.5 gives $\frac{d\Delta\omega_{beat}}{d\lambda_p} = -2\pi\times$ 0.19 MHz/nm (and $\frac{d\Delta\omega_{FSR}}{d\lambda_p} = -2\pi\times$ 0.02 MHz/nm). The theoretical and experimental pulling rates are therefore in good agreement.

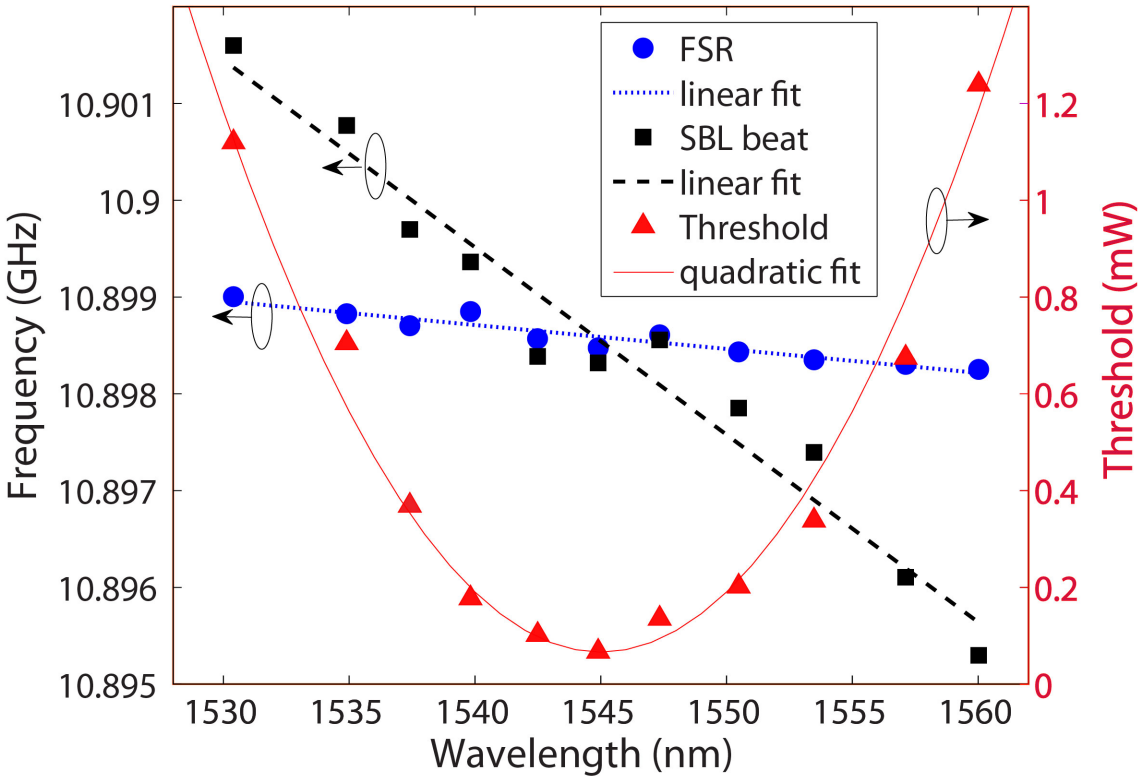

Figure 5.5: **SBL mode pulling measurement.** The measured cold cavity FSR (circles), Brillouin beat frequency (squares) and SBL threshold power (triangles) are plotted versus the pump wavelength. The linear fit of the cold cavity FSR gives a slope of $-2\pi\times$ 0.02 MHz/nm and the fit of the Brillouin beat frequency gives a slope of $-2\pi\times$ 0.19 MHz/nm. The quadratic fit of the threshold power yields the Brillouin gain linewidth of $2\pi\times$ 51 MHz.

5.7 Threshold Tuning of SBS by Cavity Size and Pump Wavelength

From the threshold equation (5.5) of the SBSoscillation, we can see that beyond the importance of high cavity Q factor evident in this expression, it is essential to maintain a large SBL gain parameter, $g_b \equiv \frac{g_0}{1+\frac{4\Delta\Omega^2}{\Gamma^2}}$ (where $\Delta\Omega$ is roughly the difference between the cavity FSR to the Brillouin shift). Because the gain spectrum is relatively narrow (typical full-width half maximum is 20-60 MHz [93, 99]), this requires a precise match of the free-spectral-range to the Brillouin shift. We have already shown that Ω_B depends on the pump wavelength λ_p and phonon velocity V_a through the relation $\Omega_B/2\pi = 2nV_a/\lambda_p$. An illustration of the control possible using the new resonator geometry is provided in figure 5.6a where four devices having diameters of 6020, 6044, 6062 and 6080 microns (lithography mask size) were tested at a series of pump wavelengths in the 1500 nm band. In each device, the pump wavelength was sequentially tuned along resonances belonging to the same azimuthal mode family. The minimum threshold for each device corresponds to excitation at the Brillouin gain maximum (i.e., $g_b(\Delta\Omega = 0)$). The rise in threshold away from the minimum (for a given resonator diameter) reflects tuning of the Brillouin shift frequency with pump wavelength noted above. The variation of this peak frequency shift versus the corresponding pump wavelength is plotted in figure 5.6c. There is good agreement with the expected theoretical dependence.

5.8 Fundamental Linewidth of Stimulated Brillouin Laser

The Hamiltonian for parametric coupling of a mechanical field, b (frequency Ω), and a Stokes field, a (frequency ω_1), that is induced by a pump field $A(t)$ (via matrix element μ) is given by [100–102]:

$$H = \hbar\omega_1 a^\dagger a + \hbar\Omega b^\dagger b + \frac{\hbar\mu}{2}\left(A(t)^* ba + A(t)a^\dagger b^\dagger\right). \tag{5.16}$$

where this Hamiltonian omits energy non conserving terms. Introducing slowly varying operators for the Stokes and the mechanical fields, and also treating the blue pump mode as a classical, nondynamical field, the relevant equations of motion are

$$\dot{\beta}^\dagger = -\frac{\Gamma}{2}\beta^\dagger + i\frac{\mu}{2}A_o^*\alpha e^{i\Delta\Omega t} + F(t), \tag{5.17}$$

$$\dot{\alpha} = \left[i(\omega_s - \omega_1) - \frac{\kappa}{2}\right]\alpha - i\frac{\mu}{2}A_o\beta^\dagger e^{-i\Delta\Omega t} + f(t), \tag{5.18}$$

where α and β are the slowly varying operator fields for the Stokes and the mechanical fields; Γ (κ) is the mechanical (optical) energy decay rate, $\Delta\Omega = \omega_p - \omega_s - \Omega$, and where $F(t)$ and $f(t)$ are Langevin

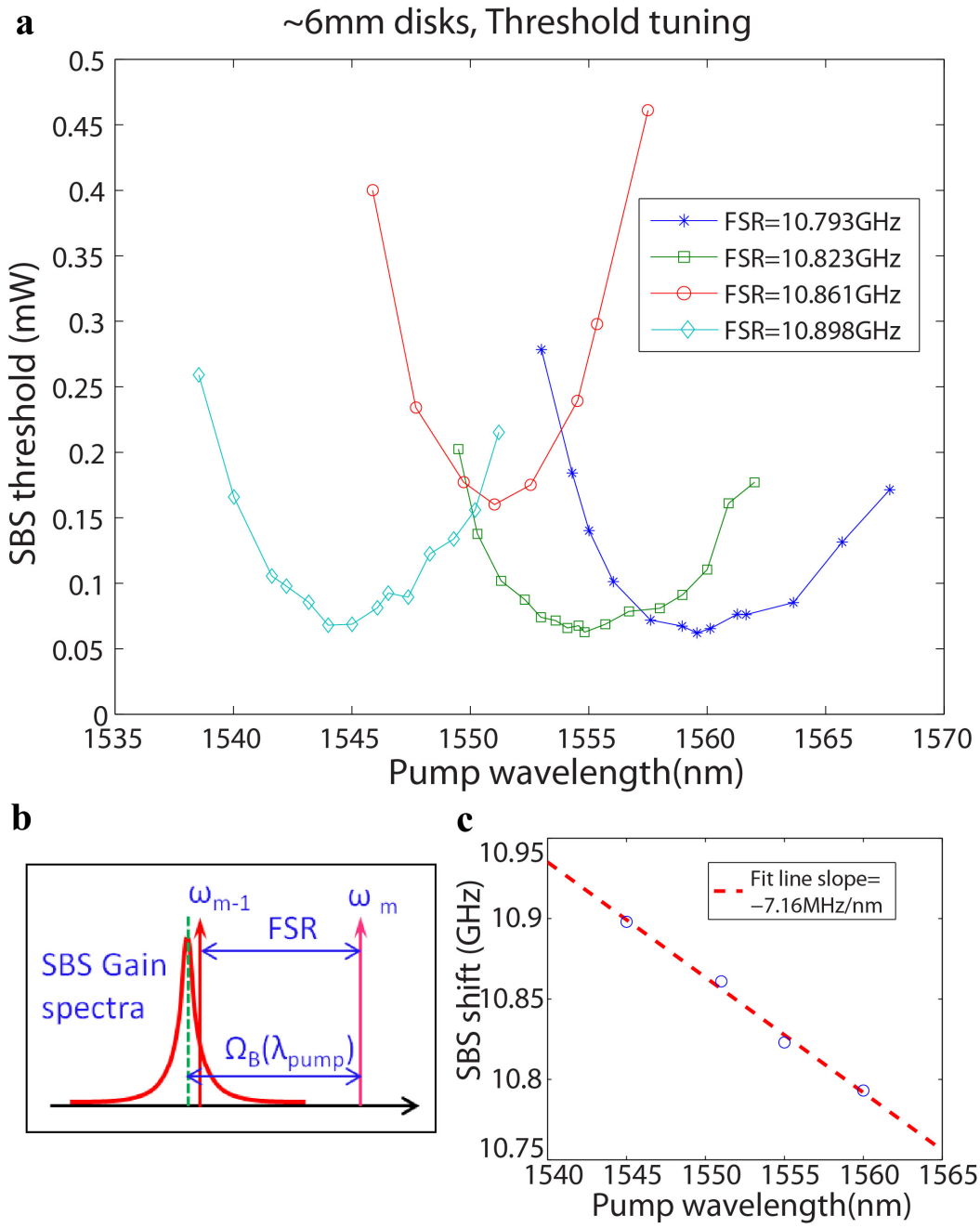

Figure 5.6: **Illustration of tuning control of the SBL devices.** (a) SBL threshold is measured as a function of pump wavelength using four slightly different resonator diameters. FSRs are indicated in the legend. (b) Illustration of the control of the SBS gain with the change of FSR and pump wavelength. (c) Measured Brillouin-shift frequency (circles) versus pump wavelength.

operators with the standard normalization for damped oscillators [103, 104]. We now restrict the solution of these equations to a regime in which the mechanical field is much more strongly damped than the optical field. This is a case typical of the devices considered in this study. The resulting adiabatic elimination of the more strongly damped field results in corresponding amplification of the other, less-strongly damped field. In the regime ($\kappa \ll \Gamma$) elimination of β gives

$$\dot{\alpha} = \left[i(\omega_s - \omega_1) - \frac{\kappa}{2} \right] \alpha + g^c |A_o|^2 \alpha + h(t), \tag{5.19}$$

where g^c is the gain parameter introduced in the discussion of frequency pulling in section 5.6 and is related to the matrix element μ by $g_0^c = \mu^2/2\Gamma$. $h(t)$ is fluctuation operator that depends upon the original operators introduced in equations (5.17) and (5.18). As an aside, the adiabatic approximation applied in this analysis eliminates the possibility of contributions from the optical pump to the SBL phase noise. These contributions have been studied in Brillouin fiber ring lasers [105, 106] and also analyzed in the first reports of SBS laser action in microresonators (see equation (4) in [15]). They are suppressed by a factor $(1 + \Gamma/\kappa)^2$ or about 2000X in the current device. Nonetheless, they are interesting and potentially important in cases where pumps have large amounts of phase noise. In the current study, there was no evidence of these fluctuations in the Schawlow-Townes noise spectrum discussed below.

Analysis of the phase noise in the Stokes field using the standard approach gives the following linewidth formula

$$\Delta\nu = \frac{\kappa}{4\pi \bar{N}_S}(n_T + N_T + 1), \tag{5.20}$$

where $\Delta\nu$ is the laser linewidth in Hertz. Also, $\bar{N}_S$ and N_T are the number of coherent and thermal quanta in the Stokes field while n_T is the number of thermal quanta in the mechanical field. N_T is negligible at optical frequencies and has been included here only to indicate the symmetrical form of thermal noise contributions from the optical and mechanical degrees of freedom. The unity term in the expression is of quantum origin, and results from the two underlying degrees of freedom (optical and mechanical oscillator fields) each contributing 1/2 to the zero point (in addition to the already noted thermal occupancy). The cumulative contribution from these two sources provides the unity in the above expressions. It is also interesting to note that based upon analysis in [15] we would expect a small correction factor to equation (5.20) of the form $(1 + \kappa/\Gamma)^{-2}$ resulting from the adiabatic approximation made above. This correction would be of order of a few percent using the system parameters.

The above form of the linewidth can be rewritten in terms of more-readily measurable quantities

as follows:

$$\Delta\nu = \frac{\hbar\omega^3}{4\pi P Q_T Q_E}(n_T + N_T + 1), \tag{5.21}$$

where $Q_{T,E}$ are the total and external Q factors, and P is the output power of the Brillouin laser. In this form, the expression is similar to the Schawlow-Townes formula for an inversion-based laser. In comparing this formula to the conventional Schawlow-Townes formula, the presence of the mechanical thermal quanta (as well as their zero-point contribution) is new and alters the magnitude of the linewidth. In the present case of Brillouin oscillation near a mechanical frequency of 10.8 GHz, $n_T = 569$ and this factor greatly increases the value of the linewidth over its vacuum-noise-limited value.

To characterize the SBL frequency noise, a Mach-Zehnder interferometer having a free spectral range of 6.72 MHz is used as a discriminator and the transmitted optical power is detected and measured using an electrical spectrum analyzer (ESA). To suppress the intensity noise, the complementary outputs of the interferometer were detected using a balanced receiver. This ESA spectrum is related to the two-sided frequency-fluctuation spectral density, $S_\nu(f)$, through the following relation:

$$W_{ESA}(f) = \frac{V_{pp}^2 2\pi^2 \tau_d^2 \mathrm{sinc}^2(\tau_d f) S_\nu(f)}{R_L}, \tag{5.22}$$

where τ_d is the Mach-Zehnder delay and V_{pp} is the peak-to-peak voltage of the detected MZI output over one fringe. Using this formula, the frequency-fluctuation spectral density is plotted in the inset of figure 5.7a, at different output power levels from 47 to 375 $upmu$W (shown as different colors). The frequency-fluctuation spectra have a relatively flat (white noise) region for carrier offset frequencies above 2 MHz and then a 1/f-like region at frequencies below 2 MHz. The value of the white noise region is plotted both as a function of SBL power in figure 5.7a. Also plotted are fits to inverse SBL power according to equation (5.21). The thermal quanta of the mechanical field can be derived from the measurement values of the ST noise levels. For the device in the measurement, $Q_T = 140$ million, $Q_E = 390$ million, which gives $n_T \approx 600$. This is in good agreement with the theoretical thermal quanta value at room temperature (570). These dependences as well as calculation confirm that the measured white frequency noise component is the ST quantum noise of the laser. The minimum value of 0.06 $\mathrm{Hz}^2/\mathrm{Hz}$ for the Schawlow-Townes noise is to our knowledge the lowest recorded ST noise for any chip-based laser.

Similar measurements on the frequency noise of the SBL at different external cavity couping rates (i.e., different Q_E) are given in figure 5.7b, while keeping the output power the same. The fit curve according to equation (5.21) is in good agreement with the data. It is also interesting to note that, to the authors' knowledge, the ST noise dependence on loading has not previously been

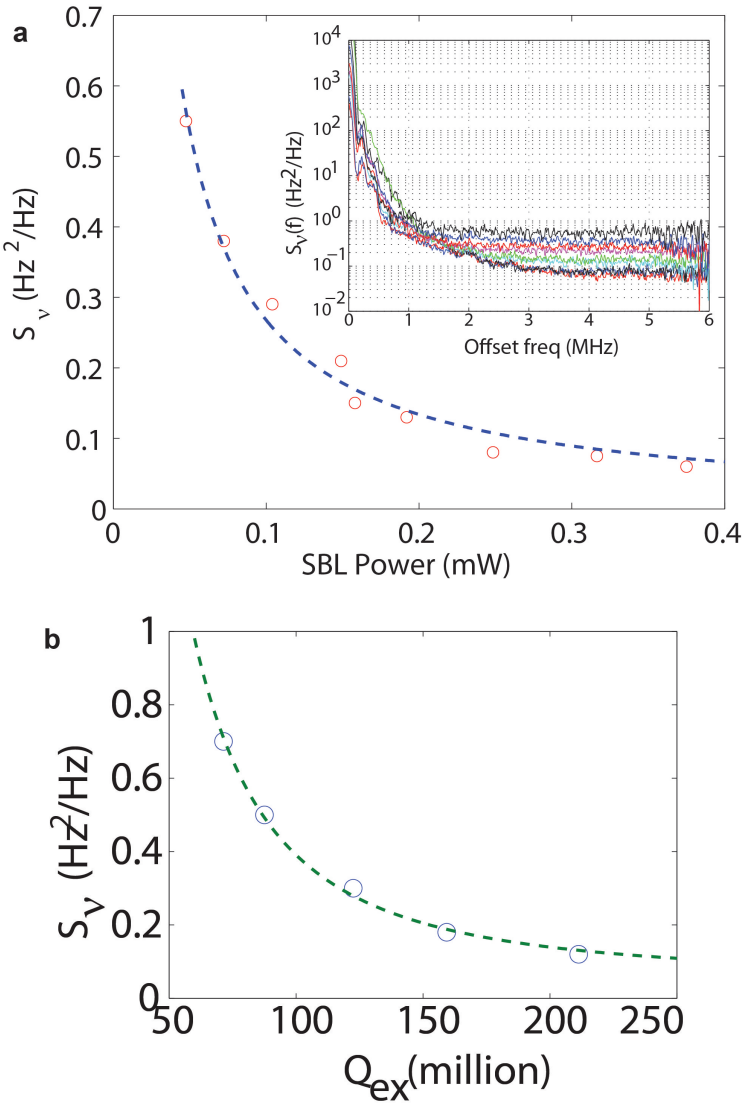

Figure 5.7: **Measurements of the power spectral density (PSD) of the SBL Schawlow-Townes-like, frequency noise.** Main panel: ST frequency noise of a highly coherent microcavity Brillouin laser on silicon is plotted versus the output power. The dashed line is an inverse power fit to the data. This gives a measured thermal quanta of the Brillouin phonon modes at room temperature (600), which is in good agreement with the calculated value (570). Inset: Power spectral density (PSD) of the microcavity Brilouin laser, measured by a balanced Mach-Zehnder Interferometer at different output power levels. The white noise part of the PSD gives the power-dependent noise in the main panel.

recorded. This, normally difficult measurement, was possible here on account of the ability to vary the taper loading of the resonator [13, 14].

The 1/f noise that appears at lower carrier offset frequencies is given in figure 5.8 and approximately tracks a similar-shaped noise spectrum in the laser pump over this frequency range. However, the absolute level of 1/f noise of the SBL at a given offset frequency is reduced by about 30dB relative to the 1/f noise in the pump. Indeed, the level of technical noise in this band is comparable to several commercial fiber lasers that were characterized as part of this study. As such, the performance of the SBL, both in the quantum limited ST regime and the technical-noise limited 1/f regime, is excellent.

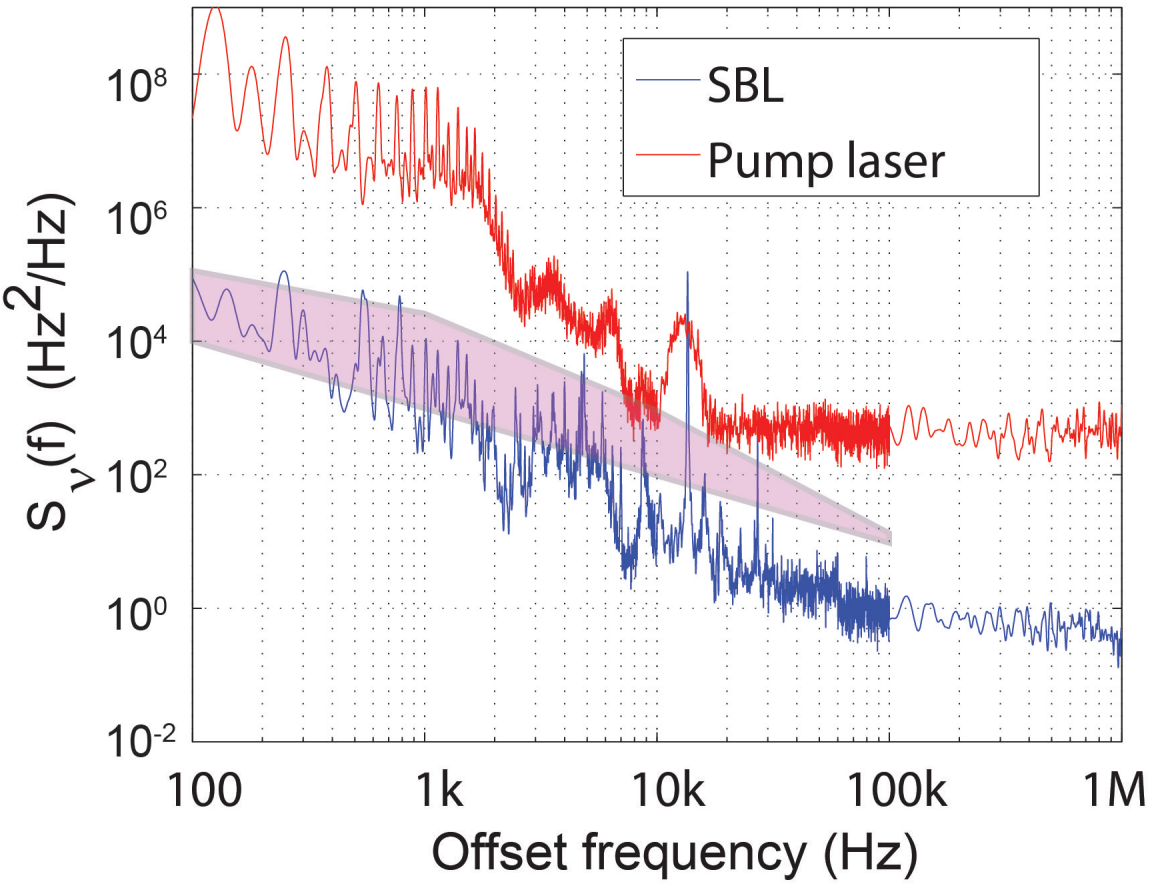

Figure 5.8: **PSD of the technical frequency noise of the microcavity Brillouin laser and the pump laser (external cavity diode laser) offset frequencies from 100 Hz to 1 MHz.** The shaded region is the frequency noise performance of commercial, narrow linewidth fiber lasers, with quoted effective linewidth from 1 to 7 kHz.

5.9 Discussion and Conclusion

The combined effect of adiabatic suppression of pump noise and very low Schawlow-Townes noise means that the SBL device studied here acts as a spectral purifier, boosting the coherence of the pump wave. The relatively small frequency shift created in this process (about 11 GHz) can be easily compensated. For example, low coherence DFB lasers are manufactured with wavelengths set on the ITU grid by control of an integrated grating pitch with fine control provided by temperature tuning of the fully packaged device. A DFB laser could be tuned through this same process to function as an SBL pump so that the emitted SBL wavelength resides at the desired ITU channel. In this way, the existing WDM infrastructure could be adapted for high-coherence operation in optical QAM systems. The frequency noise levels demonstrated here exceed even state of the art monolithic semiconductor laser by 40dB [107]. Using the measured phase noise, it is estimated that Square 1024-QAM formats could be implemented using an SBL generated optical carrier at 40GB/s.

While the current devices use a taper coupling for launch of the pump and collection of laser signal, the ability to precisely control the resonator boundary enables use of microfabricated waveguides for this process. Several designs are under investigation, the implementation of which will extend the range of applications of the SBL devices. For example, the SBLs demonstrated here are candidates for locking to a reference cavity so as to create Hertz or lower long-term linewidths. Such a source on a chip might one day be combined with microcomb technology [6] to realize a compact and high-performance microwave oscillator. At the tabletop scale, these comb-based systems have recently exceeded the performance of cryogenic electronic oscillators [33]. Also, another approach for stable, microwave generation relies upon heterodyne mixing of stable Brillouin laser lines in optical fiber [91]. The present devices would be interesting candidates for this same approach.

In conclusion, we have characterized single-line and cascaded operation up to the 9th-order in a novel chip-based Brillouin laser. Moreover, a technique for controllable operation with or without cascade has been demonstrated. SBS threshold tuning and frequency pulling, induced by the real and imaginary parts of the SBS gain have been modeled and observed. A theoretical formula for the fundamental linewidth of the SBL has been derived and we have used it to show that the thermal quanta of the mechanical mode greatly enhances the Schawlow-Townes noise of the SBL. The power spectral density of the Brilouin laser frequency noise is measured. The Schawlow-Townes frequency noise of the SBL shows an inverse dependence of the output power and a record low value of 0.06 Hz^2/Hz is obtained for a chip-based laser. The inferred valued of the thermal quanta in the mechanical mode of the present laser system is obtained from the measurement of the ST noise and agrees well the theory. Finally, the technical noise of the SBL is comparable to commerical narrow linwidth fiber lasers (with effective linewidth of $\sim$1 kHz).

Chapter 6

High Performance, Low-Phase-Noise Microwave Synthesizer on Silicon

6.1 Introduction

The generation of low phase noise radio, microwave and optical signals relies upon resonant devices that feature large storage times or equivalently high Q factors [108, 109]. Maintaining large storage time, in compact or integrated circuits, becomes increasingly challenging with decreasing size and increasing frequency [110, 111]. These two scaling laws of performance create challenges for compact or integrated microwave and millimeter-wave sources, wherein performance (in terms of phase noise at a given offset frequency) steadily degrades with increasing oscillation frequency [111]. As a result, state-of-the-art microwave oscillators are larger, discrete devices based on dielectric resonators [112]. The introduction of optical fiber for long distance communication positively impacted the frequency scaling side of this problem. First, the distribution of microwaves over optical fiber has lead to remarkable progress on transfer of low phase noise microwaves onto optical carrier waves [110, 113]. Second, fiber delay lines provided a way to create long storage time with no frequency dependent attenuation in hybrid optoelectronic oscillators (OEOs) [114]. These high-performance OEOs represented a paradigm shift in the generation of microwaves and were followed by optical resonator based versions that employed an optical microcavity to achieve the requisite oscillator storage time [115, 116]. Generally, the ability to achieve long storage times in compact, high-Q resonators has experienced a major leap forward during this same period [7, 10–12, 117, 118].

On another front, both fiber and optical resonators have also been applied to create microwaves by heterodyne of coherent laser lines [119, 120]. In this case, co-oscillation occurs within the same cavity so that a high level of common mode noise suppression leads to good performance microwave generation [119, 121]. Sideband injection locking in a master-slave laser configuration has also been

applied to enable broadband multiplication of a supplied electronic microwave signal [122]. A remarkable, recent advance has been the introduction of optical dividers in the form of frequency combs to create record low close-to-carrier phase noise microwave signal sources [33]. Frequency combs have previously been applied to stabilize optical carrier frequencies for distribution of microwaves over optical fiber [123–125], however, in this new approach an optical signal serves as the root for the ultrahigh-stability microwave signal itself. While the technique is complex, emerging technologies like frequency microcombs [6, 38] and compact reference cavities [82, 126–128] could one day lead to chip-based photonic microwave sources that exceed the performance of the best electronic sources. In a related development, microcavity-based microcombs and parametric oscillators are providing a new way to synthesize microwaves directly [47, 52, 58, 75, 77, 129]. While the performance is well off from the optical divider approach, the method is less complex.

In this work we report the application of cascaded Brillouin oscillation to microwave frequency synthesis at a level comparable to mid range commercial, all-electrical synthesizers. While fiber-based Brillouin lasers have been studied for microwave generation [91, 92, 130–132], the present device is the first chip-based Brillouin microwave source. It is also robust enough to enable incorporation as the VCO in the first demonstration of a photonic-based, microwave frequency synthesizer. Moreover, the device has a record low white phase noise floor (-160 dBc/Hz) for any microcavity-based microwave source (even including non-Brillouin based methods). It can also generate coherent microwave power in excess of 1 milliwatt without any optical or RF amplification, a significant simplification as it eliminates the need for microwave amplification stages after the photodetector. Moreover, being chip-based devices, the current sources offer integration opportunities for control and additional functions.

6.2 Microwave Generation Using Chip-based Brillouin Lasers

An ultrahigh-Q planar silica-on-silicon disk resonator [7] is used for cascaded Brillouin oscillation and microwave generation. Microcavity-based Brillouin lasers have only recently been demonstrated [15, 16, 133]. The present devices are silicon-chip based and they feature very high coherence and high quantum efficiency [7, 8]. Both high-power and low-phase-noise microwave generation from the disk resonator are achieved by cascaded stimulated Brillouin lasing and subsequent photomixing of pairs of Brillouin laser as illustrated in figure 6.1a. A narrow-linewidth fiber laser (effective linewidth 1kHz) is used as the pump laser and is coupled to the disk resonator (see photomicrograph in figure 6.1b) through a taper fiber technique [13]. The size of the disk resonator (∼6 mm) is carefully designed such that the free spectral range of the cavity matches the Brillouin gain shift [7, 8]. Once the coupled pump power reaches the stimulated Brillouin threshold, the first-order Stokes wave is excited in the backward direction and is routed through a fiber circulator to an optical spectral

analyzer, a monitor photodetector (bandwidth 125 MHz) and a fast photodetector (bandwidth 50 GHz). Further increase of the pump power leads to cascaded Brillouin lasing, e.g. 9th order Stokes has been demonstrated in our previous work [8]. These cascaded lines feature Schawlow-Townes noise less than 0.1 Hz^2/Hz [7, 8] and low technical frequency noise. As a result, they are suitable for high-stability microwave synthesis by photomixing. Fine control of this frequency is possible by adjustment of the pump frequency using acousto-optic modulation. The detected Brillouin laser can therefore function as the VCO in a microwave synthesizer as illustrated in figure 6.1c.

The Brillouin shift in the silica disk cavity is around 10.8 GHz [8], so that microwave generation from around 10.8 to 86 GHz is feasible in the present device by photomixing pairs of the cascaded Brillouin lines. We have focused on the generation of K-band (∼21.5–21.8 GHz) microwave signals by photomixing the first and third Stokes lines. Operationally, these lines feature high coherence with very low Schawlow Townes noise and technical noise; they also provide high power levels, and propagate in the same direction. It is important to note that besides the common-mode noise suppression that occurs upon photomixing because the Brillouin laser lines share a common laser cavity, combinations of laser lines that share the same optical path (i.e., odd-odd and even-even Stokes pairs) also enable cancellation of any optical-path length jitter effects.

6.3 Phase Noise of Optical VCO

To measure the phase noise of the K-band microwave signal, a phase noise analyzer (Rohde-Schwartz FSUP Signal Source Analyzer) is used. Figure 6.2 shows the single-sideband phase noise ($L(f)$) of a 21.7 GHz signal generated using the first and third Stokes laser lines for a series of output optical power levels of the third Stokes (-16.5, -10.2, -8.2, -4.5, -1.4 and 1.2 dBm from upper to lower curves). Significantly, the phase noise of this signal has $1/f^2$ dependence over 5 decades (200 Hz to 20 MHz), which corresponds to white frequency noise. Moreover, this $1/f^2$ noise has an inverse dependence on the third Stokes laser line power as shown in the inset to figure 6.2 (phase noise is measured at 100 kHz frequency offset and power is varied by changing the pump power). The inset of figure 6.2 also shows a calculated phase noise based on the Schawlow-Townes frequency noise of the third Stokes line power. For a Brillouin laser, the two-sided Schawlow-Townes frequency noise [8] can be rewritten as

$$S_\nu^{ST}(f) = \frac{kT}{8\pi^2 \tau \tau_{ex} P} \frac{c}{2nV_a}, \tag{6.1}$$

where P is output power of the Brillouin laser, τ (τ_{ex}) is the total (external) cavity photon life time, c is the speed of light, n is the refractive index of silica, V_a is the sound velocity in silica. This equation gives the limit of Schawlow-Townes noise formula [8] when the number of thermal quanta of the Brillouin phonons is far greater than unity, which is the case for measurements taken at room temperature (thermal quanta = 569). It is important to note that the Schawlow-Townes

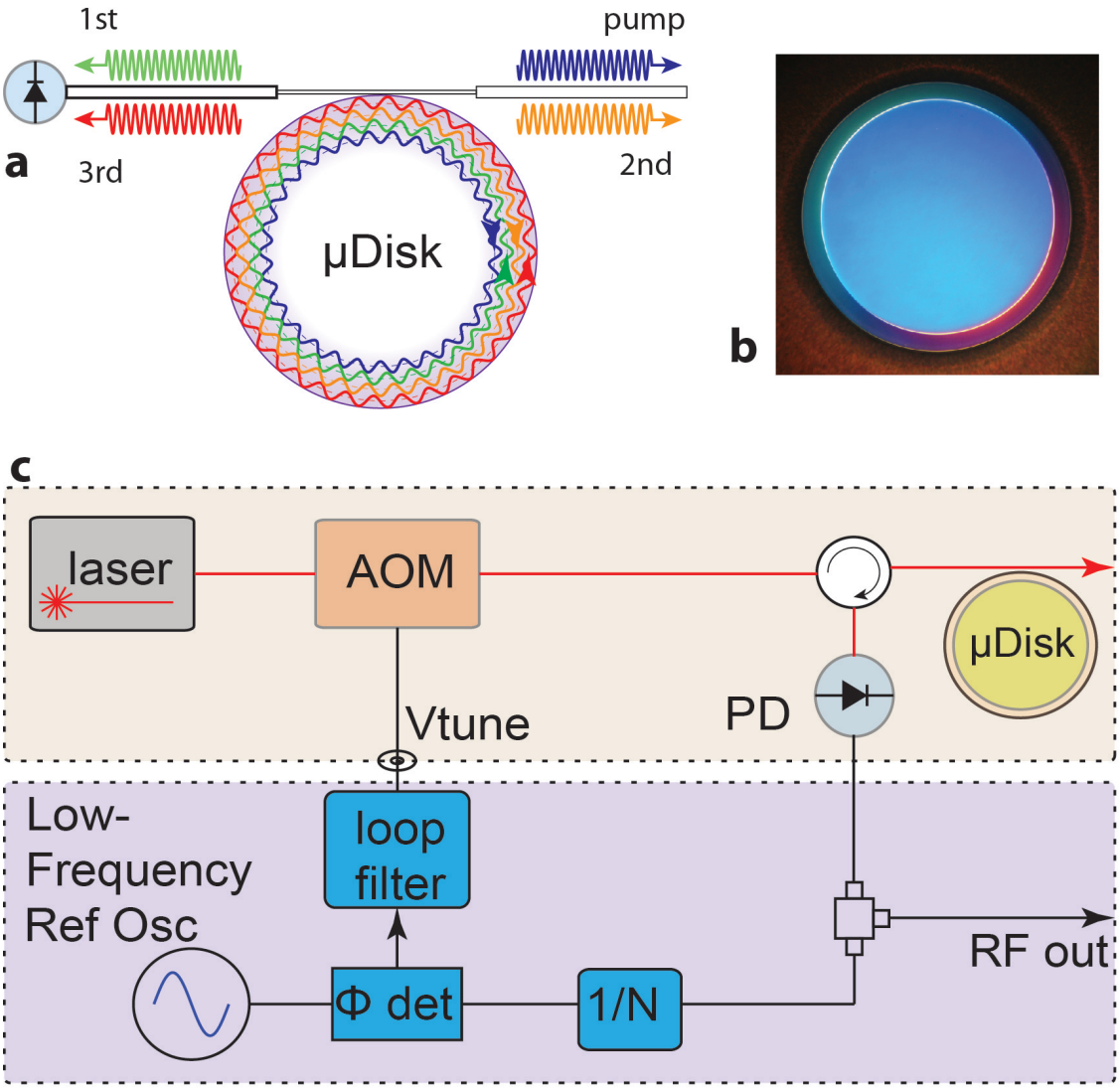

Figure 6.1: **Explanation of microwave synthesizer using chip-based Brillouin laser. a,** A Brillouin microwave oscillator showing pump (blue) and second Stokes (orange) waves and the first (green) and third (red) Stokes waves incident on the detector for microwave generation. **b,** Photomicrograph of the ultra-high-Q planar silica resonator on a silicon chip. **c,** Block diagram for a closed-loop Brillouin microwave oscillator. The open-loop Brillouin microwave oscillator (shown in the upper dashed box) functions as a voltage-controlled photonic oscillator. All hardware in the upper dashed box replaces an electrical VCO in a conventional electrical synthesizer. Components in the upper box include a pump laser, acousto-optic modulator, circulator, highspeed detector and ultrahigh-Q disk resonator.

noise is independent of both the pump frequency and the Brillouin frequency. As a result, at an equivalent power level, the phase noise levels measured in figure 6.2 would be expected if the pump frequency were higher resulting in a higher-frequency Brillouin shift. For the calculation of the Shawlow-Townes noise, measured cavity τ's of $\tau = 28$ ns and $\tau_{ex} = 34$ ns are used, (i.e., no free parameters are used), and $L(f) = 10\log(S_\phi^I(f)/2)$. Here $S_\phi^I(f)$ is the one-sided power spectral density of phase noise and is related to the two-sided power spectral density of frequency noise $S_\nu^{II}(f)$ as $S_\phi^I(f) = \frac{2S_\nu^{II}(f)}{f^2}$. Because the output optical power of the first Stokes line varies over 2.5 to 5.0 dBm from the upper to lower measurement curves (i.e., power levels much greater than for the third Stokes wave), the Schawlow-Townes noise of the first Stokes line is not expected to be a significant component of noise in the photomix generated carrier wave. Indeed, the good agreement between the measurement values and calculation in the inset of figure 6.2 shows that the phase noise of the Brillouin microwave signal is mainly contributed by the Schawlow-Townes noise of the third Stokes line. As a general comment relevant to the discussion of phase noise in the introduction, the results in figure 6.2 confirm that the very high Q factor of the Brillouin laser (high storage time) leads to the low microwave phase noise upon photomixing of the Stokes laser lines. Ultimately, the cascade process sets the limit of phase noise in these devices (see section 6.4). Finally, at low offset frequencies in figure 6.2, the phase noise exhibits a non-Schawlow-Townes component. While Brillouin lasers suppress technical phase noise from the pump [8, 15], it is possible that this noise is contributed by the pump. It is also possible that this noise is environmental related. The closed-loop control described in the next section suppresses this noise.

6.4 Cascade and Phase Noise in a Brillouin Microwave Oscillator

For cascaded Stimulated Brillouin lasers, the Nth Stokes wave is excited once the intra-cavity circulating power of the *N-1*th Stokes wave reaches the threshold excitation level. It has been shown that the excitation of the Nth Stokes wave will cause the intracavity power of the textitN-1th Stoke wave to be clamped [8] on account of gain clamping. For microwave generation by heterodyne mixing of the first and third Stokes waves, the operation described in the main text is to achieve maximum output power of the third Stokes wave just before threshold excitation of the fourth Stokes wave. It can be shown that the Schawlow-Townes frequency noise of a third Stokes wave at the threshold of excitation of the fourth Stokes wave is

$$S_\nu(f) = \frac{\hbar\omega g_c[n_T + N_T + 1]}{4\pi^2} \approx \frac{g_c kT\omega}{4\pi^2\Omega_B} = \frac{g_c kT}{4\pi^2}\frac{c}{2nV_A}, \tag{6.2}$$

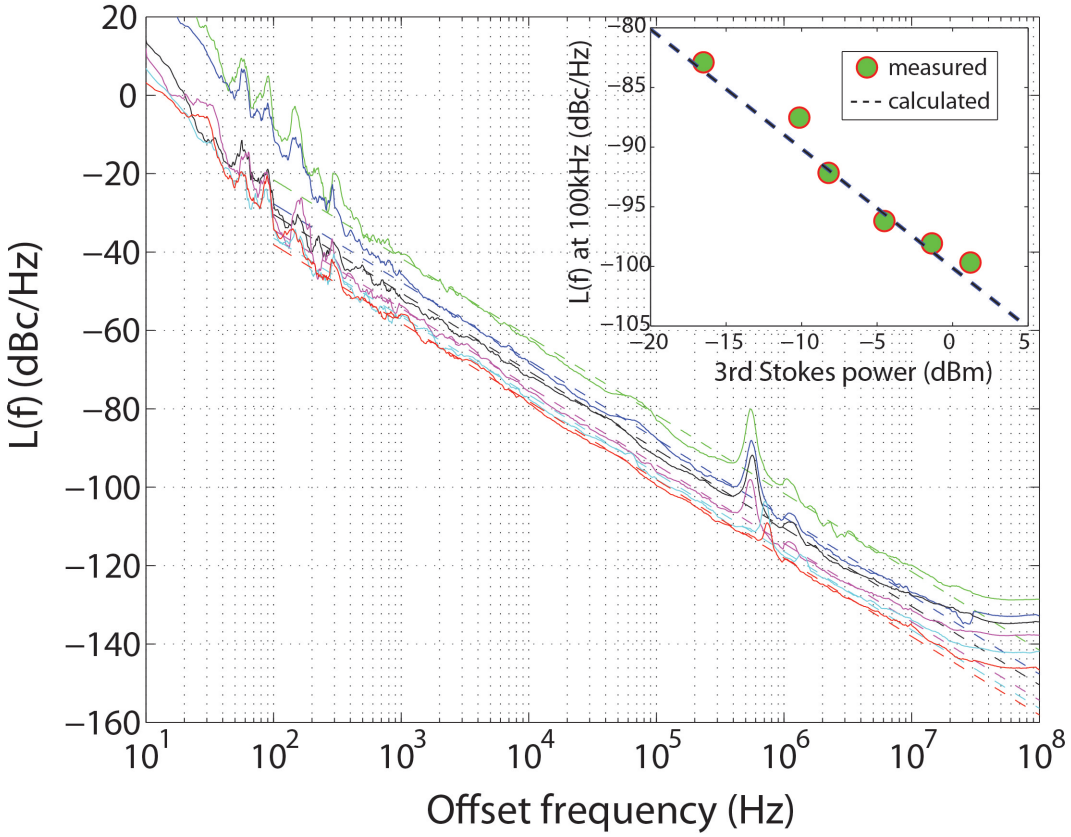

Figure 6.2: **Dependence of the single-sideband phase noise of the microwave oscillator at 21.7 GHz on the output optical power of the Brillouin laser.** The microwave signal is produced by photomixing the first and third Stokes lines on a high-speed detector. The output optical power of the third Stokes line is increasing from top to bottom curves (-16.5, -10.2, -8.2, -4.5, -1.4 and 1.2 dBm, respectively). The phase noise shows $1/f^2$ dependences for 5 decades from 200 Hz to 20 MHz. The dashed lines are $1/f^2$ fits to the measured phase noise spectra. Inset: plot showing inverse power dependence of the phase noise of the Brillouin microwave signal (100 kHz offset frequency) on the optical power of the third Stokes line. Circles: measured values; dashed line: calculated values based upon the Schawlow-Townes formula.

where n_T (N_T) is the number of thermal quanta in the mechanical (optical) field. At room temperature, N_T is negligible and $n_T \gg 1$, which gives the approximate form in the last two expressions in equation (6.2). ω (Ω_B) is the angular frequency for the optical (mechanical) field, and $\frac{\omega}{\Omega_B} = \frac{c}{2nV_A}$. g_c is the microcavity Brillouin gain and is related to the bulk Brillouin gain parameter g_0 by $g_c = \frac{c^2 g_0}{n^2 V_{eff}(1+\frac{4\Delta\Omega^2}{\Gamma^2})}$ (Lorentzian Brillouin gain spectrum). V_{eff} is the effective mode volume, Γ is the Brillouin phonon damping rate, and $\Delta\Omega$ is the offset of the cavity FSR relative to the Brillouin phonon frequency Ω_B. It can be seen from equation (6.2) that the noise limit is independent of both the pump frequency and the phonon frequency. Assuming that cascade is not inhibited, equation (6.2) sets a limit of the $1/f^2$ phase noise of the Brillouin oscillator upon photomixing the first and the third Stokes lines. From equation (6.2) and the volume dependence of g_c, it can be seen that a larger effective mode volume will help reduce the microcavity Brillouin gain parameter g_c and also reduce the Schawlow-Townes limit of the Brillouin oscillator. Moreover, operation at cryogenic temperatures would lower this noise limit as well through reduction of the phonon thermal quanta. The incident pump power at which the cascade transitions from the third to fourth Stokes oscillation is given by the following form:

$$P_{th} = \frac{27\pi^2 n^2 V_{eff}}{\tilde{g_0} Q_T^2 \lambda^2}, \tag{6.3}$$

where $\tilde{g_0} \equiv \frac{g_0}{1+\frac{4\Delta\Omega^2}{\Gamma^2}}$, and Q_T is the loaded Q factor of the cavity. Therefore, in systems wherein the phase noise is limited by cascade the high optical Q enables attainment of this noise limit at low pump power levels.

6.5 Phase-locked Operation of Oscillator

The Brillouin microwave oscillator can be operated in two distinct ways: open-loop (no feedback control) and closed-loop (phase-lock-loop control). In open-loop operation, the first and third Stokes lines from the resonator are directly photomixed on a fast photodetector with no other control. This is the method used for the spectra in figure 6.2. Alternatively, the center frequency of the free-running Brillouin microwave oscillator can be finely varied in the range of 100s kHz to a few MHz, by adjusting the pump laser frequency through either a piezo control of the pump laser cavity, or with an external acousto-optic modulator (AOM). Thus the Brillouin oscillator constitutes a voltage-controlled oscillator (VCO) and the device can be configured into a phase-lock-loop control design (i.e., closed loop operation). Phase-lock-loop control of optically generated microwave tones has been previously accomplished by reference to a high-performance microwave reference [134–136]. In these earlier works the objective was to use the the high stability microwave electrical reference to stabilize the optical generated tone. In the present case, the original microwave tone from the open

loop SBS oscillator is already of sufficient stability at shorter times (higher offset frequencies) so that the PLL is used only to obtain longer-term stability. Moreover, the loop control does not use another microwave oscillator to achieve stability, but rather a low frequency quartz oscillator via electrical frequency division. Indeed, the divider used here not only allows stabilization using a low-frequency reference oscillator, but also converts the SBS microwave signal into nearly any microwave signal frequency less than 21.8 GHz. As a result, this device constitutes a microwave synthesizer with performance comparable to good commercial electrical synthesizers. The essential elements of the SBS microwave synthesizer are shown in the experimental schematic of figure 6.3. The synthesizer is analyzed by a phase noise analyzer (PNA) and an Allan deviation tester (ADEV) and a mutual time base is shared between the frequency reference, phase noise analyzer and the Allan deviation tester.

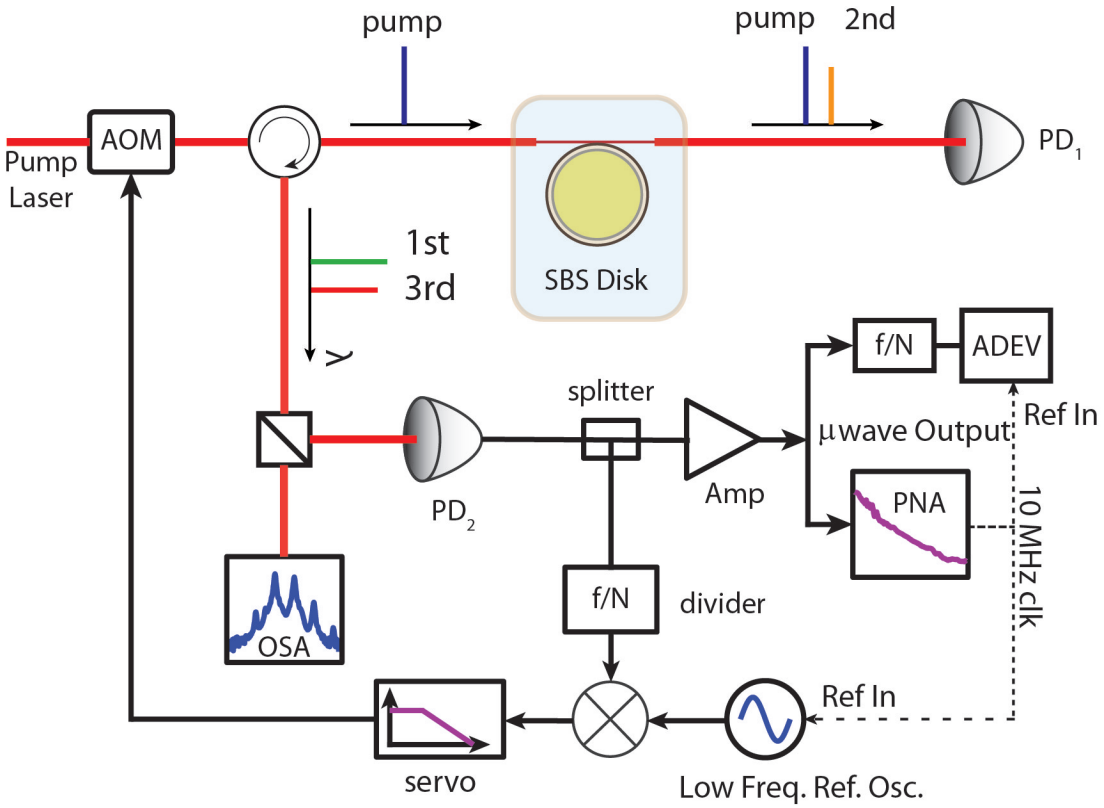

Figure 6.3: **Experimental schematic for the closed-loop Brillouin microwave oscillator.** AOM: Acouto-optic modulator; PD: photodetector; PNA: phase noise analyzer; ADEV: Allan Deviation tester; f/N: frequency divider. A mutual time base is shared between the phase noise analyzer, low-frequency reference oscillator and the ADEV tester.

The optical spectrum of the generated Stokes lines in the back-propagating direction is shown in figure 6.5a and includes the first and third Stokes lines that are used to generate the microwave tone of the present work. The incident optical power levels of the first and third Stokes lines on the high speed photodiode are 3.7 mW and 1.7 mW (the coupled optical pump power to the microresonator

was 31 mW). For comparison purposes, the open and closed loop phase noise spectra are presented in figure 6.4 together with the scaled-up phase noise of the low-frequency reference oscillator. Phase noise levels (open loop) of -90 dBc/Hz at 10 kHz offset and -110 dBc/Hz at 100 kHz are obtained for the 21.7 GHz carrier. The measured white phase noise floor of the oscillator (-156 dBc/Hz above 100 MHz) is a record for a microcavity-based microwave source by several orders of magnitude [47, 52, 58, 75, 116]. The calculated shot noise floor is -158 dBc/Hz for the 21.7 GHz carrier with 2.2 mA average photocurrent and a generated RF power of -15.5 dBm and is in good agreement with the measured result. Using another device, both a higher RF power of 2.9 dBm (1.9 mW, no optical or RF amplification) and yet lower white phase noise floor of -160 dBc/Hz were obtained. These results are within 19 dB of the very lowest white phase noise floors recently demonstrated using high-performance frequency combs and high-power photodiodes [76]. Further details on this measurement as well as the power calculations themselves are provided in the section 6.6.

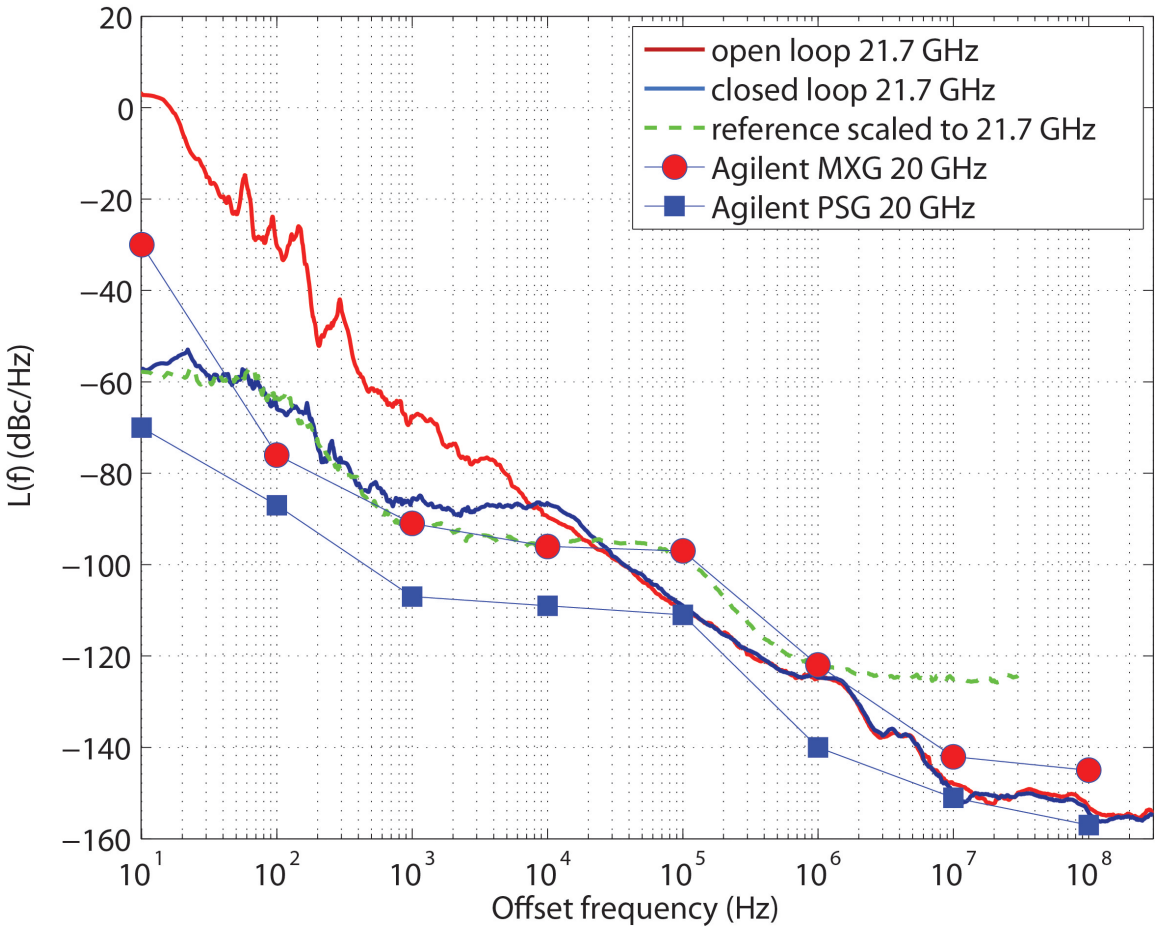

Figure 6.4: **SSB phase noise of open loop and closed loop Brillouin VCO.** The green dashed line is the phase noise of the reference oscillator scaled up to 21.7 GHz. Also plotted are the phase noise levels of the Agilent MXG signal generator (red circular markers) and PSG signal generator (blue square markers) at 20 GHz.

For closed-loop operation, an integer frequency divider (1/32) is used to divide the free-running microwave carrier to 678 MHz for phase comparision with a low-frequency reference oscillator at 678 MHz. The blue curve in figure 6.4 shows the phase noise of the closed-loop Brillouin oscillator. The close-to-carrier phase noise is now greatly reduced. The phase noise of the frequency reference is also shown in figure 6.4 as the green-dashed line. A factor of 20×log32=30 dB has been added to this line to account for phase noise scaling with frequency and thereby enable comparison with the phase noise of the closed-loop oscillator. As expected, for low offset frequencies the closed-loop oscillator tracks the scaled-up reference noise. The corresponding RF spectra for the open-loop (span 200kHz and resolution bandwidth 100 Hz) and closed-loop (span 200 Hz and resolution bandwidth 1 Hz) oscillators are given in figure 6.5b and figure 6.5c. In order to characterize the long-term frequency stability of the Brillouin oscillator, Allan deviation (ADEV) measurements were carried out for open-loop and closed-loop operation using gate times from 1 ms to 400 seconds. The measurement results are shown in figure 6.5d. For these measurements a subharmonic (1/256) at 84.6 MHz of the Brillouin oscillator is measured, as the maximum input frequency of the ADEV tester is 400 MHz. It can be seen that the long-term drift of the open-loop VCO is greatly suppressed. More than 80 dB reduction of the ADEV (wrt to the 10 MHz mutual timing base) is obtained at 400 seconds gate time. Also, a residual Allan Deviation of 5×10^{-13} is achieved at 1 second. Overall, the closed-loop Brillouin oscillator has low-phase noise at both close-to-carrier and high offset frequencies. In fact, the phase noise level demonstrated here is between a mid-range (Agilent N5183A MXG, phase noise of -97 dBc/Hz at 100 kHz offset for 20 GHz carrier) and high-performance (Agilent E8257D PSG, phase noise of -111 dBc/Hz at 100 kHz offset for 20 GHz carrier) commercial electrical microwave synthesizers. The phase noise levels of the Agilent MXG and PSG signal generators at different offset frequencies for 20 GHz carrier are plotted in figure 6.4 as well.

6.6 High-RF-power, Low White-phase-noise of the Brillouin Microwave Oscillator

High incident power to the fast photodetector means high RF power without amplification, and also a lower shot-noise-limited white phase noise floor. Higher RF power directly from the photodetecter also makes the interconnection of the microwave Brillouin oscillator to the other RF components (e.g., the frequency divider) more convenient since it avoids the requirement of a microwave amplifier. Considering the heterodyne beating of two lasers with power P_1 and P_2, onto a photodetector with responsivity R_s and load impedance R_L, the RF power is given as $P_{RF} = 2R_s^2 P_1 P_2 R_L$. The shot-noise-limited phase noise floor is given as $L(f) = 10log\left(\frac{qR_s(P_1+P2)R_L}{P_{RF}}\right)$. In the experiment, power levels as high as 11.8mW and 4.4mW for the first and third Stoke lines were delivered to the fast photodetector (PD). The generated average photocurrent was 10.66 mA, with a photodetector

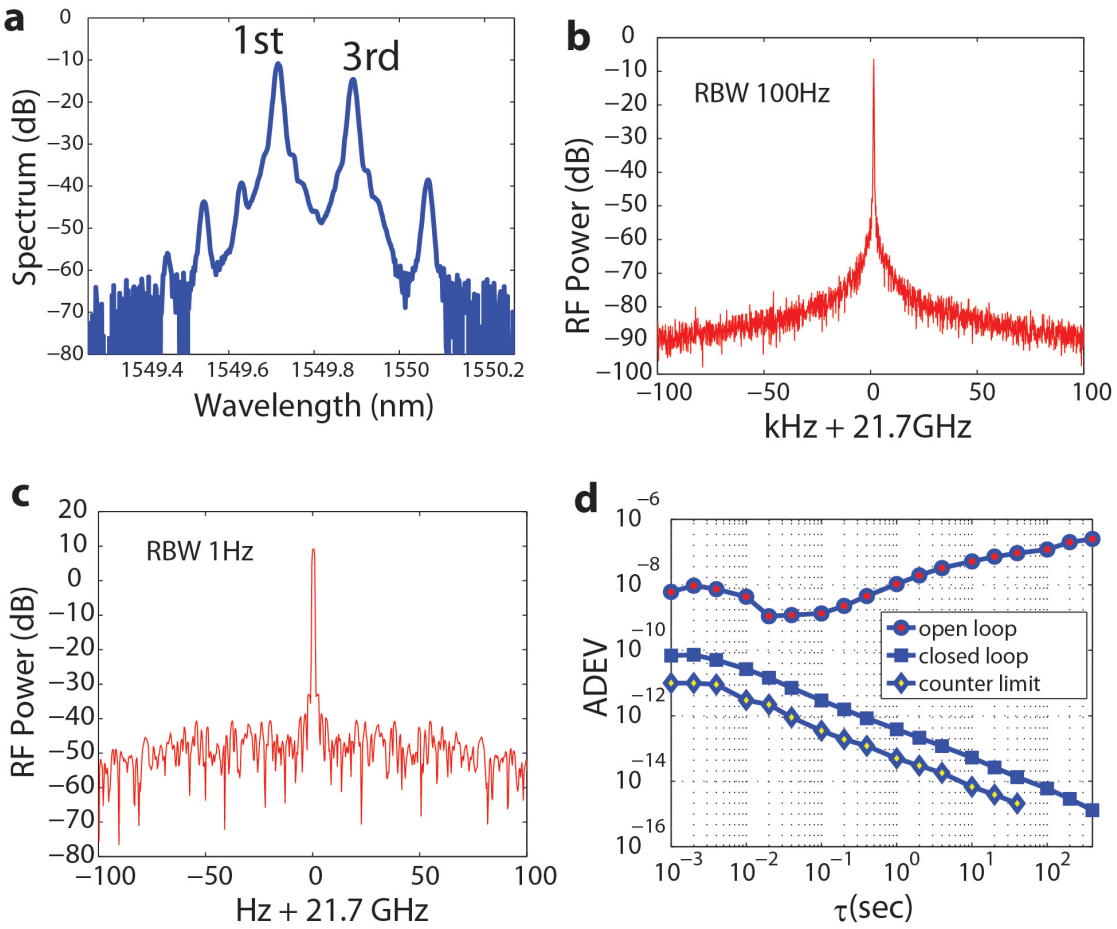

Figure 6.5: **Optical,RF spectra, and ADEV of Brillouin VCO. a,** Optical spectrum of the first-Stokes and third-Stokes laser emission lines. The pump wave is also visible, but is weak on account of propagation opposite to the direction of the first and third Stokes lines. Also visible is the 5th Stokes line in the spectrum as well as the first anti-Stokes wave. **b,** RF spectrum of an open-loop Brillouin oscillator at 21.7 GHz. The span is 200 kHz and the RBW is 100 Hz. **c,** RF spectrum of a closed-loop Brillouin oscillator at 21.7 GHz. The span is reduced to 200 Hz and the RBW is 1 Hz. **d,** Allan deviation of the Brillouin microwave oscillator. Circle markers represent the open-loop operation, square markers represents the residual Allan deviation for the close-loop operation and the diamond markers give the counter limit.

responsivity of 0.65 A/W. The microwave power measured at the RF spectrum analyzer was -1.38 dBm as shown in the inset of figure 6.6. Taking into account about 4.3 dB loss of the RF coax cable and DC block, the microwave power generated directly at the PD is 2.9 dBm (1.9 mW). It is important to note that this number is over 20 dB larger than what has been possible using microcombs [47, 52, 58, 75, 116]. For comparison, the calculated RF power is 3.4 dBm and the calculated shot-noise-limited white phase noise floor is -163 dBc/Hz. In the measurement, the white phase noise floor shown in figure 6.6 is -160 dBc/Hz for offsets above 200 MHz, which is close to the calculated value. (Note: the instrument white phase noise floor is lower than -164 dBc/Hz.) In summary, a record-high, RF power and low phase noise floor for a microresonator-based microwave source has been demonstrated.

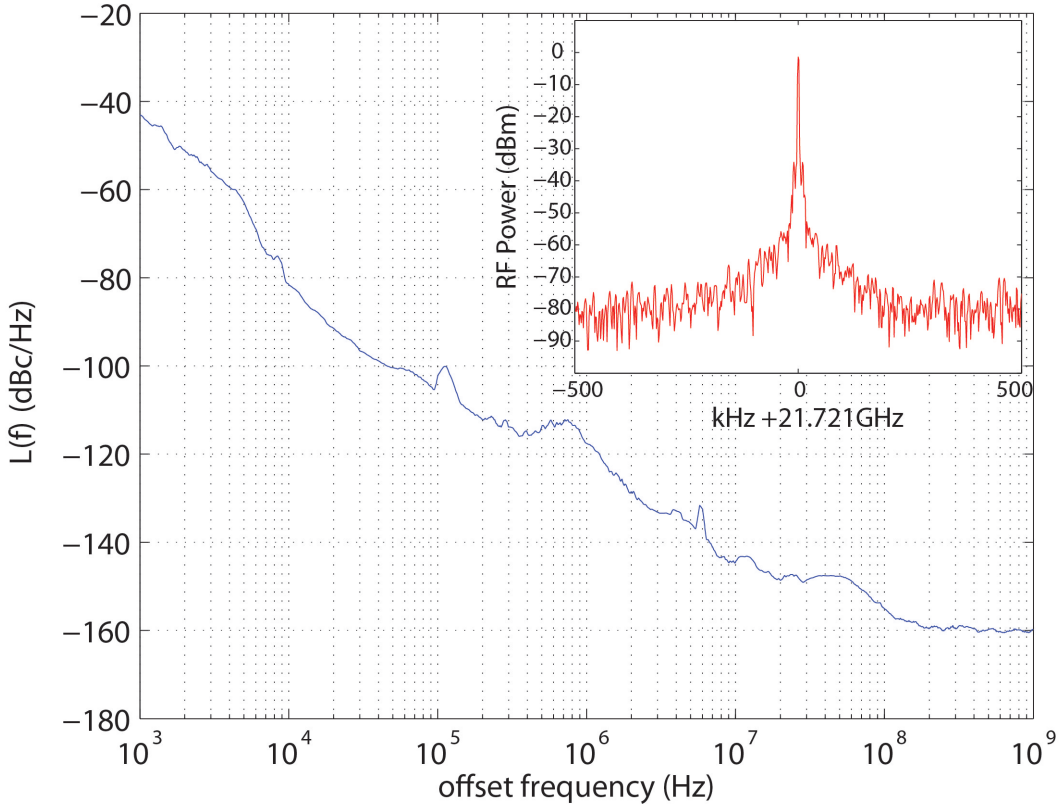

Figure 6.6: **High RF power of the Brillouin Microwave Oscillator.** Main panel: Single-sideband phase noise of a high-power open-loop Brillouin oscillator. A record low white phase noise floor (-160 dBc/Hz) for a microcavity-based microwave source is achieved for offset frequencies greater than 200 MHz. Inset: RF spectrum of an open-loop Brillouin oscillator measured directly from a high-speed photodetector without any amplification.

6.7 Frequency Synthesizer Operation

RF frequency synthesis derived from the low-noise closed-loop Brillouin oscillator was also demonstrated. This is done by using a (fractional or integer) frequency divider to divide the closed-loop Brillouin oscillator at 21.7 GHz to different frequencies. A series of the phase noise spectra using different division ratios (f/N, N=32, 256, 512, 1024, 2048) is shown in figure 6.7a. Generally, the single-sideband phase noise $L(f)$ will drop 20log$N$ dB upon frequency division. Thus RF frequency synthesis at arbitrary frequencies up to 22 GHz is possible based on the low-noise K-band Brillouin oscillator. The time-domain traces are shown in figure 6.7b for 2.7 GHz, 1.35 GHz and 678MHz, measured using an oscilloscope with 4 GHz bandwidth.

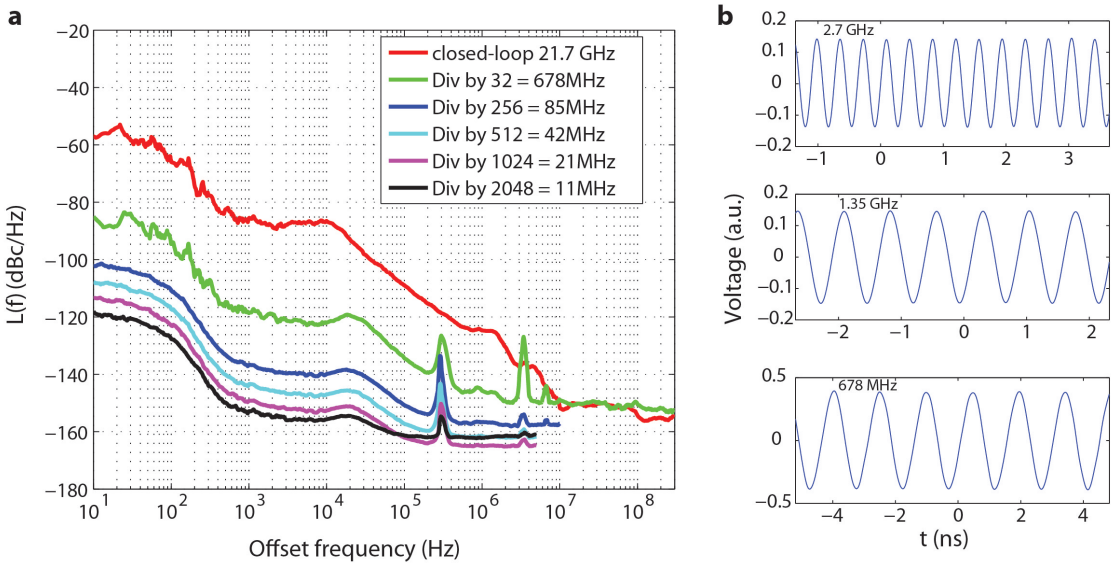

Figure 6.7: **RF Frequency synthesis by the K-band low-noise Brillouin microwave oscillator. a,** Phase noise of a series of RF frequencies generated by the synthesizer. **b,** Typical sine-wave, time-domain traces of the synthesizer output at 2.7 GHz, 1.35 GHz and 678 MHz (from top to bottom). All frequencies lower than the base oscillator frequency of 21.7 GHz are possible and the traces selected here were limited by the bandwidth of oscilloscope (4 GHz).

6.8 Out-of-loop Allan Deviation

Finally, closed-loop operation of the Brillouin oscillator was also possible by referencing to a fixed-frequency, ultra-low-noise Oven-Controlled Crystal Oscillator (OCXO) at 400 MHz. Figure 6.8 shows the Allan Deviation ($\sigma(\tau)$) measurements of the Brillouin microwave oscillator using this reference. The blue square markers are the residual ADEV of the Brillouin microwave oscillator with regard to the reference OCXO. For a more rigorous measurement, we also measure the out-of-loop Allan

Deviation of the closed-loop VCO using a second independent ultra-low-noise OCXO (10 MHz). The green diamond markers are the out-of-loop ADEV and the red circle markers are the ADEV of the reference OCXO at 400 MHz measured against the second OCXO at 10 MHz. The out-of-loop ADEV tracks the 400 MHz reference for $\tau > 0.03$ s. Thus the out-of-loop ADEV is reference limited and an out-of-loop ADEV level of 5×10^{-12} at 1 second gate time is demonstrated.

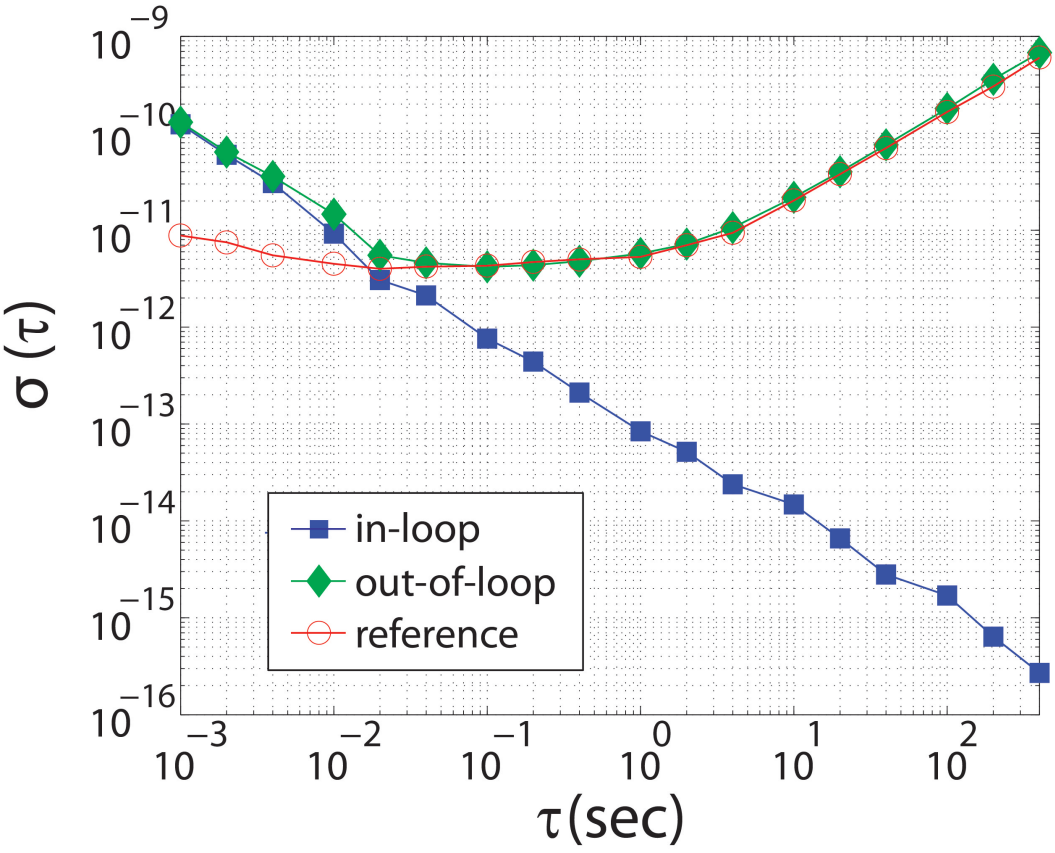

Figure 6.8: **Out-of-loop Allan deviation.** Allan deviation ($\sigma(\tau)$) measurements of the Brillouin microwave oscillator using an ultra-low-noise Oven-Controlled Crystal Oscillator (OCXO) at 400 MHz as reference. The blue square markers are the residual ADEV of the Brillouin microwave oscillator with regard to the reference OCXO. The green diamond markers are the out-of-loop ADEV, measured against a second low-noise OCXO at 10 MHz. The red circle markers are the ADEV of the reference OCXO at 400 MHz measured against the second OCXO at 10 MHz.

6.9 Discussion

In this work, we have demonstrated a microwave synthesizer with commercial-level frequency stability using a compact, on-chip Brillouin laser VCO. The combined demonstrations show that the Brillouin VCO can operate as a direct replacement for conventional electronic VCO devices. Significantly, the phase noise of the Brillouin VCO does not degrade with increasing frequency as compared

to electronic devices. This is because the phase noise contributed by the underlying Stokes lines (assuming constant power in each line) is not sensitive to order or to pump frequency. Also, by operating the Brillouin at shorter pump wavelengths or by operating on higher-order Stokes lines, the base frequency of the synthesizer can be readily boosted. For example, by operation with a green pump (doubled YAG), the base frequency would be boosted to beyond 60 GHz using the same Stokes 1 to Stokes 3 photomixing configuration demonstrated here (again with no degradation in phase noise performance). Also, by operation on the 1-5 or 1-7 Stokes combinations, millimeter-wave generation well beyond 100 GHz is feasible. Likewise, electronic dividers have been demonstrated to these frequencies [137], thereby making the possibility of high-performance millimeter-wave synthesizers possible using this approach. It is important to note that such millimeter-wave synthesizers would be predicted to produce X-band signals with significantly lower phase noise than what has even been demonstrated here. This is because the divider process quadratically improves the phase noise. For example, by only maintaining the Schawlow-Townes noise at shorter pump wavelengths, the predicted X-band (10 GHz) phase noise level would be -130 dBc/Hz at 100 kHz offset upon division of a 90 GHz SBS-generated base frequency. Ultimately, the current limit to phase noise in these devices is the onset of cascade to higher-order Stokes lines. If this process could be forestalled through, for example, judicious cavity dispersion control, then much lower phase noise levels than what has been demonstrated here are possible.

Chapter 7

Other Experiments

7.1 Thermorefractive and Thermal Mechanical Noise of Microcavities

High-Finesse Fabry-Perot optical cavities made of ultralow expansion (ULE) material are used as reference cavities for laser frequency stabilization to sub-Hertz level linewidth [82]. A recent advance in ultra stable optical reference cavities is a silicon single-crystal optical cavity with demonstrated fractional stability of 1×10^{-16} at short timescales and a stabilized laser linewidth of sub-40 mHz [138]. Compact WGM optical cavities, are also good reference cavities due to their ultrahigh Q-factor, small footprint and robust configuration [139–142]. For both the Fabry-Perot and WGM optical cavities, the ultimate frequency stability is limited by thermal noise-induced cavity length or refractive index fluctuations [139, 143].

The thermal dynamical fluctuations of the temperature of the cavity medium at thermal equilibrium state is given by [144],

$$\langle \delta T^2 \rangle = \frac{k_B T^2}{\rho c_p V}, \tag{7.1}$$

where k_B is the Boltzman constant, T is the temperature at equilibrium, V is the effective mode volume, c_p is the specific heat capacity. The temperature fluctuations will lead to the refractive index fluctuations of the cavity medium, thus cause the fluctuations of the cavity resonance frequency, which is called thermorefractive noise:

$$\left| \frac{\delta\omega}{\omega} \right| = \left| \frac{\delta n}{n} \right| = \left| \frac{1}{n} \frac{\mathrm{d}n}{\mathrm{d}T} \delta T \right|. \tag{7.2}$$

The power spectrum density of the thermorefractive noise of a microcavity can be derived by introducing fluctuating thermal sources in the heat diffusion equation in analogous to the Langevin

approach [139]. An approximate analytic expression is derived for a silica microsphere cavity [139],

$$S_{\delta\omega/\omega}(\Omega) \approx \frac{k_B T^2 D}{\pi^{5/2} n^2 \rho c_p R} \frac{2}{\sqrt{d^2 - b^2}} \left(\frac{\mathrm{d}n}{\mathrm{d}T}\right)^2 \int_0^\infty \frac{q^2 e^{-q^2 b^2/2}}{D^2 q^4 + \Omega^2} \frac{\mathrm{d}q}{2\pi}, \tag{7.3}$$

where R is the resonator radius, d and b are the dimensions of the mode across section, and D is the thermal diffusivity of silica.

The presence of the thermorefractive noise in microcavities is the practical limit of the frequency stabilities when use microcavities as reference cavities. It also sets the background level for the displacement sensitivity when ultilizing the thermal Brownian motion of microcavities for displacement sensing and monitoring [145]. From equation (7.3), we can see that the thermorefactive noise is approximately inverse proportional to the cavity mode volume. Also by operating at a flat temperature coefficient region where $\alpha \equiv (1/n)(\mathrm{d}n/\mathrm{d}T)$ is small, the thermorefractive noise can be reduced.

The measurement of the the thermorefractive noise is based on a frequency locking technique using the Hänsch-Couillaud approach [95, 96]. An narrow linewidth fiber laser was used as the probe laser and is locked to the cavity resonance. The Hänsch-Couillaud error signal provides the frequency discrimination to transfer the cavity frequency fluctuations to output intensity fluctuations, while rejecting laser intensity fluctuations when the laser is locked at the cavity line center. The laser frequency noise will also be discriminated by the Hänsch-Couillaud error signal thus it sets a limit of the measurement sensitivity of cavity frequency noise. The spectra of the the thermorefractive noise for the planar silica disk resonators with three different diameter (0.3, 0.4, and 1 mm) are given in figure 7.1. In each subfigure, the blue curve is the measured frequency fluctuation spectrum of the disk resonator, the green curve is the frequency noise of the probe fiber laser, and the red curve is the measurement background noise when the laser is off-resonance. The red curve is determined by the detector thermal (Johnson) noise and photon shot noise. And its rise with the increase of Fourier frequencies is due to the calculated reduced cavity transfer function when the Fourier frequency is beyond the cavity linewidth. The measured cavity frequency noise generally rises with the decrease of the Fourier frequencies. This part of the broadband noise at low Fourier frequencies is the thermorefractive noise. In figure 7.1a, there is also a black curve, which is the calculated thermorefractive noise with fitted diameters b and d from equation (7.3). It can be seen that the measured cavity frequency noise is in good agreement with the calculated thermorefractive noise at low Fourier (offset) frequencies less than 2 MHz. Finally, it can be seen that a reduced cavity thermorefractive noise comes with the increase of the cavity size.

The thermal Brownian motion (thermal mechanical noise) of the disk microresonators are also visible in the cavity frequency noise spectra in figure 7.1. They are the multiple peaks with Lorentzian shape in the measured frequency noise curves. These mechanical modes are the research objects in the field of cavity optomechanics [3], where optical forces can be used to cool or amplify the motion

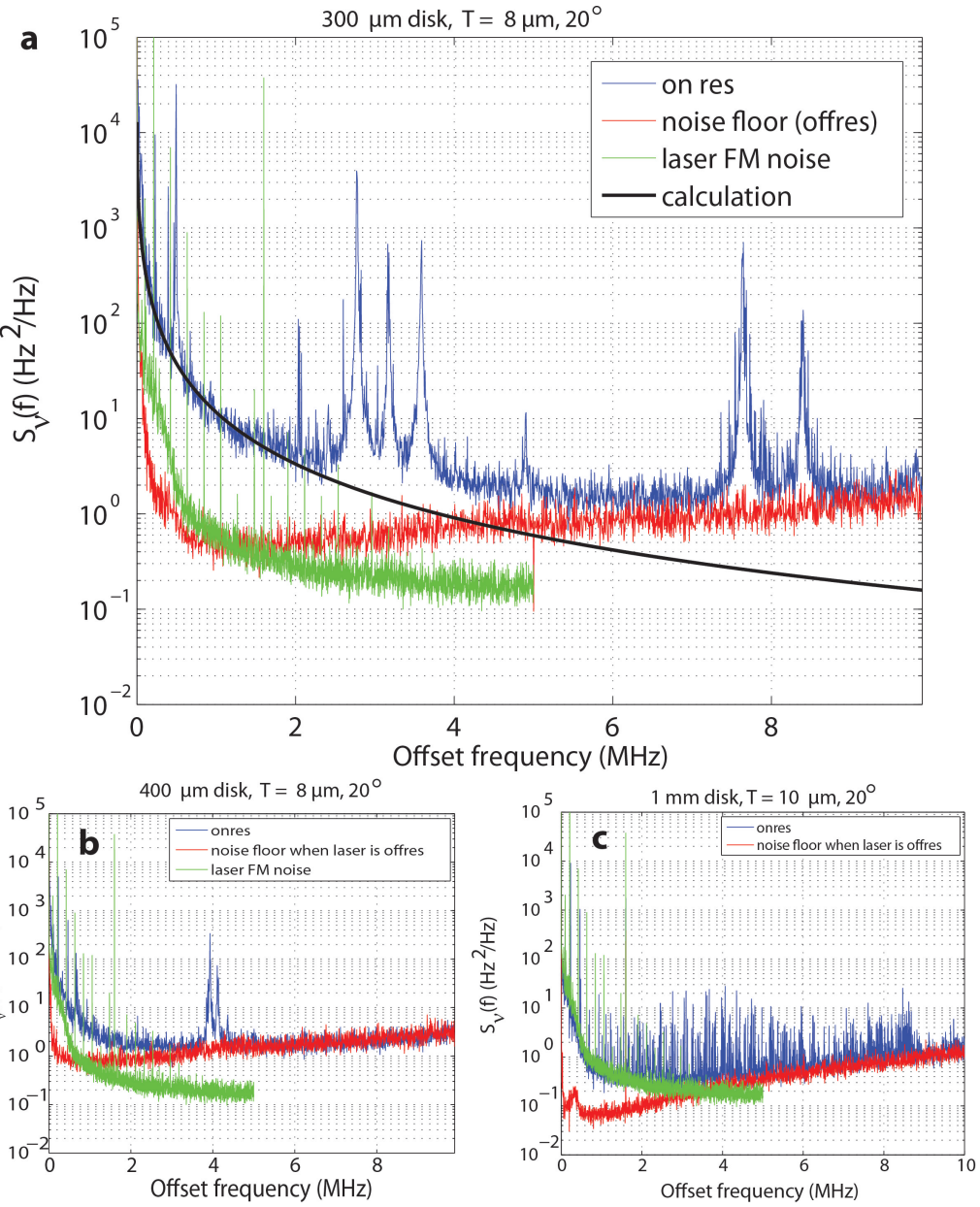

Figure 7.1: **Thermorefractive and thermal mechanical noise of microresonators.** (a) The blue curve is the measured frequency fluctuation spectrum of the disk resonator (Diameter 300 μm), the black curve is the calculated thermorefractive noise. The green curve is the frequency noise of the probe laser, and the red curve is the measurement background noise when the laser is off-resonance. The multiple peaks in the blue curve is the thermo Brownian motion of the disk resonator. (b) Measurement of the frequency noise spectrum of a 400 μm disk resonator. (c) Frequency noise spectrum of a 1 mm disk resonator. The low-frequency thermorefractive noise is not detected because the sensitivity is limited by the frequency noise of the probe laser. However, a dense spectrum of the thermo-mechanical peaks are shown.

of a mechanical mode.

7.2 Microcavities as Frequency References

As discussed in section 7.1, the thermorefractive noise of the microresonators decreases approximately inverse proportional to cavity mode volume. The resonator sizes of the planar silica disk resonators have been demonstrated to be as high as 25 mm. Thus the large-sized disk resonators are good candidates to be used as chip-based frequency references for laser frequency stabilization.

In this experiment, two disk resonators with diameter 15 mm were used as frequency reference cavities for laser frequency stabilization of two independent lasers. The lasers used in this study are one external-cavity-diode-laser (ECDL) and one narrow linewidth fiber laser (Koheras). Note that the ECDL has much higher frequency noise than the fiber laser. The heterodyne beat of the two lasers were analyzed by a phase noise analyzer (PNA). When the ECDL and fiber laser are free running, the jitter noise of the beat signal (mainly from the ECDL) prohibits a stable measurement of the phase noise by the PNA. Therefore, the ECDL were prestabilized to a Mach-Zehnder Interferometer to reduce the jitter noise by a loose lock. This enables a successful stable measurement of the single-sideband (SSB) phase noise of the beat note by mixing the ECDL and fiber laser, without final stabilization to the two disk resonators. The measured SSB phase noise spectrum is given in figure 7.2 (red curve). The SSB phase noise when the two lasers were both stablized to the two disk resonators is plotted in figure 7.2 as well (blue curve). A 10–20 dB reduction of the SSB phase noise was obtained for offset from 100 Hz to 100 kHz. Particularly, a phase noise level of -40 dBc/Hz at 1 kHz offset was obtained.

7.3 Cavity Optomechanics with Microdisk Resonators

Cavity optomechanics studies the cavity-enhanced radiation pressure interaction between light (photons in a cavity) with a mechanical oscillator at mesoscale [3, 146]. Depending on whether the laser is blue or red detuned from the cavity resonance, the unbalanced energy transfer between the scattered Stokes and anti-Stokes waves caused by the mechanical motion of the cavity will lead to the amplification or cooling of the mechanical motion. For the amplification part, once the amplification gain or the parametric instability overcomes the intrinsic loss of mechanical mode, it results in a self-sustaining, regenerative oscillation of the mechanical mode in an optical cavity [147, 148]. Furthermore, phonon laser oscillation in a compound microcavity two-level system has been demonstrated [102]. For the cooling part, unresolved and resolved sideband cooling have been demonstrated [96, 149]. And recently, the cooling of a nanomechanical oscillator to its quantum ground state has been achieved [150, 151]. Also the quantum motion of a nanomechanical resonator has been observed

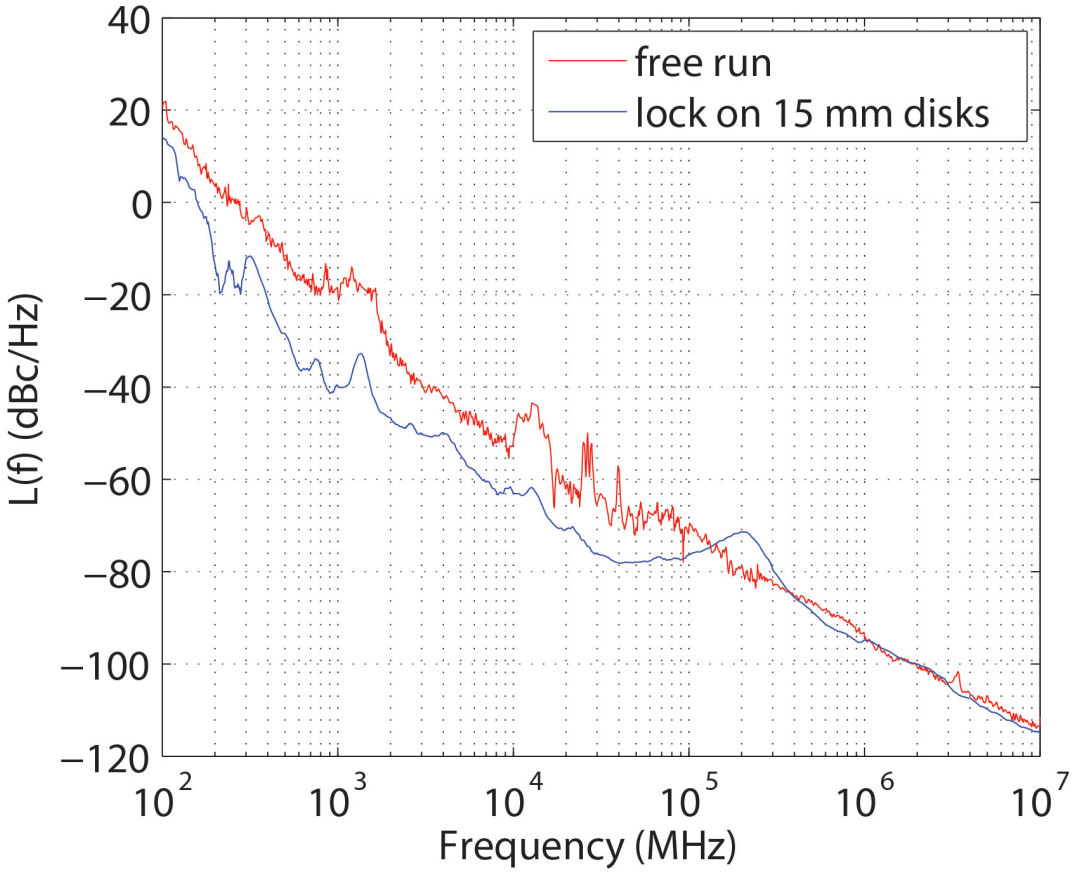

Figure 7.2: **Microcavities as frequency references.** An external-cavity-diode-laser (ECDL) and a narrow linewidth fiber laser (Koheras) were locked (frequency stabilized) to two independent disk resonators with diameter 15 mm separately. (The ECDL was prestabilized to a Mach-Zehnder Interferometer before locked to the 15 mm disk resonator). The heterodyne beat of the two lasers with/without frequency stabilization were analyzed by a phase noise analyzer (PNA). The red curve is the free-running single-sideband (SSB) phase noise of the heterodyne beat signal. The blue curve is the SSB phase noise of the heterodyne beat signal when the ECDL and fiber laser locked to two 15 mm disk resonators. Phase noise reduction of 20 dB at 1 kHz offset was obtained.

while cooling the mechanical resonator to near its ground state by resolved sideband laser cooling [152].

Of all the parameters of a cavity optomechanical system (e.g., the photon decay rate κ, the phonon decay rate Γ_m, effective mass m_{eff}, mechanical frequency Ω_m, the optomechancal coupling rate g), the mechanical Q factor (or equivalently the phonon decay rate) is an important parameter. For the amplification side, the pump threshold for the optomechanical oscillation (or parameteric instability) is inversely proportional to the mechanical Q. Furthermore, the fundamental linewidth of the optomechanical oscillator decreases with the increase of the mechanial Q. For the cooling side, the mechanical Q affects how fast the reheating of the mechanical mode by the ambient thermal bath. Thus it determines a final effective temperature for the mechanical mode under laser cooling.

In this section, we report on an optomechanical oscillator with the highest mechanical Q in the air so far (to the best of our knowledge). Mechanical Q in the range from 25,000 to 80,000 was demonstrated with a planar silica disk resonator. Moreover, these optomechanical oscillators possesses low phase noise above threshold and is comparable to the best single MEMS oscillator. The linewidth narrowing effect of the mechanical mode below threshold was measured and was used to infer the cavity optomechanical coupling coefficient.

7.3.1 Ultralow-loss Optomechanical Oscillator on a Chip

The optomechanical resonator in this study is the planar silica-on-silicon microdisk resonators described in chapter 1. The optomechanical coupling, $g_{OM} \equiv \frac{\mathrm{d}\omega}{\mathrm{d}x} = -\omega/R$. Thus the optomechanical coupling strength decreases with the increase of the resonator diameter R. Here we measured the thermal mechanical spectrum of the microdisk resonators with small diamemters $\leq$ 500 μm. A tunable EDCL is used as the probe laser and coupled on the side of the cavity resonance. The Brownian motion of the resonator introduces a phase modulation of the intracavity field, and is transferred to intensity modulation on the cavity output when the probe laser is located on either side of the cavity's Lorentzian line shape. The cavity transmitted signal was detected using a photodetector with bandwidth 125 MHz and its spectrum was analyzed with a RF spectrum analyzer. In order to make sure that the radiation pressure amplification of the mechanical motion is negligible, the power of the probe laser is kept lower than 5% of the threshold for mechanical oscillation. All the measurement were performed at room temperature and with air pressure of 1 atm.

The measured mechanical mode spectra of the microdisk resonator with ultrahigh mechanical Q are given in figure 7.3, with corresponding Lorentzian fits (blue curves) to extract the linewidth and mechanical Q. Figure 7.3a-b show two high-Q mechanical modes from one microdisk (diameter 300 μm, wedge angle 20°, undercut 80 μm). One mode is at 16.5 MHz, with a 3 dB linwidth of 210 Hz and mechanical Q of 78,570. The other mode is at 26.0 MHz, with a 3 dB linwidth of 1059 Hz and mechanical Q of 24,800. Figure 7.3c shows a high Q (79,950) mechanical mode from a 400 μm disk

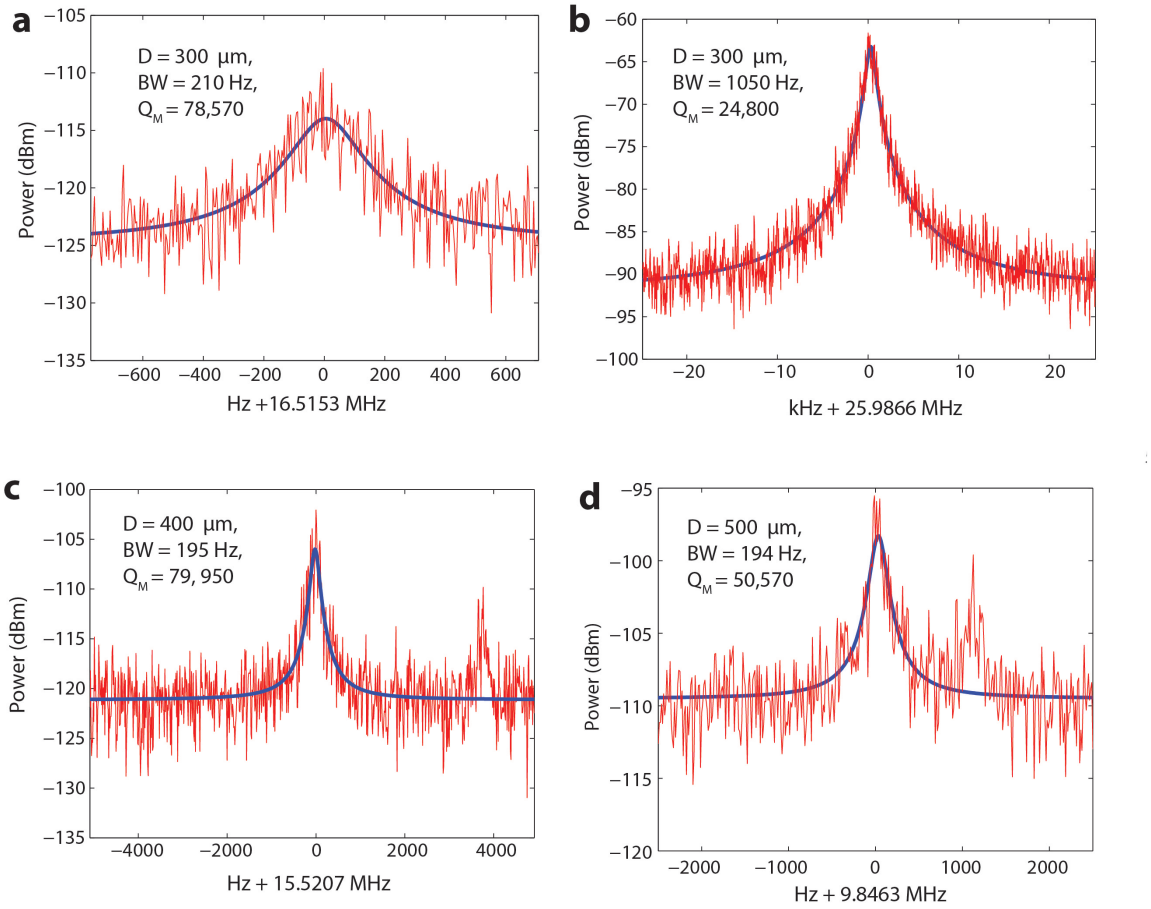

Figure 7.3: **Mechanical modes of microdisk resonators with ultrahigh mechanical Q in air.** The blue curves are the Lorentzian fits to extract the mechanical Q. (a) A high-Q (78,570) mechanical mode at 16.5 MHz. Resonator dimensions: D = 300 μm, wedge angle $\theta \approx 19°$, oxide thickness T = 8 μm, undercut C = 80 μm. (b) A high-Q (24,800) mechanical mode at 26.0 MHz. Resonator is the same as (a). (c) A high-Q (79,950) mechanical mode at 15.5 MHz. Resonator dimensions: D=400 μm, $\theta \approx 19°$, T = 8μm, C=70 μm. (d) A high-Q (50,741) mechanical mode at 9.8 MHz. Resonator dimensions: D = 500 μm, $\theta \approx 19°$, T = 10 μm, C = 65 μm.

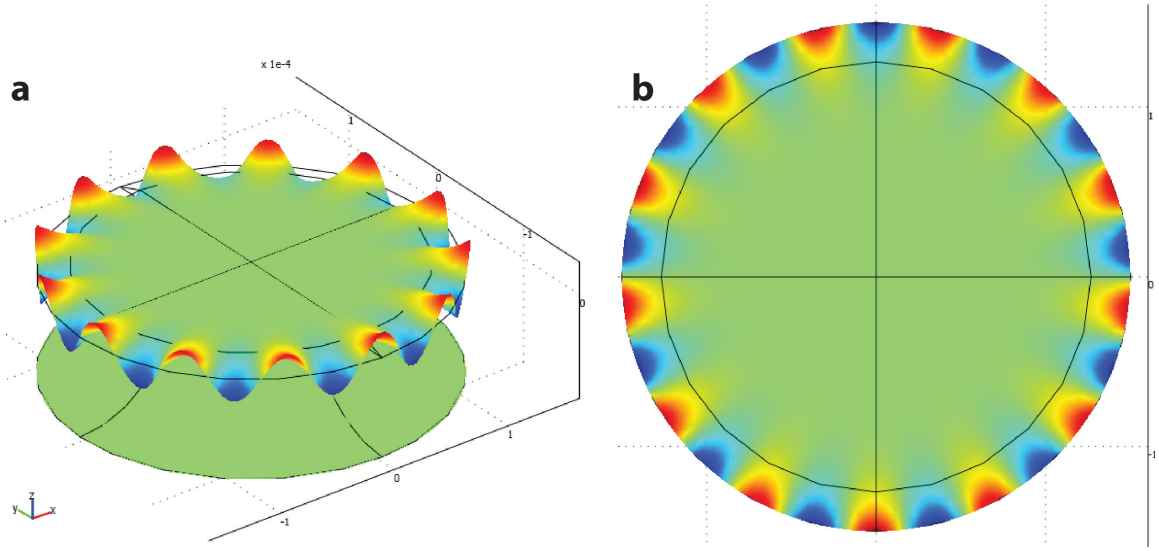

Figure 7.4: **FEM simulation of the "Crown" mechanical mode of the microdisk resoantor.** Disk dimension: D = 300 μm, $\theta = 19°$, T = 8 μm, and undercut C = 80 μm. The displacement of the crown modes is mainly along the z-axis. (a) 3-D view with deformed shape showing z-displacement. (b) 2-D top view showing z-displacement.

at 15.5 MHz, and figure 7.3d shows a high Q (50,570) mechanical mode from a 500 μm disk at 9.8 MHz.

From FEM simulation of the mechanical modes of the microdisk resonators, these ultrahigh-Q mechanical modes belong to the "crown" mode families. Figure 7.4 gives the simulated z-displacement of a 13th crown mode for a microdisk (D = 300 μm, $\theta = 19°$, T = 8μm, and undercut C = 80 μm). The simulated eigenfrequency of this mode is at 16.1 MHz and agrees with the measured mode shown in figure 7.3a. The displacement of these crown modes is mainly along the z-axis, and they form a wave-like, up-and-down shape along the rim of the microdisk resonator.

The measured Q factors (25,000–80,000) of these mechanical modes in air are one order of magnitude larger than what has been studied in microtoroid optomechancial oscillators in air. Ultralow-dissipation mechanical modes with Q-factors around 50,000 in low-pressure environment (p <1 mbar) were demonstrated in microtoroid resonators with low-clamping losses [153, 154]. However, the mechanical Q in these microtoroid cavities degrades to values lower than around 3000 in the air environment, due the viscous air damping.

In order to clarify the origins of the high mechanical Q-factors of micirodisk resoantors in the air, which is not observed in microtoroids, we consider different contributions to the mechanical damping rate in oscillators:

$$\Gamma_M^{tot} = \Gamma_M^{mat} + \Gamma_M^{clp} + \Gamma_M^{air}, \tag{7.4}$$

where Γ_M^{tot} is the total mechanical damping rate, Γ_M^{mat} is the dissipation caused by material loss, Γ_M^{clp} is the clamping loss (also called anchor loss), and Γ_M^{air} is the loss due to air damping. For Γ_M^{mat},

dissipations caused by two level systems [155] (which are common to amorphous materials) and anharmonicity [156] in reflowed silica gives a material-loss-limited mechanical Q of around 50,000 [153]. For the clamping loss term, dissipation is caused by phonon tunneling (or acoustic coupling) to the substrate. An approximate formula was given to calculate the clamping-loss-limited Q-factor in a microtoroid resonator [153],

$$Q_M^{clp} \approx 3\left(\frac{c\rho}{E_{mech}}\Omega_m \int_{A_p} |\Delta z(r)|^2 \mathrm{d}A\right)^{-1} \tag{7.5}$$

Where E_{mech} is the total energy stored in the mechanical mode, c is the speed of sound in silica, ρ is the density of silica, Ω_m is the angular eigenfrequency of the mode, and $\Delta z(r)$ is the z-displacment of oscillation at position r, with the integration area over the clamping area A_p. This formula with an empirical prefactor 3 was shown to give good estimate of the clamping loss of a microtoroid resonator [153].

For the air damping term, we can consider the power dissipation of an vibrating surface due to viscous damping by air [157],

$$P_{dis} = \iint_S \sqrt{\Omega_m \rho_a \eta/8}|v_\parallel|^2 \mathrm{d}S, \tag{7.6}$$

where ρ_a is the density of air, and η is the viscosity of air. The integration is taken over the surface area. Then the viscous-air-damping-limited Q is can be calculated as,

$$Q_M^{air} = \frac{\Omega_m \iiint_V \rho|v|^2 \mathrm{d}V}{P_{dis}} = \sqrt{\frac{8\Omega_m\rho^2}{\rho_a\eta}}\frac{\iiint_V |v|^2 \mathrm{d}V}{\iint_S |v_\parallel|^2 \mathrm{d}S}. \tag{7.7}$$

Equation (7.7) can be rewritten as

$$Q_M^{air} = F\left[\sqrt{\frac{8\Omega_m\rho^2}{\rho_a\eta}}\frac{\iiint_V |v|^2 \mathrm{d}V}{\iint_S |v|^2 \mathrm{d}S}\right]\beta \tag{7.8}$$

where $\beta \equiv \frac{\iint_S |v|^2 \mathrm{d}S}{\iint_S |v_\parallel|^2 \mathrm{d}S}$ is a normalized factor, indicating the overall ratio between the total velocity squared and the square of the parallel-to-surface component of the velocity. It can be viewed as an enhancement factor of Q_M^{air} due to the projection of velocity on any surface shapes over the cases where the vibration displacement is exactly parallel to the surface ($v = v_\parallel$). Here we introduce an empirical factor F to account for the measured mechanical Q value and the calculated Q value using equation (7.8), similar to the empirical factor used in equation (7.5).

Now let's first consider the clamping loss and air damping loss of the crown modes in microtoroid resonators. These crown modes [154] feature a local vibration of the torus region and small amount of vibration coupling to the anchor surface (contact plane between the silica layer and the silicon pillar), resulting a calculated clamping-loss-limited $Q_M^{clp} \sim 100,000$. However, because the vibration

of the torus is along the z-axis, and torus cross section is circular shape, it leads to an approximate β factor of 2. The calculated air-damping-limited Q_M^{air} using equation (7.8) is around 4000 and is consistent with the measured mechanical Q values of microtoids in the air [147, 153, 154].

For micordisk resonator, from the FEM simulation in figure 7.4, it can be seen that the displacement of the oscillation is confined along the edge of disk wedge region. Thus the phonon tunneling into the substrate is minimum. The calculated clamping-loss-limited Q_M^{clp} for the 13th crown mode in figure 7.4 is around 5 million, which is far greater than the measured value. For the air-damping loss, because of the small wedge angle ($\theta = 19°$), and $v_{\parallel}/v = \sin(\theta)$, it features an enhancement of the air-damping-limited Q_M^{air} by a factor of $\beta = \sin(\theta)^2 \approx 10$. The calculated Q_M^{air} for the 13th crown mode in figure 7.4 is around 50,000.

In summary, the measured mechanical Q-factors of the crown modes in microdisk resonators features a record high value (25,000–80,000) for optomechanical oscillators in the air. It is one order of magnitude higher than the mechanical Q of microtoroids in the air. Detailed analysis of the mechanical loss mechanisms indicates that air-damping loss is reduced in wedge-like microdisks due to the small projected vibration velocity along the surface area. The clamping loss for the crown modes are negligible due the confined vibration in the edge of the wedge region. The measured high mechanical Q factors in the disk resonators are around the material-loss-limited regime.

7.3.2 Low-phase-noise Optomechanical Oscillator

For any self-sustaining regenerative oscillator, the oscillation linewidth above threshold is directly related to the intrinsic resonator damping rate or Q factor [108, 109]. It has been shown that the fundamental Schawlow-Townes (ST) linewidth [103, 158] for an optomechanical oscillator is

$$\Delta\Omega_M = \frac{\Gamma_M n_T}{2\bar{n}_c}, \tag{7.9}$$

where n_T is the thermal occupation of the mechanical bath at temperature T and frequency Ω_m, and $n_T \approx \frac{k_B T}{\hbar\Omega_m}$. $\bar{n}_c$ is the phonon number of the coherent mechanical oscillation above threshold, and $\bar{n}_c = \frac{E}{\hbar\Omega_m}$, where E is the stored mechanical energy in the oscillator. Thus equation (7.9) can be rewritten as

$$\Delta\Omega_M = \frac{\Gamma_M k_B T}{2E}. \tag{7.10}$$

It can be seen that the ST linewidth of OMO is proportional to the intrinsic mechanical damping rate, and inverse proportional to the oscillation energy (power), which is the classical ST characteristics. Also, the ST linewidth of OMO is proportional to the temperature as well. That is because the phase of the optomechanical oscillator is perturbed by the noise processes coupling to the thermal bath at temperature T.

The measured SSB phase noise of the high-Q optomechanical oscillator at 16.4 MHz (D=300 μm) is given in figure 7.5a. The detected RF power (which is proportional to the oscillation power) from the photodetector is increasing from upper to lower curves: -18, -7, -2, and 2 dBm. We can see that in general, the measured phase noise decreases with the increase of the oscillation power. While equation (7.10) can be used to explain the drop of the $1/f^2$ phase noise component with power, the Leeson's equation for an oscillator's phase noise can be used to explain the drop of the white, 1/f, $1/f^2$, and $1/f^3$ phase noise components with the increase of oscillation power [108],

$$L(f) = 10\log\left[\frac{1}{2}\left(1+\left(\frac{f_m}{2Q_M f}\right)^2\right)\left(1+\frac{f_c}{f}\right)\frac{Fk_BT}{P}\right], \tag{7.11}$$

where $f_m = \Omega_m/2\pi$ is the OMO frequency, Q_M is the mechanical Q factor, f_c is the corner frequency for flicker noise, and F is the noise figure.

The RF spectrum for the OMO at 16.4 MHz is given in figure 7.5b, with span 5 kHz and RBW 10 Hz. The spectrum is resolution bandwidth limited. Due to the nonlinear transduction function of the cavity response from the Lorentzian lineshape, the RF spectrum of the OMO output shows many higher harmonics of the fundamental oscillation frequency, shown in figure 7.5c. It can be used as a RF harmonic comb generator.

Figure 7.6 summaries the SSB phase noise of the low-noise microdisk OMOs in this work, two MEMS oscillators made of CC beam and glass disk respectively [159], and also a temperature-controlled quartz crystal oscillator (TCXO). Two microdisk OMOs are plotted, with diameter 0.3 and 0.4 mm. Both of these two OMOs have similar level of white and $1/f^2$ phase noise, but the larger disk (0.4 mm) has a much lower flicker phase noise component. In fact, it is the record low phase noise of an OMO demonstrated, to the best of our knowledge. The two OMOs have a much lower phase noise than the the MEMS beam oscillator, and it comparable to the MEMS glass disk oscillator. Also plotted is the phase noise of a temperature-controlled quartz crystal oscillator (TCXO, Greenray Industries, Inc., model T75). We can see that the $1/f^2$ phase noise of the OMOs, without any active temperature control, is only about 20 dB higher than the TCXO.

7.3.3 Linewidth Narrowing below OMO Threshold

The mechanical mode of an optomechanical oscillator starts regenerative oscillation when the blue-detuned pump laser provides high enough gain to overcome the intrinsic damping loss. Thus if we monitor the mechanical mode spectrum as a function of the pump laser power below threshold, linewidth narrowing should occur on account of optomechanical amplification by radiation pressure. It can be shown that the effective mechanical damping rate in presence of optomechanical

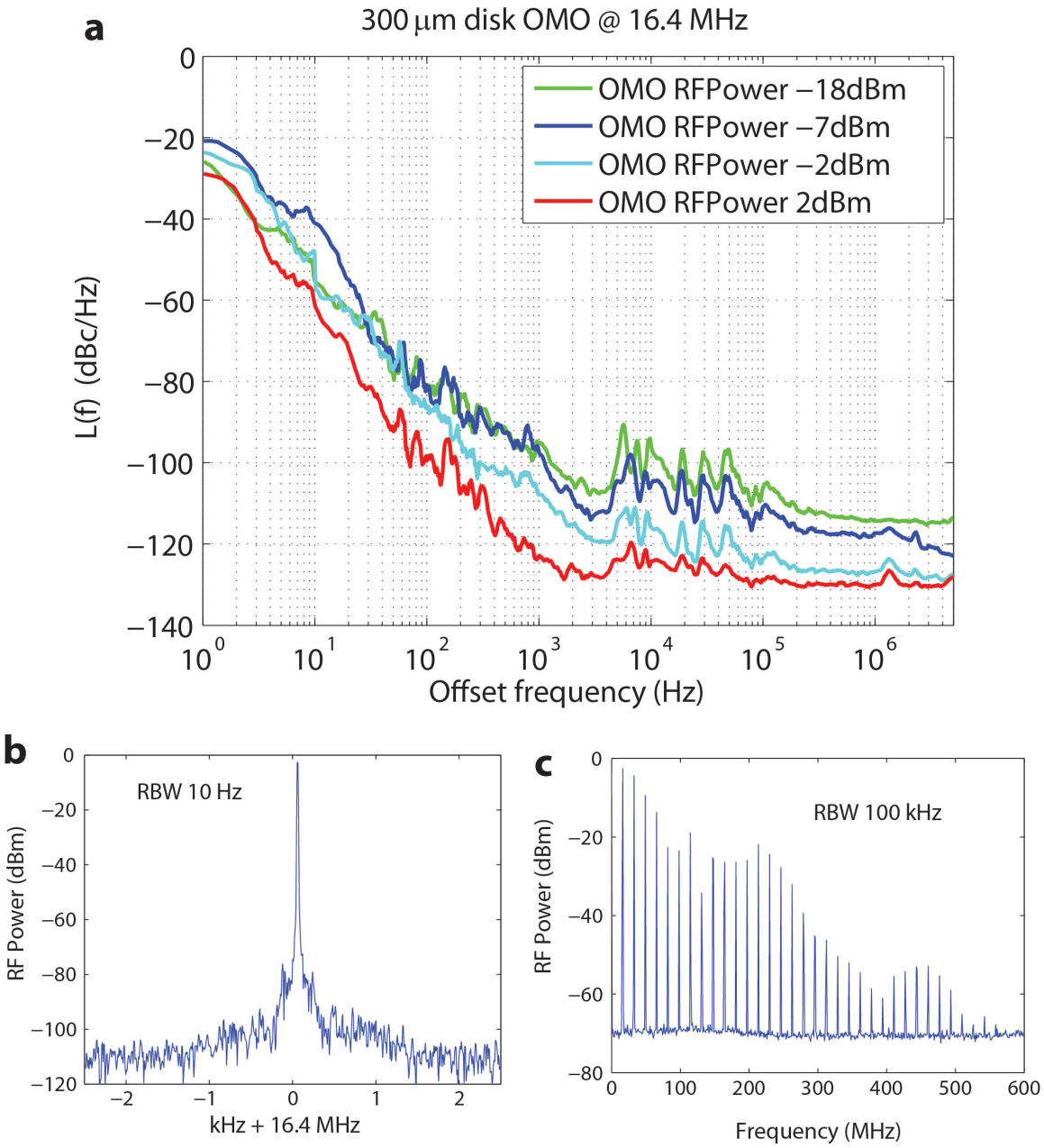

Figure 7.5: **Phase noise and RF spectrum of an optomechanical oscillator.** (a) SSB phase spectrum of an optomechanical oscillator (OMO) at 16.4 MHz from a 300 μm disk resonator with high mechancial Q in the air. The oscillator RF power detected from the same photodetector is increasing from upper to lower curves: -18, -7, -2, and 2 dBm. (b) RF spectrum of the low-phase-noise OMO at 16.4 MHz with span 5kHz and RBW 10 Hz. (c) Harmonic RF spectrum of the OMO detected from a PD with 125 MHz bandwidth. Due to the nonlinear transduction function of the cavity response from the Lorentzian lineshape, the RF spectrum of the OMO output shows many higher harmonics of the fundamental oscillation frequency. It can be used as a RF harmonic comb generator.

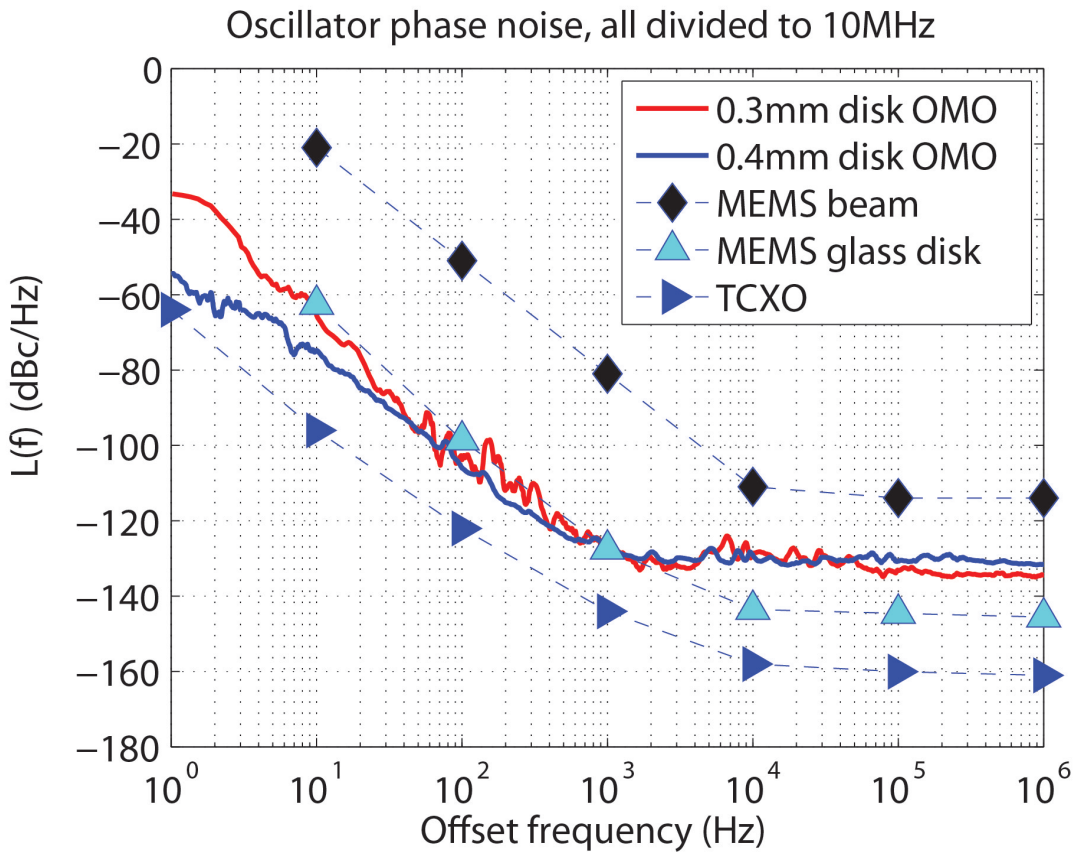

Figure 7.6: **Comparison of microdisk OMO with other low-noise oscillators.** The SSB phase noise of two microdisk OMOs, with diameter 0.3 and 0.4 mm are plotted. The larger (0.4 mm) OMO disk features the lowest phase noise for an OMO so far. And it has a relatively low flicker phase noise than the 0.3 mm disk. In comparison, the SSB phase noise spectra of two MEMS oscillators, made of CC beam and glass disk respectively [159], are shown. Also plotted is the phase noise of a temperature-controlled quartz crystal oscillator (TCXO). All the phase noise curves have been scaled to 10 MHz for fair comparison.

amplification can be rewritten as [146]

$$\Gamma_{eff} = \Gamma_M - \frac{4g^2 n_{cav}}{\kappa}\left[\frac{\kappa^2/4}{(\Delta-\Omega_m)^2+\kappa^2/4} - \frac{\kappa^2/4}{(\Delta+\Omega_m)^2+\kappa^2/4}\right], \tag{7.12}$$

where n_{cav} is the intracavity photon number, κ is the cavity photon damping rate, and Δ is the pump detuning. $g = g_{OM}\sqrt{\hbar/2m_{eff}\Omega_m}$ is the optomechanical coupling rate, denoting the cavity frequency shift by the zero-point motion of the mechanical oscillator. $g_{OM} \equiv \frac{\mathrm{d}\omega}{\mathrm{d}x} = -\omega/R$. From equation (7.12), it can be seen that a blue detuned laser provides amplification to mechanical motion, while a red detuned laser provides cooling of mechanical motion. Also, the optomechanical amplification rate is proportional to the intracavity photon number.

The linewidth narrowing effect of the mechanical motion due to optomechanical amplification in the high-mechanical-Q microdisk resonators below oscilation threshold is studied. An OMO disk resonator with dimensions: $D = 300$ μm, $\theta \approx 19°$, thickness T = 8 μm, undercut C = 127 μm was used. The optical resonance has a loaded linewidth of 32 MHz at critically coupling. The pump laser is kept at half detuning level, i.e., $\Delta = \frac{1}{2}\kappa$ with the increase of the pump power below threshold. The transmitted cavity signal is analyzed using a RF spectrum analyzer.

The measured mechanical mode spectra below threshold is given in figure 7.7. The OMO frequency is at 13.553 MHz. And the intracavity photon number is calculated as $n_{cav} = \frac{\kappa_{ex}P_{in}}{(\kappa^2/4+\Delta^2)\hbar\omega_l}$. Lorentzian fitting is used to extract the cavity linewidth at each pump power level, which is plotted versus the intracavity photon number in figure 7.8. Both these two figures show a clear trend of the linewidth narrowing of mechanical motion on account of optomechanical amplification. Also figure 7.8 shows a linear fit (dashed line) of the mechanical damping rate with the intracavity photon number, according to equation (7.12). The linear fit gives an instrinc of mechanical linewidth $\Gamma_M/2\pi =$ 618 Hz, or equivalently $Q_M =$ 25,200. It also gives the optomechancial coupling rate $g = 78$ rad/s. The relative small value of g is expected due to the large cavity size and thick oxide.

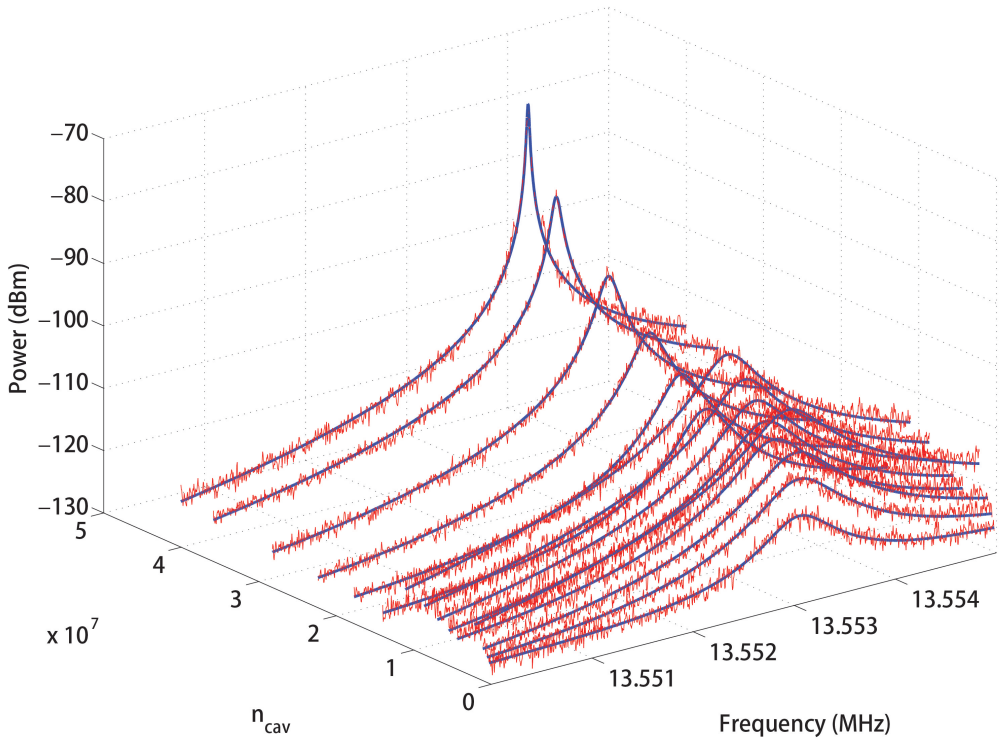

Figure 7.7: **Amplification of mechanical motion below threshold.** OMO disk dimensions: $D = 300$ μm, $\theta \approx 19°$, thickness T = 8 μm, undercut C = 127 μm. The cavity is kept at critical coupling and the pump laser is kept at half detuning level, i.e., $\Delta = \frac{1}{2}\kappa$ with the increase of the pump power. The loaded cavity linewidth $\kappa/2\pi = 32$ MHz. And the OMO frequency is at 13.553 MHz.

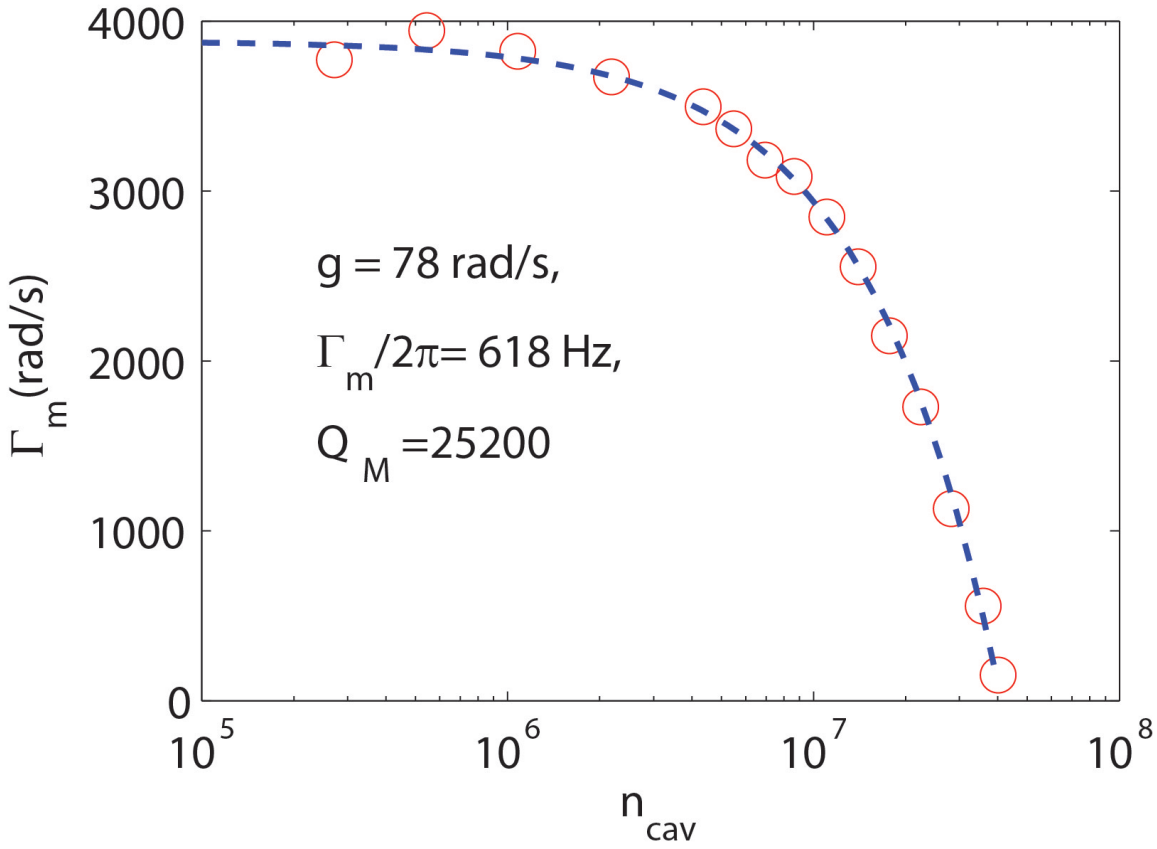

Figure 7.8: **Linewidth narrowing of mechanical mode below threshold.** The effective linewidth of the mechanical mode in presence of optomechancial amplification in figure 7.7 is plotted versus the intracavity photon number. An intrinsic mechanical linewidth of 618 Hz is measured at 13.553 MHz, giving a mechanical Q of 25,200.

Appendix A

Frequency Locking to Microcavities

For laser frequency stabilization to high-Finesse reference cavities, it is required to lock the external laser to the line center of the cavity resonance. Frequency locking can be implemented in a variety of ways, e.g., the Pound-Drever-Hall (PDH) locking [121], Hänsch-Couillaud (HC) locking [95], and optical feedback injection locking [160]. Here we show detailed information on applying the PDH and HC locking techniques to whispering-gallery-mode microresonators.

For the Hänsch-Couillaud technique [95, 154], the polarization state of the input laser is chosen such that it is composed of two orthogonal components, i.e., $\mathbf{E}_{cav}$ and $\mathbf{E}_{LO}$. $\mathbf{E}_{cav}$ is coupled to the interrogated cavity mode, while $\mathbf{E}_{LO}$ is served as the optical local oscillator (reference arm). The cavity transmitted field contains phase shift from the cavity. This phase shift can be transformed to a dispersive error signal by homodyne detection of the interference (superposition) of the LO and cavity transmission fields. Because $\mathbf{E}_{cav}$ and $\mathbf{E}_{LO}$ are orthogonal, a quarter wave plate and a polarization beam splitter (PBS) is used to rotate and decompose the LO and cavity transmission fields to the same x and y coordinates. The schematic for the HC locking technique is given in figure A.1a. An example of the HC dispersive error signal together with the cavity transmission is given in figure A.1c. A phase lock loop control (with servo and laser frequency control) is then applied for frequency locking.

For the Pound-Drever-Hall (PDH) locking to microresonators, two FM sidebands are created with the probe laser using an electro-optical modulator (EOM). These two sidebands will experience different phase shifts after the cavity. The detected beat signal from the cavity transmission is then downconverted to the baseband by mixing with the electrical local oscillator. The phase difference of the two sidebands is transformed to a dispersive error signal because the downcovertion can be simply viewed as the superposition of the upper and lower sidebands. The schematic for PDH locking to a WGM cavity is given in figure A.1b. Also figure A.1d shows the typical PDH error signal together with a cavity resonance.

Both of these two methods are classic ways for laser frequency locking. The HC method uses the same laser as the local oscillator and requires less instrumentation. But it is more sensitive

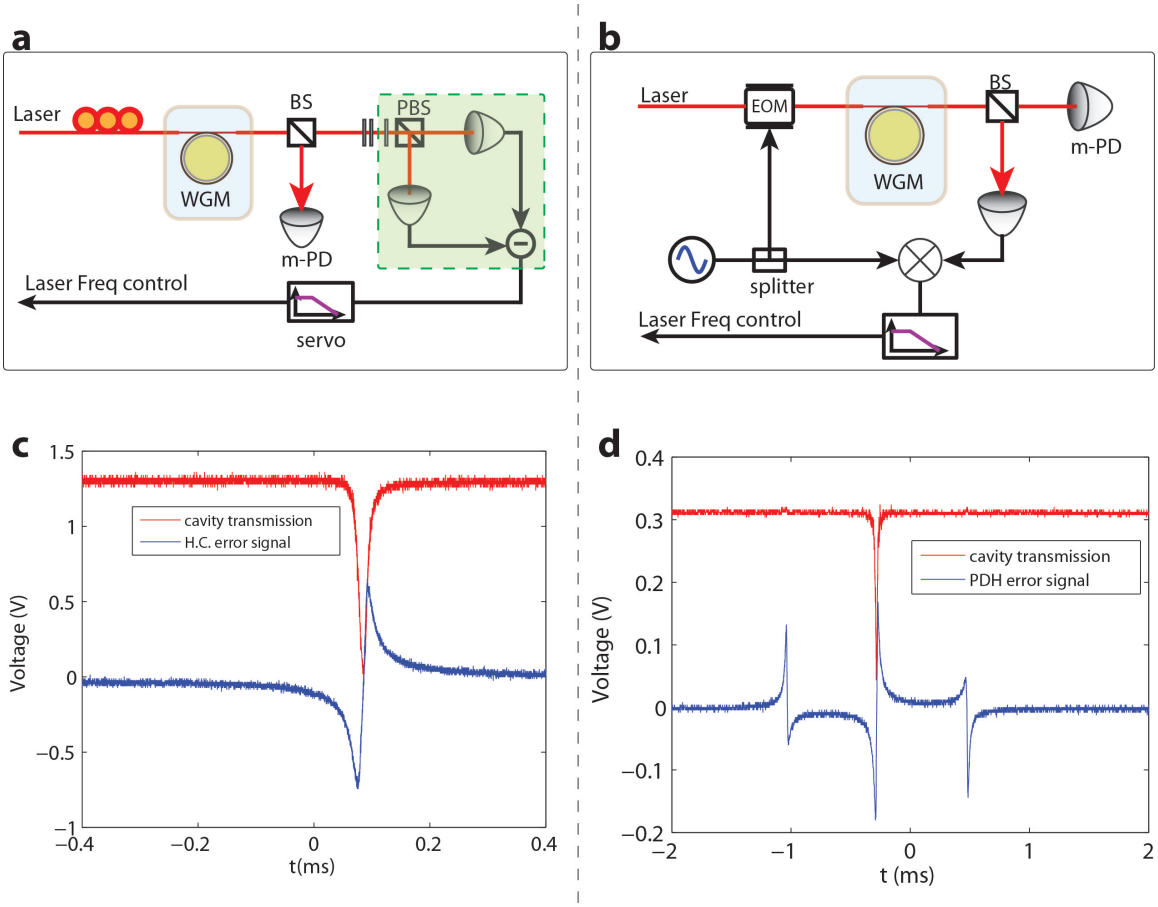

Figure A.1: **Laser frequency locking to microcavities.** (a) Schematic for Hänsch-Couillaud (HC) locking technique to frequency stabilization of the laser to a WGM resonator. BS: beam spiltter; PBS: polarization beam splitter; m-PD: monitor photodetector. The dashed box on the right is the balanced homodyne detection to create a dispersive error signal across cavity resonance. (b) Schematic for Pound-Drever-Hall (PHD) frequency stabilization. EOM: Electro-optic phase modulator. (c) Cavity Transmission signal (red) and the HC dispersive error signal (blue) when the laser is scanned across a resonance. (d) Cavity Transmission signal (red) and the PDH dispersive error signal (blue) when the laser is scanned across a resonance.

to polarization state drift in the fiber. The PDH method is insensitive to polarization drift, but it requires an EOM and a signal generator as the local oscillator. To examine the locking quality, the in-loop error signal can be analyzed using a RF spectrum analyzer. Figure A.2 gives the PSD of the in-loop error signal when a fiber laser is used to locked to a 15 mm disk resonator using PHD method. The blue curve is at the open-loop operation, while the probe laser is manually tune approximately to the cavity line center. The red curve is at closed-loop when PDH lock is on. The cyan curve is the noise background (photon shot noise and detector thermal noise) when the laser is off-resonance. The y-axis shows the raw data from the spectrum analyzer and is proportional to the frequency noise of the laser (wrt the disk resonator). It can seen that the laser frequency noise is reduced more than 40 dB at 100 Hz Fourier frequency.

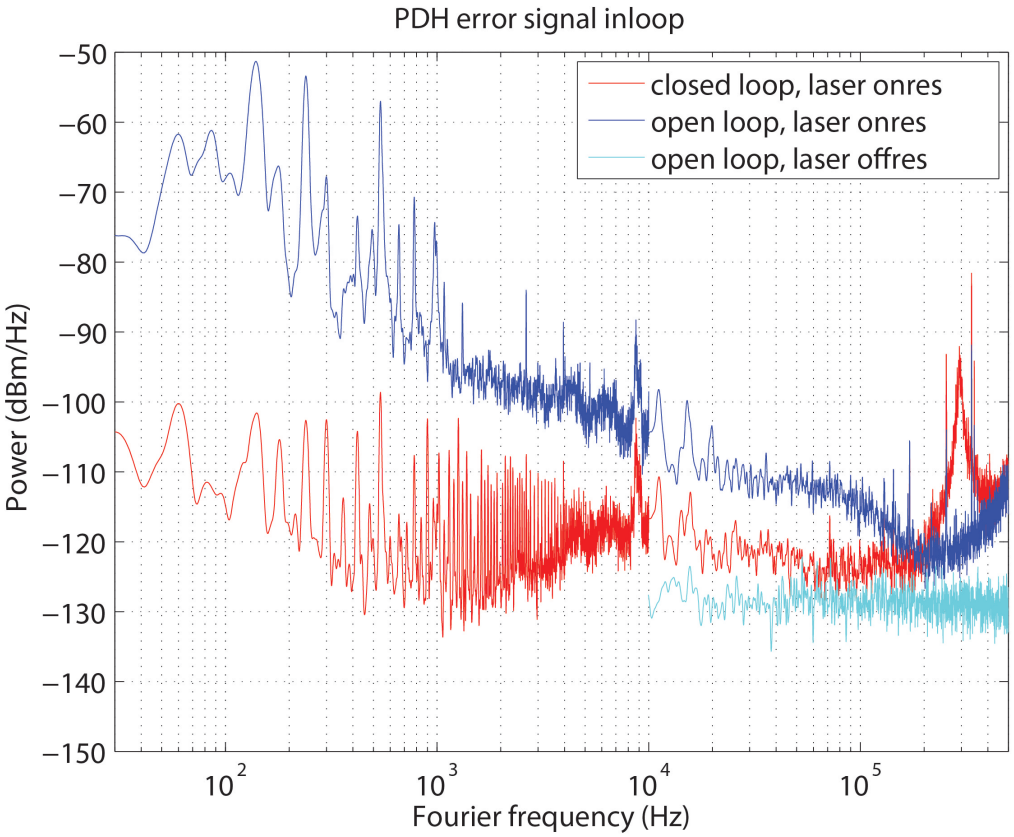

Figure A.2: **laser frequency noise reduction with frequency stabilization.** The power spectral density (PSD) of the in-loop PDH error signal when a probe laser in interrogating an ultra-high-Q planar disk reaontor. The probe laser is a CW narrow-linewidth fiber laser (Orbits lightwave, Inc.). Blue curve: open-loop operation, while the probe laser is manually tune approximately to the cavity line center. Red curve: closed-loop when PDH lock is on. Cyan curve: noise background (photon shot noise and detector thermal noise) when the laser is off-resonance. The PSD is proportional to the frequency noise of the laser (relative to the disk resonator). Laser frequency noise reduction up to 40 dB is obtained at 100 Hz Fourier frequency.

Appendix B

Measurement of Laser Frequency Noise Fluctuation Spectrum

Measurement of the laser frequency noise fluctuation spectrum requires a frequency discriminator to convert frequency fluctuations to intensity fluctuations. A frequency discrimator can be an interferometer, a cavity resonance or an atomic/molecular transition line. On the other hand, heterodyne of two independent but identical lasers is another convenient way to measure laser phase noise (frequency noise) because the beat signal can be analyzed by a RF spectrum analyzer or a phase noise analyzer directly. Both of these two methods (frequency discriminator and heterodyne) are applied here to characterize two kinds of laser in our laboratory.

For the frequency discriminator method, we use a fiber-based Mach-Zehnder interferometer (MZI). One arm is delayed by 100–200 ns with regard to the other arm in the MZI, resulting a FSR between 10 and 5 MHz. The two complementary outputs of the MZI are sent into a balanced photodetector. Thus at quadrature point of the MZI output, the intensity noise of the laser is suppressed, while the slope of the MZI fringes gives a conversion of the laser frequency noise to output intensity fluctuations and can be analyzed using a baseband FFT spectrum analyzer. The power spectrum density on the FFT analyzer can be written as [7]

$$W_{ESA}(f) = \frac{V_{pp}^2 \pi^2 \tau^2 sinc^2(\tau f) S_\nu(f)}{R_L}, \tag{B.1}$$

where V_{pp} is the peak-to-peak voltage of the MZI fringe, $\tau = 1/FSR$ is the delay of one arm, and R_L is the load impedance. $S_\nu(f)$ is the one-sided power spectral density of the laser frequency noise (and it is twice as large as the two-sided PSD). The measured laser FM noise spectra for an external-cavity diode laser (ECDL, New Focus 6700) and a narrow linewidth fiber laser (Orbits Lightwave) are given in figure B.1a. It can be seen that the ECDL laser reaches a white frequency noise (Schawlow-Townes noise) for offset frequencies greater than 80 kHz, while it has certain big amount of technical noise for low offset frequencies below 10 kHz. The technical noise is related to

current noise of the diode, and also thermal, acoustic and mechanical noises. For the fiber laser, it has both much lower technical noise and white frequency noise. The noise bump around 1 MHz for the fiber laser is attributed to relaxation oscillations.

The single-sideband phase noise can be converted from the frequency noise spectrum using $L(f) = 10\log\left(\frac{S_\nu(f)}{f^2}\right) - 3$, shown in figure B.1b. Also, two independent but identical Orbits fiber lasers were photomixed on a fast photodetector and the beat signal is analyzed by a phase noise analyzer (PNA). This is a very convenient way to measure laser phase noise spectrum, albeit with much higher requirements on test equipments (a second laser and a PNA). The measured SSB phase noise of fiber laser is plotted in figure B.1b. Here we subtract 3 dB from the original heterodyne phase noise to account for the phase noise of a single laser. It can be seen from figure B.1b that the measured SSB phase noise using two distinct methods are in excellent agreement with each other.

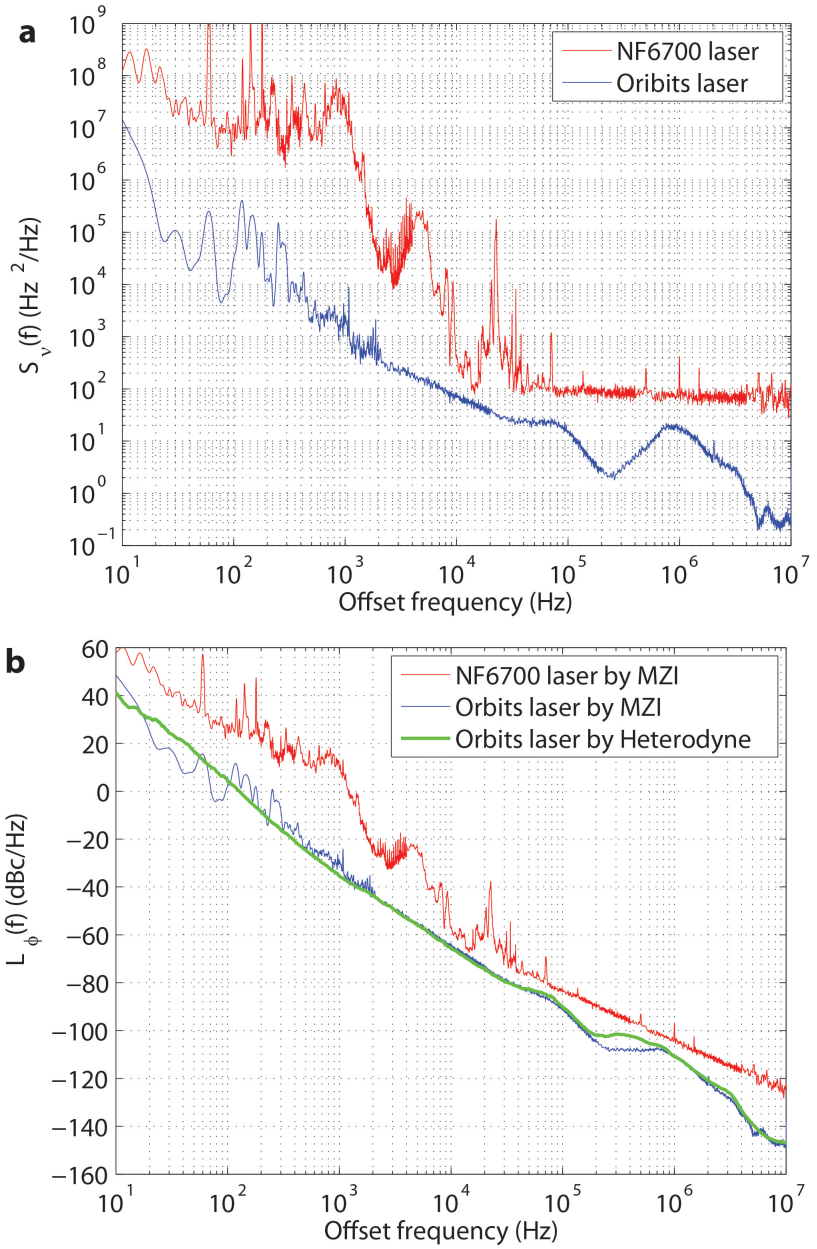

Figure B.1: **Measurement of laser frequency noise spectrum.** (a) Red curve: frequency noise spectrum of the New Focus 6700 laser; Blue cure: frequency noise spectrum of the Orbits fiber laser. These two FM noise spectra were measured by a Mach-Zehnder Interferometer (MZI) with balanced detector. (b) Single-sideband (SSB) phase noise the New Focus 6700 laser (red) and Orbits fiber laser (blue), measured by MZI. The SSB phase noise of the Orbits laser was also measured by analyzing the phase noise of the heterodyne beat signal of two independent Orbits fibers with identical specification. A factor of 3 dB has been subtracted from the measured SSB phase noise of the beat note to get the SSB phase noise of one fiber laser. Albeit two very different approaches were used (MZI FM discrimator and heterodyne beat), the measured laser FM noises are in excellent agreement with each other.

Appendix C

Publications

J. Li, H. Lee, and K. J. Vahala, "Microwave synthesizer using an on-chip Brillouin oscillator," *accepted by Nat. Commun.* (2013).

J. Li, H. Lee, T. Chen, and K. J. Vahala, "Low-Pump-Power, Low-Phase-noise, and Microwave to Millimeter-wave Repetition Rate Operation in Microcombs," *Phys. Rev. Lett.* **109**, 233901 (2012).

H. Lee*, T. Chen*, J. Li* (*Co-first-authors), K. Y. Yang, S. Jeon, O. Painter, K. J. Vahala, "Chemically etched ultrahigh-Q wedge-resonator on a silicon chip," *Nat. Photon.* **6**, 369–373 (2012).

J. Li, H. Lee, T. Chen, K. J. Vahala, "Characterization of a high coherence, Brillouin microcavity laser on silicon," *Opt. Exp.* **20**, 20170–20180 (2012).

J. Li, H. Lee, K. Y. Yang, and K. J. Vahala, "Sideband spectroscopy and dispersion measurement in microcavities," *Opt. Exp.* **20**, 26337–26344 (2012).

H. Lee, T. Chen, J. Li, O. Painter, K. J. Vahala, "Ultra-low-loss optical delay line on a silicon chip," *Nature Commun.* **3**, 867 (2012)

T. Chen, H. Lee, J. Li, and K. J. Vahala, "A general design algorithm for low optical loss adiabatic connections in waveguides," *Opt. Exp.* **20**, 22819–22829 (2012).

W. Schweinberger, A. Sommer, E. Bothschafter, J. Li, F. Krausz, R. Kienberger, and M. Schultze, "Waveform-controlled near-single-cycle milli-joule laser pulses generate sub-10 nm extreme ultraviolet continua," *Opt. Lett.* **37**, 3573–3575 (2012).

J. Li, H. Jiang, J. Xiao, and Q. Gong, "The mechanism of multi-focusing of lasers into uniaxial

crystals," *J. Opt. A: Pure Appl. Opt.* **9**, 664–672 (2007).

Bibliography

[1] K. J. Vahala, "Optical microcavities," *Nature* **424**, 839–846 (2003).

[2] T. Aoki, B. Dayan, E. Wilcut, W. P. Bowen, A. S. Parkins, T. Kippenberg, K. Vahala, and H. Kimble, "Observation of strong coupling between one atom and a monolithic microresonator," *Nature* **443**, 671–674 (2006).

[3] T. Kippenberg and K. Vahala, "Cavity optomechanics: back-action at the mesoscale," *Science* **321**, 1172–1176 (2008).

[4] F. Vollmer and S. Arnold, "Whispering-gallery-mode biosensing: Label-free detection down to single molecules," *Nature Methods* **5**, 591–596 (2008).

[5] T. Lu, H. Lee, T. Chen, S. Herchak, J.-H. Kim, S. E. Fraser, R. C. Flagan, and K. Vahala, "High sensitivity nanoparticle detection using optical microcavities," *Proceedings of the National Academy of Sciences* **108**, 5976–5979 (2011).

[6] T. Kippenberg, R. Holzwarth, and S. Diddams, "Microresonator-based optical frequency combs," *Science* **332**, 555–559 (2011).

[7] H. Lee, T. Chen, J. Li, K. Y. Yang, S. Jeon, O. Painter, and K. J. Vahala, "Chemically etched ultrahigh-Q wedge-resonator on a silicon chip," *Nature Photonics* **6**, 369–373 (2012).

[8] J. Li, H. Lee, T. Chen, and K. J. Vahala, "Characterization of a high coherence, Brillouin microcavity laser on silicon," *Optics Express* **20**, 20170–20180 (2012).

[9] I. S. Grudinin, A. B. Matsko, and L. Maleki, "On the fundamental limits of Q factor of crystalline dielectric resonators," *Optics Express* **15**, 3390–3395 (2007).

[10] I. S. Grudinin, V. S. Ilchenko, and L. Maleki, "Ultrahigh optical Q factors of crystalline resonators in the linear regime," *Physical Review A* **74**, 063806 (2006).

[11] A. A. Savchenkov, A. B. Matsko, V. S. Ilchenko, and L. Maleki, "Optical resonators with ten million finesse," *Optics Express* **15**, 6768–6773 (2007).

[12] D. Armani, T. Kippenberg, S. Spillane, and K. Vahala, "Ultra-high-Q toroid microcavity on a chip," *Nature* **421**, 925–928 (2003).

[13] M. Cai, O. Painter, and K. J. Vahala, "Observation of critical coupling in a fiber taper to a silica-microsphere whispering-gallery mode system," *Physical Review Letters* **85**, 74–77 (2000).

[14] S. Spillane, T. Kippenberg, O. Painter, and K. Vahala, "Ideality in a fiber-taper-coupled microresonator system for application to cavity quantum electrodynamics," *Physical Review Letters* **91**, 43902 (2003).

[15] I. S. Grudinin, A. B. Matsko, and L. Maleki, "Brillouin Lasing with a CaF_2 Whispering Gallery Mode Resonator," *Physical Review Letters* **102**, 043902 (2009).

[16] M. Tomes and T. Carmon, "Photonic micro-electromechanical systems vibrating at X-band (11-GHz) rates," *Physical Review Letters* **102**, 113601 (2009).

[17] M. J. Thorpe, R. J. Jones, K. Moll, J. Ye, and R. Lalezari, "Precise measurements of optical cavity dispersion and mirror coating properties via femtosecond combs," *Optics Express* **13**, 882–888 (2005).

[18] A. Schliesser, C. Gohle, T. Udem, T. W. Hänsch, et al., "Complete characterization of a broadband high-finesse cavity using an optical frequency comb," *Optics Express* **14**, 5975–5983 (2006).

[19] P. Del'Haye, O. Arcizet, M. Gorodetsky, R. Holzwarth, and T. Kippenberg, "Frequency comb assisted diode laser spectroscopy for measurement of microcavity dispersion," *Nature Photonics* **3**, 529–533 (2009).

[20] A. A. Savchenkov, E. Rubiola, A. B. Matsko, V. S. Ilchenko, L. Maleki, et al., "Phase noise of whispering gallery photonic hyper-parametric microwave oscillators," *Optics Express* **16**, 4130–4144 (2008).

[21] R. DeVoe, C. Fabre, K. Jungmann, J. Hoffnagle, and R. Brewer, "Precision optical-frequency-difference measurements," *Physical Review A* **37**, 1802 (1988).

[22] J. Li, H. Lee, T. Chen, O. Painter, and K. Vahala, "Chip-based Brillouin lasers as spectral purifiers for photonic systems," *arXiv preprint arXiv:1201.4212* (2012).

[23] M. Oxborrow, "Traceable 2-D finite-element simulation of the whispering-gallery modes of axisymmetric electromagnetic resonators," *Microwave Theory and Techniques, IEEE Transactions on* **55**, 1209–1218 (2007).

[24] O. Arcizet, A. Schliesser, P. DelHaye, R. Holzwarth, and T. J. Kippenberg, "Optical frequency comb generation in monolithic microresonators," *Practical Applications of Microresonators in Optics and Photonics, AB Matsko, ed.(CRC Press, 2009)* (2009).

[25] G. P. Agrawal, *Nonlinear Fiber Optics* (Springer, 2000).

[26] D. J. Jones, S. A. Diddams, J. K. Ranka, A. Stentz, R. S. Windeler, J. L. Hall, and S. T. Cundiff, "Carrier-envelope phase control of femtosecond mode-locked lasers and direct optical frequency synthesis," *Science* **288**, 635–639 (2000).

[27] S. A. Diddams, D. J. Jones, J. Ye, S. T. Cundiff, J. L. Hall, J. K. Ranka, R. S. Windeler, R. Holzwarth, T. Udem, and T. Hänsch, "Direct link between microwave and optical frequencies with a 300 THz femtosecond laser comb," *Physical Review Letters* **84**, 5102–5105 (2000).

[28] R. Holzwarth, T. Udem, T. W. Hänsch, J. Knight, W. Wadsworth, and P. S. J. Russell, "Optical frequency synthesizer for precision spectroscopy," *Physical Review Letters* **85**, 2264–2267 (2000).

[29] T. Udem, R. Holzwarth, T. W. Hänsch, et al., "Optical Frequency Metrology," *Nature* **416**, 233–237 (2002).

[30] S. Diddams, T. Udem, J. Bergquist, E. Curtis, R. Drullinger, L. Hollberg, W. Itano, W. Lee, C. Oates, K. Vogel, et al., "An optical clock based on a single trapped $^{199}Hg^{+}$ ion," *Science* **293**, 825–828 (2001).

[31] T. Rosenband, D. Hume, P. Schmidt, C. Chou, A. Brusch, L. Lorini, W. Oskay, R. Drullinger, T. Fortier, J. Stalnaker, et al., "Frequency ratio of Al^{+} and Hg^{+} single-ion optical clocks; metrology at the 17th decimal place," *Science* **319**, 1808–1812 (2008).

[32] M. Hentschel, R. Kienberger, C. Spielmann, G. Reider, N. Milosevic, T. Brabec, P. Corkum, U. Heinzmann, M. Drescher, F. Krausz, et al., "Attosecond metrology," *Nature* **414**, 509–513 (2001).

[33] T. Fortier, M. Kirchner, F. Quinlan, J. Taylor, J. Bergquist, T. Rosenband, N. Lemke, A. Ludlow, Y. Jiang, C. Oates, et al., "Generation of ultrastable microwaves via optical frequency division," *Nature Photonics* **5**, 425–429 (2011).

[34] T. Steinmetz, T. Wilken, C. Araujo-Hauck, R. Holzwarth, T. W. Hänsch, L. Pasquini, A. Manescau, S. D'Odorico, M. T. Murphy, T. Kentischer, et al., "Laser frequency combs for astronomical observations," *Science* **321**, 1335–1337 (2008).

[35] C.-H. Li, A. J. Benedick, P. Fendel, A. G. Glenday, F. X. Kärtner, D. F. Phillips, D. Sasselov, A. Szentgyorgyi, and R. L. Walsworth, "A laser frequency comb that enables radial velocity measurements with a precision of 1 cm s^{-1}," *Nature* **452**, 610–612 (2008).

[36] F. Quinlan, G. Ycas, S. Osterman, and S. Diddams, "A 12.5 GHz-spaced optical frequency comb spanning >400," *Review of Scientific Instruments* **81**, 063105–063105 (2010).

[37] A. Bartels, D. Heinecke, and S. A. Diddams, "10-GHz self-referenced optical frequency comb," *Science* **326**, 681–681 (2009).

[38] P. DelHaye, A. Schliesser, O. Arcizet, T. Wilken, R. Holzwarth, and T. Kippenberg, "Optical frequency comb generation from a monolithic microresonator," *Nature* **450**, 1214–1217 (2007).

[39] T. Kippenberg, S. Spillane, and K. Vahala, "Kerr-nonlinearity optical parametric oscillation in an ultrahigh-Q toroid microcavity," *Physical Review Letters* **93**, 83904 (2004).

[40] A. A. Savchenkov, A. B. Matsko, D. Strekalov, M. Mohageg, V. S. Ilchenko, and L. Maleki, "Low Threshold Optical Oscillations in a Whispering Gallery Mode CaF_2 Resonator," *Physical Review Letters* **93**, 243905 (2004).

[41] A. A. Savchenkov, A. B. Matsko, V. S. Ilchenko, I. Solomatine, D. Seidel, and L. Maleki, "Tunable optical frequency comb with a crystalline whispering gallery mode resonator," *Physical Review Letters* **101**, 93902 (2008).

[42] I. S. Grudinin, N. Yu, and L. Maleki, "Generation of optical frequency combs with a CaF_2 resonator," *Optics Letters* **34**, 878–880 (2009).

[43] D. Braje, L. Hollberg, and S. Diddams, "Brillouin-enhanced hyperparametric generation of an optical frequency comb in a monolithic highly nonlinear fiber cavity pumped by a CW laser," *Physical Review Letters* **102**, 193902 (2009).

[44] J. S. Levy, A. Gondarenko, M. A. Foster, A. C. Turner-Foster, A. L. Gaeta, and M. Lipson, "CMOS-compatible multiple-wavelength oscillator for on-chip optical interconnects," *Nature Photonics* **4**, 37–40 (2009).

[45] F. Ferdous, H. Miao, D. E. Leaird, K. Srinivasan, J. Wang, L. Chen, L. T. Varghese, and A. M. Weiner, "Spectral line-by-line pulse shaping of on-chip microresonator frequency combs," *Nature Photonics* **5**, 770–776 (2011).

[46] L. Razzari, D. Duchesne, M. Ferrera, R. Morandotti, S. Chu, B. Little, and D. Moss, "CMOS-compatible integrated optical hyper-parametric oscillator," *Nature Photonics* **4**, 41–45 (2009).

[47] S. B. Papp and S. A. Diddams, "Spectral and temporal characterization of a fused-quartz-microresonator optical frequency comb," *Physical Review A* **84**, 053833 (2011).

[48] P. DelHaye, T. Herr, E. Gavartin, M. Gorodetsky, R. Holzwarth, and T. Kippenberg, "Octave spanning tunable frequency comb from a microresonator," *Physical Review Letters* **107**, 63901 (2011).

[49] Y. Okawachi, K. Saha, J. S. Levy, Y. H. Wen, M. Lipson, and A. L. Gaeta, "Octave-spanning frequency comb generation in a silicon nitride chip," *Optics Letters* **36**, 3398–3400 (2011).

[50] P. DelHaye, O. Arcizet, A. Schliesser, R. Holzwarth, and T. J. Kippenberg, "Full stabilization of a microresonator-based optical frequency comb," *Physical Review Letters* **101**, 53903 (2008).

[51] J. Li, H. Lee, T. Chen, and K. J. Vahala, "Chip-based Frequency Comb with Microwave Repetition Rate," in *Frontiers in Optics* (2011).

[52] J. Li, H. Lee, T. Chen, and K. J. Vahala, "Low-Pump-Power, Low-Phase-Noise, and Microwave to Millimeter-Wave Repetition Rate Operation in Microcombs," *Physical Review Letters* **109**, 233901 (2012).

[53] A. B. Matsko, A. A. Savchenkov, D. Strekalov, V. S. Ilchenko, and L. Maleki, "Optical hyperparametric oscillations in a whispering-gallery-mode resonator: Threshold and phase diffusion," *Physical Review A* **71**, 033804 (2005).

[54] T. Herr, K. Hartinger, J. Riemensberger, C. Wang, E. Gavartin, R. Holzwarth, M. Gorodetsky, and T. Kippenberg, "Universal formation dynamics and noise of Kerr-frequency combs in microresonators," *Nature Photonics* **6**, 480–487 (2012).

[55] M. A. Foster, J. S. Levy, O. Kuzucu, K. Saha, M. Lipson, and A. L. Gaeta, "Silicon-based monolithic optical frequency comb source," *Optics Express* **19**, 14233–14239 (2011).

[56] L. Maleki, V. Ilchenko, A. Savchenkov, W. Liang, D. Seidel, and A. Matsko, "High performance, miniature hyper-parametric microwave photonic oscillator," in *Frequency Control Symposium (FCS), 2010 IEEE International* pp. 558–563 (2010).

[57] T. Carmon, L. Yang, and K. J. Vahala, "Dynamical thermal behavior and thermal self-stability of microcavities," *Optics Express* **12**, 4742–4750 (2004).

[58] A. Savchenkov, A. Matsko, W. Liang, V. Ilchenko, D. Seidel, and L. Maleki, "Kerr combs with selectable central frequency," *Nature Photonics* **5**, 293–296 (2011).

[59] A. H. Zewail, "Femtochemistry: Atomic-scale dynamics of the chemical bond," *The Journal of Physical Chemistry A* **104**, 5660–5694 (2000).

[60] A. Baltuska, T. Udem, M. Uiberacker, M. Hentschel, E. Goulielmakis, C. Gohle, R. Holzwarth, V. Yakovlev, A. Scrinzi, T. W. Hänsch, et al., "Attosecond control of electronic processes by intense light fields," *Nature* **421**, 611–615 (2003).

[61] W. R. Zipfel, R. M. Williams, W. W. Webb, et al., "Nonlinear magic: multiphoton microscopy in the biosciences," *Nature Biotechnology* **21**, 1369–1377 (2003).

[62] A. Weiner, *Ultrafast Optics* (Wiley, 2011).

[63] M. T. Asaki, C.-P. Huang, D. Garvey, J. Zhou, H. C. Kapteyn, and M. M. Murnane, "Generation of 11-fs pulses from a self-mode-locked Ti: Sapphire laser," *Optics Letters* **18**, 977–979 (1993).

[64] U. Morgner, F. Kärtner, S. Cho, Y. Chen, H. Haus, J. Fujimoto, E. Ippen, V. Scheuer, G. Angelow, and T. Tschudi, "Sub-two-cycle pulses from a Kerr-lens mode-locked Ti: Sapphire laser," *Optics Letters* **24**, 411–413 (1999).

[65] H. A. Haus, "Mode-locking of lasers," *Selected Topics in Quantum Electronics, IEEE Journal of* **6**, 1173–1185 (2000).

[66] A. Matsko, A. Savchenkov, W. Liang, V. Ilchenko, D. Seidel, and L. Maleki, "Mode-locked Kerr frequency combs," *Optics Letters* **36**, 2845–2847 (2011).

[67] A. B. Matsko, W. Liang, A. A. Savchenkov, and L. Maleki, "Chaotic dynamics of frequency combs generated with continuously pumped nonlinear microresonators," *Optics Letters* **38**, 525–527 (2013).

[68] T. Herr, V. Brasch, M. Gorodetsky, and T. Kippenberg, "Soliton mode-locking in optical microresonators," *arXiv preprint arXiv:1211.0733* (2012).

[69] K. Saha, Y. Okawachi, B. Shim, J. S. Levy, M. A. Foster, R. Salem, A. R. Johnson, M. R. Lamont, M. Lipson, and A. L. Gaeta, "Modelocking and femtosecond pulse generation in chip-based frequency combs," *Optics Express* **21**, 1335–1343 (2013).

[70] R. Trebino, *Frequency-Resolved Optical Gating: The Measurement of Ultrashort Laser Pulses* (Springer, 2000).

[71] V. Ilchenko and M. Gorodetskii, "Thermal nonlinear effects in optical whispering gallery microresonators," *Laser Phys* **2**, 1004–1009 (1992).

[72] A. E. Fomin, M. L. Gorodetsky, I. S. Grudinin, and V. S. Ilchenko, "Nonstationary nonlinear effects in optical microspheres," *Journal of Optical Society of America B* **22**, 459–465 (2005).

[73] M. Eichenfield, R. Camacho, J. Chan, K. J. Vahala, and O. Painter, "A picogram-and nanometre-scale photonic-crystal optomechanical cavity," *Nature* **459**, 550–555 (2009).

[74] Q. Lin, J. Rosenberg, X. Jiang, K. J. Vahala, and O. Painter, "Mechanical oscillation and cooling actuated by the optical gradient force," *Physical Review Letters* **103**, 103601 (2009).

[75] A. Savchenkov, D. Eliyahu, W. Liang, V. Ilchenko, J. Byrd, A. Matsko, D. Seidel, and L. Maleki, "Miniature Optical Atomic Clock: Stabilization of a Kerr Comb Oscillator," *arXiv preprint arXiv:1301.3198* (2013).

[76] F. Quinlan, T. Fortier, H. Jiang, A. Hati, C. Nelson, Y. Fu, J. Campbell, and S. Diddams, "Exploiting shot noise correlations in the photodetection of ultrashort optical pulse trains," *Nature Photonics* **7**, 290–293 (2013).

[77] S. B. Papp, P. Del'Haye, and S. A. Diddams, "Mechanical control of a microrod-resonator optical frequency comb," *arXiv preprint arXiv:1205.4272* (2012).

[78] E. Ip, A. P. T. Lau, D. J. Barros, and J. M. Kahn, "Coherent detection in optical fiber systems," *Optics Express* **16**, 753–791 (2008).

[79] M. Nakazawa, S. Okamoto, T. Omiya, K. Kasai, and M. Yoshida, "256 QAM (64 Gbit/s) coherent optical transmission over 160 km with an optical bandwidth of 5.4 GHz," in *Optical Fiber Communication (OFC), collocated National Fiber Optic Engineers Conference, 2010 Conference on (OFC/NFOEC)* pp. 1–3 (2010).

[80] C. J. Karlsson, F. Å. Olsson, D. Letalick, and M. Harris, "All-Fiber Multifunction Continuous-Wave Coherent Laser Radar at 1.55 μm for Range, Speed, Vibration, and Wind Measurements," *Applied Optics* **39**, 3716–3726 (2000).

[81] R. Rafac, B. Young, J. Beall, W. Itano, D. Wineland, and J. Bergquist, "Sub-dekahertz Ultraviolet Spectroscopy of $^{199}Hg^{+}$," *Physical Review Letters* **85**, 2462–2465 (2000).

[82] B. Young, F. Cruz, W. M. Itano, and J. Bergquist, "Visible lasers with subhertz linewidths," *Physical Review Letters* **82**, 3799–3802 (1999).

[83] L. Yang, T. Lu, T. Carmon, B. Min, and K. J. Vahala, "A 4-Hz fundamental linewidth on-chip microlaser," in *Conference on Lasers and Electro-Optics* (2007).

[84] T. Lu, K. Vahala, T. Carmon, L. Yang, and B. Min, "Frequency noise of a microchip raman laser," in *Lasers and Electro-Optics, 2009 and 2009 Conference on Quantum electronics and Laser Science Conference. CLEO/QELS 2009. Conference on* pp. 1–2 (2009).

[85] W. Liang, V. Ilchenko, A. Savchenkov, A. Matsko, D. Seidel, and L. Maleki, "Whispering-gallery-mode-resonator-based ultranarrow linewidth external-cavity semiconductor laser," *Optics Letters* **35**, 2822–2824 (2010).

[86] R. Chiao, C. Townes, and B. Stoicheff, "Stimulated Brillouin scattering and coherent generation of intense hypersonic waves," *Physical Review Letters* **12**, 592–595 (1964).

[87] E. Ippen and R. Stolen, "Stimulated Brillouin scattering in optical fibers," *Applied Physics Letters* **21**, 539–541 (1972).

[88] S. Smith, F. Zarinetchi, and S. Ezekiel, "Narrow-linewidth stimulated Brillouin fiber laser and applications," *Optics Letters* **16**, 393–395 (1991).

[89] J. Geng, S. Staines, Z. Wang, J. Zong, M. Blake, and S. Jiang, "Highly stable low-noise Brillouin fiber laser with ultranarrow spectral linewidth," *Photonics Technology Letters, IEEE* **18**, 1813–1815 (2006).

[90] Y. Okawachi, M. S. Bigelow, J. E. Sharping, Z. Zhu, A. Schweinsberg, D. J. Gauthier, R. W. Boyd, and A. L. Gaeta, "Tunable all-optical delays via Brillouin slow light in an optical fiber," *Physical Review Letters* **94**, 153902 (2005).

[91] M. C. Gross, P. T. Callahan, T. R. Clark, D. Novak, R. B. Waterhouse, and M. L. Dennis, "Tunable millimeter-wave frequency synthesis up to 100 GHz by dual-wavelength Brillouin fiber laser," *Optics Express* **18**, 13321–13330 (2010).

[92] T. Schneider, M. Junker, and K.-U. Lauterbach, "Theoretical and experimental investigation of Brillouin scattering for the generation of millimeter waves," *Journal of Optical Society of America B* **23**, 1012–1019 (2006).

[93] R. W. Boyd, *Nonlinear Optics* (San Diego, CA (United States); Academic Press Inc., 1992).

[94] B. Min, T. J. Kippenberg, and K. J. Vahala, "Compact, fiber-compatible, cascaded Raman laser," *Optics Letters* **28**, 1507–1509 (2003).

[95] T. Hansch and B. Couillaud, "Laser frequency stabilization by polarization spectroscopy of a reflecting reference cavity," *Optics Communications* **35**, 441–444 (1980).

[96] A. Schliesser, R. Rivière, G. Anetsberger, O. Arcizet, and T. J. Kippenberg, "Resolved-sideband cooling of a micromechanical oscillator," *Nature Physics* **4**, 415–419 (2008).

[97] A. Yariv, *Quantum Electronics* (Wiley and Sons, New York, 1989).

[98] Z. Wu, L. Zhan, Q. Shen, J. Liu, X. Hu, and P. Xiao, "Ultrafine optical-frequency tunable Brillouin fiber laser based on fiber strain," *Optics Letters* **36**, 3837–3839 (2011).

[99] R. W. Tkach, A. R. Chraplyvy, and R. Derosier, "Spontaneous Brillouin scattering for single-mode optical-fibre characterisation," *Electronics Letters* **22**, 1011–1013 (1986).

[100] Y. Shen and N. Bloembergen, "Theory of stimulated Brillouin and Raman scattering," *Physical Review* **137**, A1787 (1965).

[101] A. Matsko, V. Ilchenko, A. Savchenkov, and L. Maleki, "Highly nondegenerate all-resonant optical parametric oscillator," *Physical Review A* **66**, 043814 (2002).

[102] I. S. Grudinin, H. Lee, O. Painter, and K. J. Vahala, "Phonon laser action in a tunable two-level system," *Physical Review Letters* **104**, 083901 (2010).

[103] K. J. Vahala, "Back-action limit of linewidth in an optomechanical oscillator," *Physical Review A* **78**, 023832 (2008).

[104] R. W. Boyd, K. Rzaewski, and P. Narum, "Noise initiation of stimulated Brillouin scattering," *Physical Review A* **42**, 5514 (1990).

[105] A. Debut, S. Randoux, and J. Zemmouri, "Linewidth narrowing in Brillouin lasers: Theoretical analysis," *Physical Review A* **62**, 023803 (2000).

[106] A. Debut, S. Randoux, and J. Zemmouri, "Experimental and theoretical study of linewidth narrowing in Brillouin fiber ring lasers," *Journal of Optical Society of America B* **18**, 556–567 (2001).

[107] M. Okai, M. Suzuki, and T. Taniwatari, "Strained multiquantum-well corrugation-pitch-modulated distributed feedback laser with ultranarrow (3.6 kHz) spectral linewidth," *Electronics Letters* **29**, 1696–1697 (1993).

[108] D. B. Leeson, "A simple model of feedback oscillator noise spectrum," *Proceedings of the IEEE* **54**, 329–330 (1966).

[109] A. Yariv, *Quantum Electronics, 3rd Edition* (John Wiley & Sons, New York, 1989).

[110] A. J. Seeds and K. J. Williams, "Microwave photonics," *Lightwave Technology, Journal of* **24**, 4628–4641 (2006).

[111] A. Khanna, "Microwave oscillators: the state of the technology," *Microwave Journal* **49**, 22 (2006).

[112] D. Howe and A. Hati, "Low-noise X-band oscillator and amplifier technologies: Comparison and status," in *Frequency Control Symposium and Exposition, 2005. Proceedings of the 2005 IEEE International* pp. 481–487 (2005).

[113] J. Capmany and D. Novak, "Microwave photonics combines two worlds," *Nature Photonics* **1**, 319–330 (2007).

[114] X. S. Yao and L. Maleki, "Optoelectronic microwave oscillator," *Journal of Optical Society of America B* **13**, 1725–1735 (1996).

[115] L. Maleki, "Sources: the optoelectronic oscillator," *Nature Photonics* **5**, 728–730 (2011).

[116] A. Savchenkov, V. Ilchenko, W. Liang, D. Eliyahu, A. Matsko, D. Seidel, and L. Maleki, "Voltage-controlled photonic oscillator," *Optics Letters* **35**, 1572–1574 (2010).

[117] M. L. Gorodetsky, A. A. Savchenkov, and V. S. Ilchenko, "Ultimate Q of optical microsphere resonators," *Optics Letters* **21**, 453–455 (1996).

[118] D. Vernooy, V. S. Ilchenko, H. Mabuchi, E. Streed, and H. Kimble, "High Q measurements of fused-silica microspheres in the near infrared," *Optics Letters* **23**, 247–249 (1998).

[119] G. Pillet, L. Morvan, M. Brunel, F. Bretenaker, D. Dolfi, M. Vallet, J.-P. Huignard, and A. Le Floch, "Dual-Frequency Laser at 1.5 μm for Optical Distribution and Generation of High-Purity Microwave Signals," *Journal of Lightwave Technology* **26**, 2764–2773 (2008).

[120] J. Maxin, S. Molin, G. Pillet, L. Morvan, A. Mugnier, D. Pureur, and D. Dolfi, "Dual-frequency distributed feedback fibre laser for microwave signals generation," *Electronics Letters* **47**, 816–818 (2011).

[121] R. Drever, J. L. Hall, F. Kowalski, J. Hough, G. Ford, A. Munley, and H. Ward, "Laser phase and frequency stabilization using an optical resonator," *Applied Physics B* **31**, 97–105 (1983).

[122] G. J. Schneider, J. A. Murakowski, C. A. Schuetz, S. Shi, and D. W. Prather, "Radiofrequency signal-generation system with over seven octaves of continuous tuning," *Nature Photonics* **7**, 118–122 (2013).

[123] S. Fukushima, C. Silva, Y. Muramoto, and A. Seeds, "10 to 110 GHz tunable opto-electronic frequency synthesis using optical frequency comb generator and uni-travelling-carrier photodiode," *Electronics Letters* **37**, 780–781 (2001).

[124] J. J. McFerran, E. Ivanov, A. Bartels, G. Wilpers, C. Oates, S. A. Diddams, and L. Hollberg, "Low-noise synthesis of microwave signals from an optical source," *Electronics Letters* **41**, 650–651 (2005).

[125] W. C. Swann, E. Baumann, F. R. Giorgetta, and N. R. Newbury, "Microwave generation with low residual phase noise from a femtosecond fiber laser with an intracavity electro-optic modulator," *Optics Express* **19**, 24387–24395 (2011).

[126] J. Alnis, A. Schliesser, C. Wang, J. Hofer, T. Kippenberg, and T. Hänsch, "Thermal-noise-limited crystalline whispering-gallery-mode resonator for laser stabilization," *Physical Review A* **84**, 011804 (2011).

[127] A. A. Savchenkov, A. B. Matsko, V. S. Ilchenko, N. Yu, and L. Maleki, "Whispering-gallery-mode resonators as frequency references. II. Stabilization," *Journal of Optical Society of America B* **24**, 2988–2997 (2007).

[128] N. Yu, L. M. Baumgartel, Y. Chembo, I. S. Grudinin, D. V. Strekalov, and R. J. Thompson, "Whispering-gallery-mode resonators for miniature optical clocks," in *SPIE LASE* pp. 82360P–82360P (2012).

[129] P. DelHaye, S. B. Papp, and S. A. Diddams, "Hybrid Electro-Optically Modulated Microcombs," *Physical Review Letters* **109**, 263901 (2012).

[130] X. S. Yao, "High-quality microwave signal generation by use of Brillouin scattering in optical fibers," *Optics Letters* **22**, 1329–1331 (1997).

[131] J. Geng, S. Staines, and S. Jiang, "Dual-frequency Brillouin fiber laser for optical generation of tunable low-noise radio frequency/microwave frequency," *Optics Letters* **33**, 16–18 (2008).

[132] P. T. Callahan, M. C. Gross, and M. L. Dennis, "Frequency-independent phase noise in a dual-wavelength Brillouin fiber laser," *Quantum Electronics, IEEE Journal of* **47**, 1142–1150 (2011).

[133] R. Pant, C. G. Poulton, D.-Y. Choi, H. Mcfarlane, S. Hile, E. Li, L. Thevenaz, B. Luther-Davies, S. J. Madden, and B. J. Eggleton, "On-chip stimulated Brillouin scattering," *Optics Express* **19**, 8285–8290 (2011).

[134] L. Langley, M. Elkin, C. Edge, M. Wale, U. Gliese, X. Huang, and A. Seeds, "Packaged semiconductor laser optical phase-locked loop (OPLL) for photonic generation, processing and transmission of microwave signals," *Microwave Theory and Techniques, IEEE Transactions on* **47**, 1257–1264 (1999).

[135] A. Bordonalli, C. Walton, and A. J. Seeds, "High-performance phase locking of wide linewidth semiconductor lasers by combined use of optical injection locking and optical phase-lock loop," *Journal of Lightwave Technology* **17**, 328 (1999).

[136] M. Alouini, B. Benazet, M. Vallet, M. Brunel, P. Di Bin, F. Bretenaker, A. Le Floch, and P. Thony, "Offset phase locking of Er, Yb: glass laser eigenstates for RF photonics applications," *Photonics Technology Letters, IEEE* **13**, 367–369 (2001).

[137] A. Rylyakov and T. Zwick, "96-GHz static frequency divider in SiGe bipolar technology," *Solid-State Circuits, IEEE Journal of* **39**, 1712–1715 (2004).

[138] T. Kessler, C. Hagemann, C. Grebing, T. Legero, U. Sterr, F. Riehle, M. Martin, L. Chen, and J. Ye, "A sub-40-mHz-linewidth laser based on a silicon single-crystal optical cavity," *Nature Photonics* **6**, 687–692 (2012).

[139] M. L. Gorodetsky and I. S. Grudinin, "Fundamental thermal fluctuations in microspheres," *Journal of Optical Society of America B* **21**, 697–705 (2004).

[140] A. B. Matsko, A. A. Savchenkov, N. Yu, and L. Maleki, "Whispering-gallery-mode resonators as frequency references. I. Fundamental limitations," *Journal of Optical Society of America B* **24**, 1324–1335 (2007).

[141] J. Alnis, A. Schliesser, C. Wang, J. Hofer, T. Kippenberg, and T. Hänsch, "Thermal-noise-limited crystalline whispering-gallery-mode resonator for laser stabilization," *Physical Review A* **84**, 011804 (2011).

[142] D. Strekalov, R. Thompson, L. Baumgartel, I. Grudinin, and N. Yu, "Temperature measurement and stabilization in a birefringent whispering gallery resonator," *arXiv preprint arXiv:1105.6350* (2011).

[143] K. Numata, A. Kemery, and J. Camp, "Thermal-noise limit in the frequency stabilization of lasers with rigid cavities," *Physical Review Letters* **93**, 250602 (2004).

[144] L. Landau and E. Lifshitz, "Statistical Physics, Vol. 1," *Oxford: Pergamon* **24**, 31–57 (1980).

[145] A. Schliesser, G. Anetsberger, R. Rivière, O. Arcizet, and T. Kippenberg, "High-sensitivity monitoring of micromechanical vibration using optical whispering gallery mode resonators," *New Journal of Physics* **10**, 095015 (2008).

[146] T. J. Kippenberg and K. J. Vahala, "Cavity opto-mechanics," *Optics Express* **15**, 17172–17205 (2007).

[147] T. Kippenberg, H. Rokhsari, T. Carmon, A. Scherer, and K. Vahala, "Analysis of radiation-pressure induced mechanical oscillation of an optical microcavity," *Physical Review Letters* **95**, 033901 (2005).

[148] H. Rokhsari, T. Kippenberg, T. Carmon, and K. Vahala, "Radiation-pressure-driven micromechanical oscillator," *Optics Express* **13**, 5293–5301 (2005).

[149] A. Schliesser, P. DelHaye, N. Nooshi, K. Vahala, and T. Kippenberg, "Radiation pressure cooling of a micromechanical oscillator using dynamical backaction," *Physical Review Letters* **97**, 243905 (2006).

[150] J. Chan, T. M. Alegre, A. H. Safavi-Naeini, J. T. Hill, A. Krause, S. Gröblacher, M. Aspelmeyer, and O. Painter, "Laser cooling of a nanomechanical oscillator into its quantum ground state," *Nature* **478**, 89–92 (2011).

[151] J. Teufel, T. Donner, D. Li, J. Harlow, M. Allman, K. Cicak, A. Sirois, J. Whittaker, K. Lehnert, and R. Simmonds, "Sideband cooling of micromechanical motion to the quantum ground state," *Nature* **475**, 359–363 (2011).

[152] A. H. Safavi-Naeini, J. Chan, J. T. Hill, T. P. M. Alegre, A. Krause, and O. Painter, "Observation of quantum motion of a nanomechanical resonator," *Physical Review Letters* **108**, 033602 (2012).

[153] G. Anetsberger, R. Rivière, A. Schliesser, O. Arcizet, and T. J. Kippenberg, "Ultralow-dissipation optomechanical resonators on a chip," *Nature Photonics* **2**, 627–633 (2008).

[154] A. Schliesser, G. Anetsberger, R. Rivière, O. Arcizet, and T. Kippenberg, "High-sensitivity monitoring of micromechanical vibration using optical whispering gallery mode resonators," *New Journal of Physics* **10**, 095015 (2008).

[155] R. O. Pohl, X. Liu, and E. Thompson, "Low-temperature thermal conductivity and acoustic attenuation in amorphous solids," *Reviews of Modern Physics* **74**, 991 (2002).

[156] R. Vacher, E. Courtens, and M. Foret, "Anharmonic versus relaxational sound damping in glasses. II. Vitreous silica," *Physical Review B* **72**, 214205 (2005).

[157] L. Landau and L. EM, *Fluid Mechanics: Volume 6 (Course Of Theoretical Physics)* (Butterworth-Heinemann, 1987).

[158] H. Rokhsari, M. Hossein-Zadeh, A. Hajimiri, and K. Vahala, "Brownian noise in radiation-pressure-driven micromechanical oscillators," *Applied physics Letters* **89**, 261109–261109 (2006).

[159] Y.-W. Lin, S. Lee, S.-S. Li, Y. Xie, Z. Ren, and C.-C. Nguyen, "Series-resonant VHF micromechanical resonator reference oscillators," *Solid-State Circuits, IEEE Journal of* **39**, 2477–2491 (2004).

[160] B. Dahmani, L. Hollberg, and R. Drullinger, "Frequency stabilization of semiconductor lasers by resonant optical feedback," *Optics Letters* **12**, 876–878 (1987).